SUB-BARRIER PHOTOFISSION MEASUREMENTS IN ^{238}U AND ^{232}Th

Jack Andrew Silano

A dissertation submitted to the faculty of the University of North Carolina at Chapel Hill in partial fulfillment of the requirements for the degree of Doctor of Philosophy in the Department of Physics and Astronomy.

Chapel Hill
2016

Approved by:

Hugon J. Karwowski

Nalin R. Parikh

Joaquin E. Drut

Reyco Henning

Mohammad W. Ahmed

Thomas B. Clegg

ABSTRACT

JACK ANDREW SILANO: SUB-BARRIER PHOTOFISSION MEASUREMENTS IN ^{238}U AND ^{232}Th.
(Under the direction of Hugon J. Karwowski.)

A study of photofission of ^{232}Th and ^{238}U was performed using quasi-monoenergetic, linearly-polarized γ-ray beams from the High Intensity γ-ray source at TUNL. The prompt photofission neutron polarization asymmetries, neutron multiplicities and the photofission cross sections were measured in the sub-barrier energy range of 4.3-6.3 MeV. This data set constitutes the lowest energy measurements of those observables to date. Large polarization asymmetries are observed in both nuclei, consistent with the only other measurement of this kind made at a higher energy range. Over the newly probed energy range the asymmetries, multiplicities and cross sections all vary smoothly, revealing no new resonant fission processes. The present cross sections are consistent with a triple-humped ^{232}Th fission barrier and a double-humped ^{238}U fission barrier. Previous experimental evidence of a third minimum in the ^{238}U fission barrier has been identified as an accelerator-induced background. Applications of the present data will also be discussed.

ACKNOWLEDGMENTS

Though this thesis is my own work, I could not have completed it without the help and support of my friends, family and colleagues. My experiences with them have shaped every part of my dissertation, and it wouldn't have been the same without them. First and foremost, I would like to thank Hugon Karwowski for his guidance and support throughout my graduate career. I owe nearly everything I have learned through my research experience to his mentorship, and for that I will always be grateful.

In my time at the University of North Carolina at Chapel Hill, I have had the opportunity to take classes and engage with many faculty members of the Physics & Astronomy Department. I would especially like to thank Tom Clegg and Reyco Henning for their thoughtful and thorough comments on my dissertation.

A special thanks to Nalin Parikh and Adriana Banu for assisting during the experiment. This work would not have been possible without their help. Thank you to Jonathan Mueller, Kevin Wierman, Mohammad Ahmed, Brent Fallin, Krishichayan, and Erin Hansen for their helpful discussions. Thanks to Grayson Rich for laying the groundwork for this project and getting the HIγS beam time approval.

I would like to thank Stepan Mikhailov and the HIγS staff for providing the γ-ray beams that made this work possible, and for their willingness to put up with my endless questions about the facility. Thank you to Bret Carlin and the TUNL staff for sharing their expertise, and for their patience with my many questions and requests over the years. Finally I would like to thank my family and friends for all of the love and friendship they have shown me throughout my life.

This work was supported in part by the United States Department of Energy (DOE) under Grant DE-FG02-03ER41-041.

TABLE OF CONTENTS

LIST OF FIGURES

LIST OF TABLES

LIST OF ABBREVIATIONS

CEBAF	Continuous Electron Beam Accelerator Facility
CFD	Constant fraction discriminator
CODA	CEBAF Online Data Acquisition system
DAQ	Data acquisition system
FEL	Free electron laser
FREYA	Fission Reaction Event Yield Algorithm
GDR	Giant dipole resonance
HIγS	High Intensity γ-ray Source
HPGe	High Purity Germanium
MCA	Multichannel analyzer
MS	Megasamples
PC	Proportional counter
PMT	Photomultiplier tube
PSD	Pulse shape discrimination
SNM	Special nuclear material
TFA	Timing filter amplifier
TKE	Total kinetic energy
TXE	Total excitation energy
TUNL	Triangle Universities Nuclear Laboratory
UTR	Upstream target room

CHAPTER 1: INTRODUCTION

1.1 Nuclear Fission

Since its discovery in 1939[1][2] nuclear fission has been a profoundly consequential reaction. The first application of fission was to create a devastating weapon which ended one war, nearly began others, and permanently changed the ramifications of warfare. Fission was next harnessed with powerful reactors to generate electricity which now provide 11% of the world's electricity[3]. Given the importance of fission it is reasonable to assume that the process is well understood.

While there has certainly been much progress in understanding the fission process over the past 77 years, a complete model of the fission mechanism has yet to be established. Fission is a "cataclysmic rearrangement of a single nucleus into two nuclei"[4]; a process which is affected by collective and single particle degrees of freedom. Currently there is no model which can quantitatively predict all observable features of the fission process. The lifetimes with respect to spontaneous fission are not well predicted by any theory[5][6].

Recent increases in computing power have facilitated the possibility of a comprehensive microscopic description of the fission process[7]. A complete and quantitively accurate microscopic fission model would significantly impact a number of fission applications which are currently in progress or being actively researched. A better understanding of fission would improve the design of the next generation of thorium-based reactors which are still in the prototype and design stages of development[8]. Additionally, since the current fission models are limited the safety margins for operating existing nuclear reactors are not precisely known, so the reactors are operated at a lower power output[9]. Improving the modeling of existing reactors would then allow for an increase of their power output.

Calculations of r-process nucleosynthesis would also benefit from improved nuclear modeling, particularly because calculations of the lifetimes of neutron-rich nuclei far from β-stability are similar to the calculations of the lifetimes of spontaneously fissioning nuclei[10]. An improved understanding of fission would also impact the detection and identification of special nuclear materials (SNM) through active and passive interrogation techniques[11], as these methods rely on detecting γ-rays and neutrons emitted by fissioning nuclei. This application is further motivated by the recent demonstration of a novel laser-wakefield accelerator-based γ-ray source[12], which raises the prospect of a portable, linearly-polarized γ-ray source for active interrogation.

The physical observables of fission such as the fission cross section, prompt neutron multiplicity and fragment angular distribution are determined by the structure of the fission barrier, the potential energy surface that an excited nucleus must overcome to split apart. In order for any calculation to be able to predict the fission observables accurately, it must be able to reproduce the fission barrier. Since the barrier can not be directly measured it must instead be inferred through measurements of fission observables.

A vast majority of the existing fission data come from neutron-induced fission. Depending on the interaction with the fissioning nucleus a neutron can bring different amounts of angular momentum into the system, changing how the nucleus travels through the fission barrier and the resulting observables. This means that neutron-induced fission data are a combination of multiple modes of the already complex fission reaction, making a precise determination of the fission barrier difficult. Photofission (fission induced by the absorption of a γ-ray) has proven to be a valuable probe of the fission barrier structure since a γ-ray brings a single unit of angular momentum into the fissioning system. Additionally, at energies below the fission barrier, the γ-ray interacts with the nucleus in a limited number of ways, greatly reducing the number of fission modes that contribute to the measured data. However, there are very few photofission data at low γ-ray energies where the effects of the fission barrier are most apparent, and there are significant discrepancies in some of the existing data sets.

It is the aim of the present work to provide data which may help to better constrain the shape of the fission barrier through measurements of the photofission process with ^{232}Th and ^{238}U targets. Photofission was investigated with linearly polarized γ-ray beams with energies between 4.3 and 6.3 MeV, and prompt fission neutrons were detected to measure the photofission cross sections, photofission neutron polarization asymmetries and prompt fission neutron multiplicities. The fission barriers of ^{232}Th and ^{238}U are inferred from the results of the photofission measurements, with the present work consistent with a triple-humped fission barrier for ^{232}Th and a double-humped fission barrier for ^{238}U. The results suggest that previous experimental evidence[13] of a third minimum in the ^{238}U fission barrier is an unaccounted-for accelerator-induced background, which is measured for the first time in the present work.

In the course of this work novel techniques for data acquisition and fission process simulations have been established and tested. The experiments described in this work are part of the photofission program at HIγS. Other work in this program includes measurements of photofission neutron polarization asymmetries[14], polarized photofission fragment angular distributions[15] and photofission fragment yields[16].

1.2 Overview of Contents

Chapter 2 will give an overview of the general characteristics of fission and the macroscopic-microscopic models which are used to describe the process. The specific case of photofission will be covered in Chapter 3 with a focus on the polarization asymmetry in the angular distributions of the fission fragments and the photofission cross section. A review of the existing measurements of the photofission cross sections, polarization asymmetries and prompt neutron multiplicities for ^{232}Th and ^{238}U will be given in Chapter 4. The experiment which comprises this work will be described in detail in Chapter 5. Detector calibrations, signal processing analysis and the validation of Monte Carlo simulations of the detectors used in this work will be covered in Chapter 6. A recently developed Monte Carlo fission modeling

code which was modified to simulate neutrons produced by photofission will be described in Chapter 7. Chapter 8 will describe the data reduction and analysis used to extract polarization asymmetries, multiplicities and cross sections. The results of this work will be given in Chapter 9 and will be discussed and compared to the existing measurements. Finally concluding remarks from this work and its impact on future work will be given in section 9.5.

CHAPTER 2: FISSION THEORY

2.1 General Aspects of Fission

Fission is a process in which the nucleus of an atom splits into two smaller nuclei, or fission fragments. The reaction can occur spontaneously in some heavier nuclei like ^{252}Cf, or can occur as the result of a nuclear excitation such as capture of a neutron forming an excited state. For the purposes of this work only fission induced by photoabsorption will be considered. During fission the excited nucleus becomes deformed to the point that it ultimately splits into two fragments in an event known as scission[17]. It is also possible for the nucleus to split into three or more fragments but those reactions are rare compared to binary fission, typically constituting less than 0.2% of all fission events[18], and will be neglected for the rest of this work. At low excitation energy the mass of the parent nucleus is typically divided between two fission fragments in a highly asymmetric manner, with one light fragment and one heavy fragment as shown in Fig. 2.1.

The scission of the nucleus is accompanied by the release of a large amount of energy, typically $\sim$ 200 MeV, primarily due to the release of the Coulomb energy of the positively charged nuclear fragments. For binary fission with no pre-scission neutrons emitted, the released energy is split between the kinetic energy of the fragments and their excitation energies, resulting in highly excited fragments traveling in opposite directions from one another. Because the ratio of neutrons to protons in a nucleus which is stable decreases with decreasing nuclear mass, the fragments will be relatively neutron rich. Consequently the most favorable method of fragment de-excitation is the emission of neutrons, followed by the emission of γ-rays and then β-decay.

Since its discovery a number of models have been used to describe fission, with varying

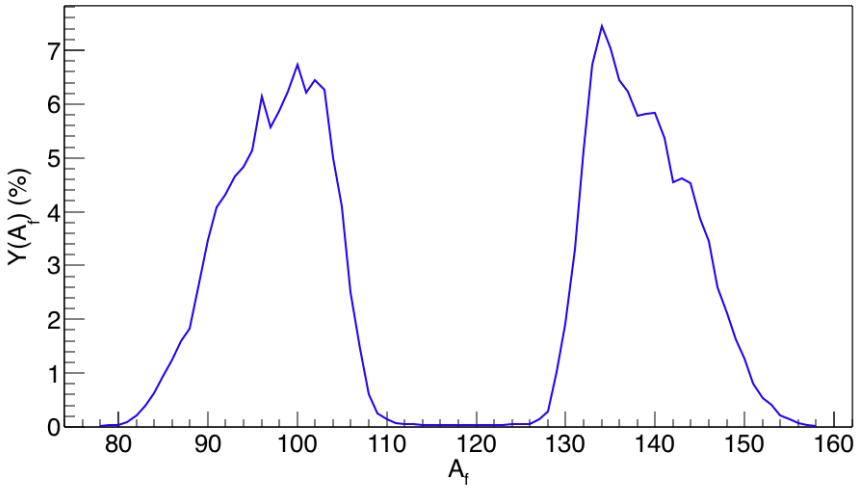

Figure 2.1: Fission fragment mass distribution for the ^{238}U(n,f) reaction[19].

degrees of success. This chapter will describe several historical models of fission which are useful for conceptually understanding the process, followed by a discussion of the more complex, modern macroscopic-microscopic approaches.

2.2 Liquid Drop Model

The liquid drop model developed by Bohr and Wheeler[20] represents the most fundamental explanation of the fission process, providing a useful qualitative understanding of the relevant nuclear forces. The nucleus is treated as a uniformly charged liquid drop with a total energy E of

$$E = E_v + E_s + E_C + E_{sy} + E_p, \tag{2.2.1}$$

where E_v is the volume energy, E_s is the surface energy, E_C is the Coulomb energy, E_{sy} is the symmetry energy and E_p is the pairing energy. E_v, E_{sy} and E_p remain constant during deformation and are thus not important to the fission process. The energy of the liquid drop is then given purely by a repulsive E_C and a restoring E_s, both of which depend on the

deformation of the drop. The deformation can be given by the multipole expansion

$$R(\theta) = \frac{R_o}{\lambda}\left[1 + \sum_{n=1} \alpha_n P_n(\cos\theta)\right], \tag{2.2.2}$$

where R_o is the radius of the undeformed drop, α_n is a coefficient which gives the contribution caused by deformation of order n, P_n is a Legendre polynomial, and λ is a scaling factor necessary to keep the volume of the drop constant with deformation. A nuclear deformation energy may then be defined as

$$E_{def} = E(R) - E(R_o), \tag{2.2.3}$$

where $E(R)$ is the energy of the deformed nucleus and $E(R_o)$ is the energy of the ground state undeformed nucleus. From calculations[21] of E_{def} there is no stable configuration of the ground state nucleus with contributions from terms of odd n, which correspond to asymmetric distributions[4]. The liquid drop model then cannot explain the observed asymmetric mass distribution.

Despite its shortcomings the liquid drop model still may provide insight into the origin of the fission barrier. By plotting E_{def} as a function of quadrupole deformation β as in Fig. 2.2, one can create a potential energy surface which qualitatively captures some of the aspects of fission. In this simple model the ground state minimum occurs at no deformation, another limitation of the model since ground state of many fissionable nuclei are known to have significant quadrupole deformation. As the nuclear deformation increases the deformation energy reaches a maximum, beyond which there is scission.

A nucleus can undergo fission by either being raised to an excitation energy above the barrier, or by tunneling through it at lower energies. Using the WKB approximation the probability of tunneling through the fission barrier can be calculated. For a parabolic fission barrier with height V_o and width $\hbar\omega$, the Hill-Wheeler transmission coefficient, T_{HW}, is given

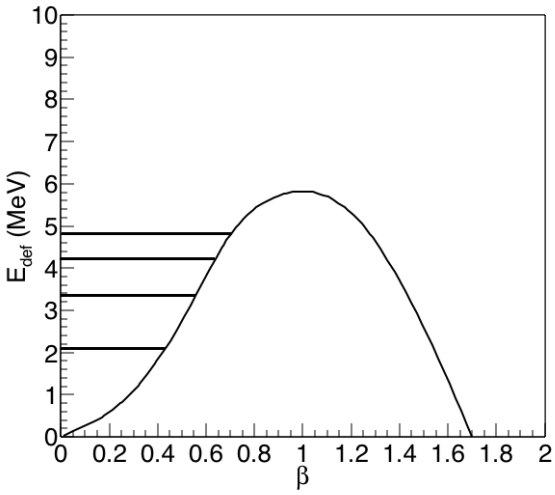

Figure 2.2: Generalized fission barrier from the liquid drop model. The ground state nucleus has no deformation, and several excited states with no deformation are shown.

by[22]

$$T_{HW} = \left[1 + \exp\left(2\pi \frac{V_o - E}{\hbar\omega}\right)\right]^{-1}. \tag{2.2.4}$$

Because of the unrealistic spherical ground state, the shape of the fission barrier obtained with the liquid drop model is likely too broad at the base, so the calculated barrier penetrabilities do a poor job of reproducing experimental measurements. The calculated fission barrier shape may then be improved upon by considering the role of shell effects.

2.3 Strutinsky Hybrid Model

The nuclear shell model treats nucleons as moving independently in an averaged potential produced by the mutual interaction of all the nucleons, consisting of a spherical central potential and a spin-orbit interaction. The nucleons are then characterized by wavefunctions which occupy individual energy levels. By calculating single particle states for deformed nuclear potentials, the total nuclear energy for an even-even nucleus can be written as[23]

$$E = \sum_{\mu} 2n_{\mu}\varepsilon_{\mu}, \tag{2.3.1}$$

where n_μ are the occupation numbers and ε_μ are the energy levels of the single particle states described by the Nilsson Hamiltonian[24]. Since the shell model potential is only an approximation and residual particle interactions are neglected, errors will accumulate and the resulting energy E will be less accurate than the liquid drop model energy.

The Strutinsky hybrid model attempts to reconcile this issue by taking the liquid drop model as a starting point and adding in the deviations due to the shell effects[25]. The total energy of the nucleus is expressed as[4]

$$E = E_{LDM} + \sum_{p,n}(\delta U + \delta P), \tag{2.3.2}$$

where E_{LDM} is the liquid drop model energy, δU is the shell correction energy and δP is the pairing correction energy; with both corrections dependent on the proton number, neutron number and nuclear deformation. The pairing correction arrises from the tendency of two nucleons of the same type to form a spin-0 pair which lowers the energy of the system. The shell correction is defined as the difference between the nuclear energy calculated for a realistic shell model potential, U, and an unrealistic uniform distribution which washes out the shell effects, $\tilde{U}$.

$$\delta U = U - \tilde{U}. \tag{2.3.3}$$

U is the sum of the single particle state energies as in

$$U = \sum_{\mu} 2 n_\mu \varepsilon_\mu. \tag{2.3.4}$$

$\tilde{U}$ results from an integration over a uniform distribution of states, $\tilde{g}(\varepsilon)$, as in

$$\tilde{U} = 2\int_{-\infty}^{\lambda} \varepsilon \tilde{g}(\varepsilon) d\varepsilon, \tag{2.3.5}$$

where λ is the chemical potential of the nucleus defined by the total number of nucleons, N,

$$N = 2\int_{-\infty}^{\lambda} \tilde{g}(\varepsilon)d\varepsilon. \tag{2.3.6}$$

The uniform distribution of states is achieved by taking the shell distribution from the Nilsson model[24] and averaging it over a large enough energy range to smooth out the finer shell effects. The distribution in this "Strutinsky smoothing method" is defined as

$$\tilde{g}(\varepsilon) = \frac{1}{\sqrt{\pi\gamma}} \sum_{\nu} exp\left[\left(\frac{\varepsilon - \varepsilon_{\nu}}{\gamma}\right)^2\right], \tag{2.3.7}$$

where ν is summed over the number of energy levels in the energy interval $\sqrt{\pi\gamma}$, which is centered at ε. The range of the spreading function γ is of the order of the shell spacing in order to sufficiently smooth out the effects of single particle excitations. The resulting distribution suffers from the same build-up of error due to lack of residual particle interactions and has the same, incorrect magnitude as the initial shell model calculations. However, because the calculations were performed over a spread of states the fine structure due to single particle excitations is not present, and the difference between the two calculations is purely due to shell effects.

The application of the Strutinsky model is shown in Fig. 2.3. The δU deviations between the shell model and smoothed shell model energies are added to the liquid drop model energy to incorporate shell effects into the fission barrier, significantly changing the barrier structure. The ground state of the nucleus now has nonzero deformation in agreement with the experimentally measured quadrupole ground state deformation. The fission barrier is no longer represented by a single "hump" but is instead double humped, with a second local minima within the barrier as single particle excitations allow for additional equilibrium configurations of deformed nuclei. The number of minima in the fission barrier is not limited to two, in fact as will be discussed in section 4.2 a third minima may be present for some nuclei.

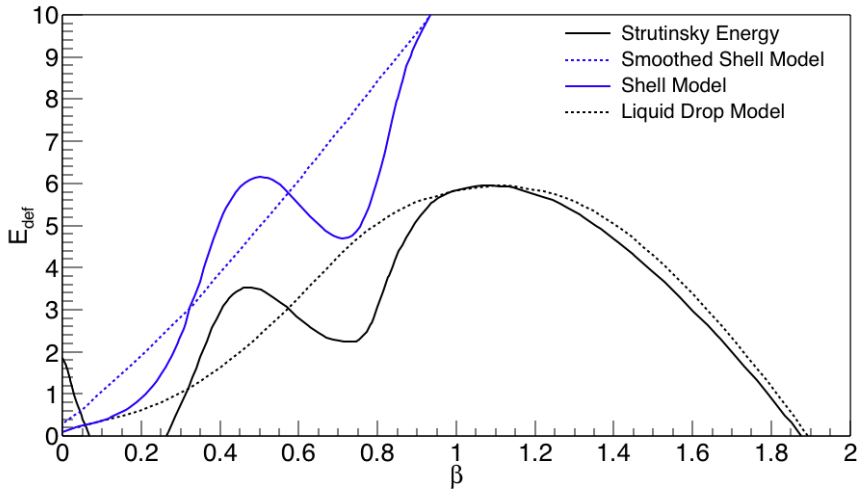

Figure 2.3: Illustration of Strutinsky method with generalized fission barrier structure, derived from Ref. [22].

2.4 Modern Fission Models

Advances in computing power have allowed for macroscopic-microscopic calculations to be performed with an increasing number of degrees of freedom in the deformation of the nucleus with more sophisticated and more realistic nuclear potentials. A recently developed macroscopic-microscopic model[26] calculated the fission barrier for ^{232}Th in 8-dimensional deformation parameter space. The microscopic energy was calculated with a deformed Woods-Saxon potential while the macroscopic energy was calculated using the Yukawa plus exponential model[27]. The potential energy surface as a function of quadrupole and hexadecapole deformations is shown in Fig. 2.4. The 8-dimensional surface is projected into two dimensions by minimizing the energy of the other 6 deformation parameters.

Improvements in computing have also created an avenue for entirely microscopic models of the fission barrier which do not need to be based around a macroscopic deformation energy. A self consistent model of the fission barrier was developed using finite-temperature superfluid nuclear density functional theory[28]. Nucleons are treated as harmonic oscillators in a Skyrme mean field. The calculated fission barrier for ^{232}Th is shown in Fig. 2.5 along with experimentally measured barrier heights, all in good general agreement. Overall there

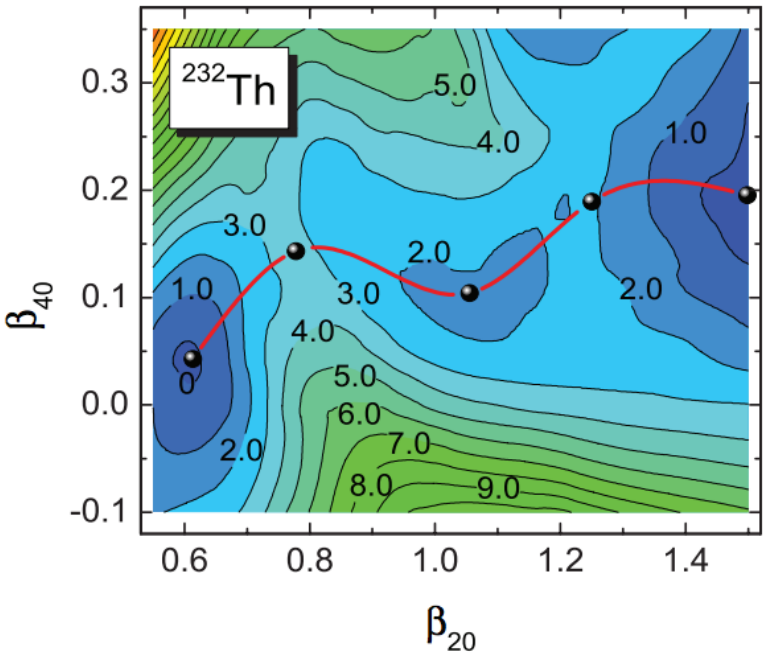

Figure 2.4: ^{232}Th fission barrier calculated with 8-dimensional macroscopic-microscopic model[26]. The axis labels β_{20} and β_{40} are the quadrupole and hexadecupole deformations, respectively.

is good agreement between modern macroscopic-microscopic and self-consistent models and inferred barrier structure from measurements. However, there is one aspect of the fission barrier for which there still considerable debate, both amongst theory and experimental data: the existence of a third minimum in the fission barrier.

For most nuclei theoretical calculations generally predict a double-humped fission barrier or at most a shallow third minimum, with a depth of less than 500 keV. Deep third minima arise only in calculations of some lighter mass isotopes of actinides with low neutron numbers. The depth of the third minimum has been associated with the neutron shell correction energy[28]. The influence of neutron number on the depth of the third minima is highlighted in Fig. 2.6, where the shallow third minimum vanishes with increasing isotopic mass. It is then expected that more neutron rich isotopes of an element like ^{232}Th and ^{238}U should not have deep third minima in their fission barriers.

Recent theoretical calculations of the ^{232}Th fission barrier predict a shallow third well with a depth of 0.5 MeV[29], 0.36 MeV[26] and < 0.1 MeV[28]. Due to the decreasing third

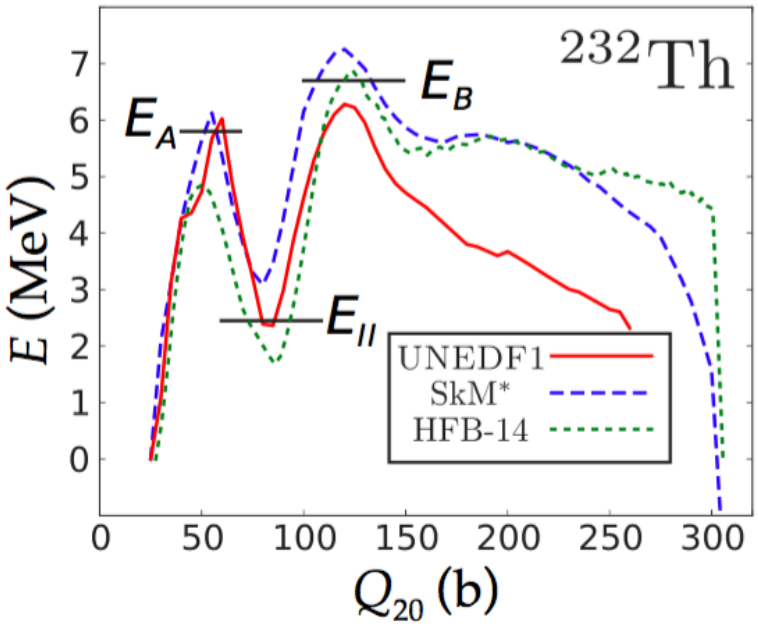

Figure 2.5: ^{232}Th fission barrier calculated with a self-consistent model, as a function of the quadrupole moment Q_{20}. Results with three different Skyrme energy density functionals are compared with experimentally measured barrier heights[28].

minimum depth with increasing neutron number, most barrier calculations of uranium isotopes are not extended to ^{238}U. It was only very recently that the ^{238}U barrier was calculated, using a multidimensionally constrained relativistic mean field model[29]. Two different interaction functionals were explored: the nonlinear point-coupling functional PC-PK1[30] and the density-dependent meson exchange functional DD-ME2[31] in the particle-hole channel. A 1.11 MeV deep third minimum was present in the ^{238}U fission barrier for the DD-ME2 calculation, while the PC-PK1 functional produced a double-humped fission barrier. As will be discussed in section 4.2 fission barrier structures inferred from experimental data are conflicting, with some measurements finding evidence of a deep third well and others consistent with a double humped barrier. Thus the dialog between theory and experiment could benefit from improved photofission measurements.

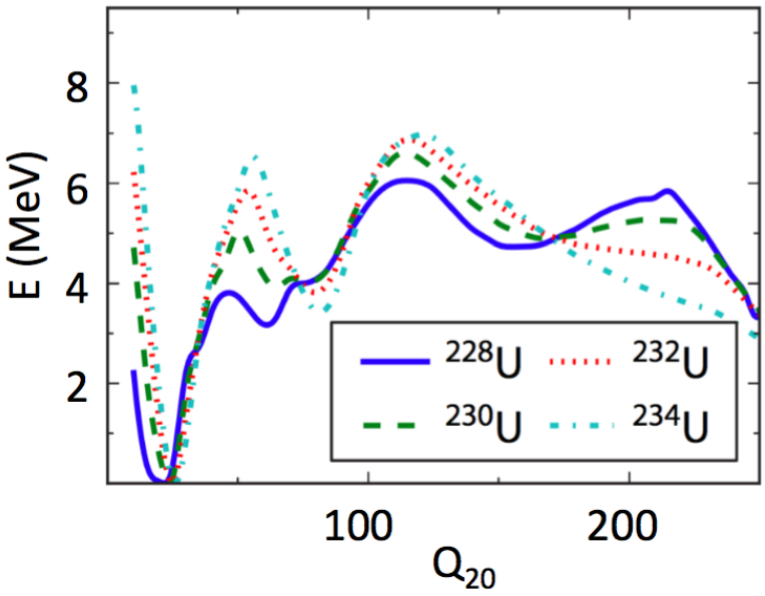

Figure 2.6: Calculated fission barriers for isotopes of uranium calculated with a self-consistent model[28].

CHAPTER 3: PHOTOFISSION THEORY

3.1 Photoabsorption

The motivation for studying fission through photofission measurements may be understood by considering the interaction between the nucleus and the electromagnetic field. Unlike neutron induced fission which brings a large range of angular momenta into the excited compound nucleus, the potential momentum states for photoabsorption are limited by a combination of selection rules and vanishing contributions from higher order multipolarities. To connect an initial state with momentum J_i to a final state with momentum J_f with an electromagnetic interaction with multipolarity l, the following sum rule must be obeyed[32]:

$$|J_i - l| \leq J_f \leq |J_i + l|. \tag{3.1.1}$$

Additionally for an initial state parity π_i and final state parity π_f, $\pi_i\pi_f = (-1)^l$ for electric transitions while $\pi_i\pi_f = (-1)^{l+1}$ for magnetic transitions. The transition rate between those two states is given by[32]

$$T_{fi}(l;R) = \frac{8\pi(l+1)}{l[(2l+1)!!]^2}\frac{k^{2l+1}}{\hbar}|\langle f|\hat{\Omega}_{l\mu}(R)|i\rangle|^2, \tag{3.1.2}$$

where k is the photon wave number, $|\langle f|\hat{\Omega}_{l\mu}(R)|i\rangle|$ is the matrix element containing all the nuclear structure information and R stands for either E or M depending on whether the transition is electric or magnetic. The squared double factorial in the denominator grows at a significantly faster rate as a function of multipolarity than the exponential in the numerator, leading to a suppression of higher order multipolarity contributions. For even-even nuclei like ^{238}U and ^{232}Th which have a $J^\pi = 0^+$ ground state, the dominant dipole interaction will

couple only to $J = 1$ and $J = 2$ excited states. A further limitation in the number of states which contribute to photoexcitations may be found by considering the relative strengths of the electric and magnetic interactions. All electric or magnetic interaction information is contained within the nuclear matrix element, so estimating their respective strengths would require specifying the currents in the nucleus.

A simpler estimate of relative strengths can be made using Weisskopf estimates which are based on electromagnetic, single-nucleon transitions based on a simplistic constant radial wave function confined to the nucleus and an angular momentum part given by a spherical harmonic and a spinor[33]. The ratio of the resulting transition rates is

$$\frac{T(l, M)}{T(l, E)} \approx 0.3A^{-2/3} \tag{3.1.3}$$

which gives an M1 contribution of about 0.8% that of the E1 strength for $A = 230$. Thus in low energy photofission measurements the E1 excitation will be dominant and the most probable mode of excitation will be $J^\pi = 0^+ \rightarrow J^\pi = 1^-$, allowing for much more selective measurements than neutron or heavy ion induced fission. Additionally the k^{2l+1} energy dependence of the transition rate means that the photofission cross section will vary smoothly with γ-ray energy, with the major exception of resonances which will be discussed in the next section.

3.2 Fission Barrier Interpretation

Because of one or more local minima within the fission barrier it is possible for the nucleus to exist in excited states within the fission barrier, with these states having well defined energy, angular momentum, parity and deformation. A schematic spectrum of states which are relevant for low energy fission for an even-even nucleus is shown in Fig. 3.1, with angular momentum and parity J^π and projection of angular momentum on the nuclear symmetry axis K (see Fig. 3.5). The ground state band is a rotational band due to the

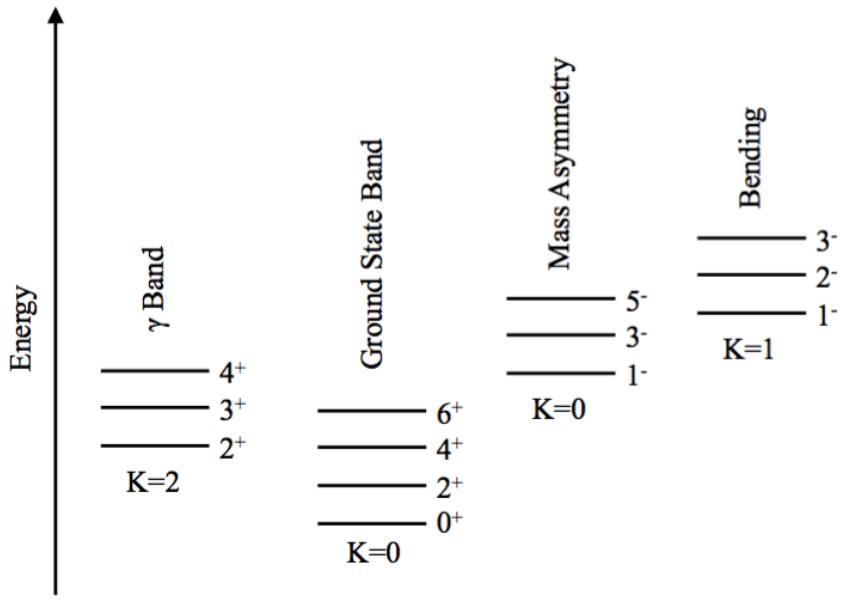

Figure 3.1: Schematic energy level diagram for an even-even nucleus, based on Ref. [34].

permanent deformation of the nucleus. Vibrational modes may also be excited, the simplest of which is a β vibration or "breathing mode" which is inherently unstable due to vibrations in the direction of the fission axis. There is a mass asymmetry mode referred to as "sloshing" corresponding to an inverting pear shaped mass distribution in which the mass asymmetry oscillates back and forth. A class of vibrational states called γ-vibrations are an excitation in which an ellipsoidal oscillation breaks axial symmetry. Finally there is also a "bending mode" in which the two ends of the highly deformed nucleus flex relative to the nuclear center. This collective state has not been identified in the excitation spectrum of nuclei in their ground state, but is expected to be present in the saddle point deformation where the energy of the state would be lower.

The various excited states are expected to occupy primarily one of the local minima within the fission barrier. Fig. 3.2 shows a schematic triple-humped fission barrier with available nuclear states which are grouped into class I, class II or class III by the potential well in which the state is localized. The classification is an idealization, since in reality the tail of a wave function centered in one potential well will penetrate the barrier to mix with states in the other minima, with the degree of mixing dependent on the penetrability of the

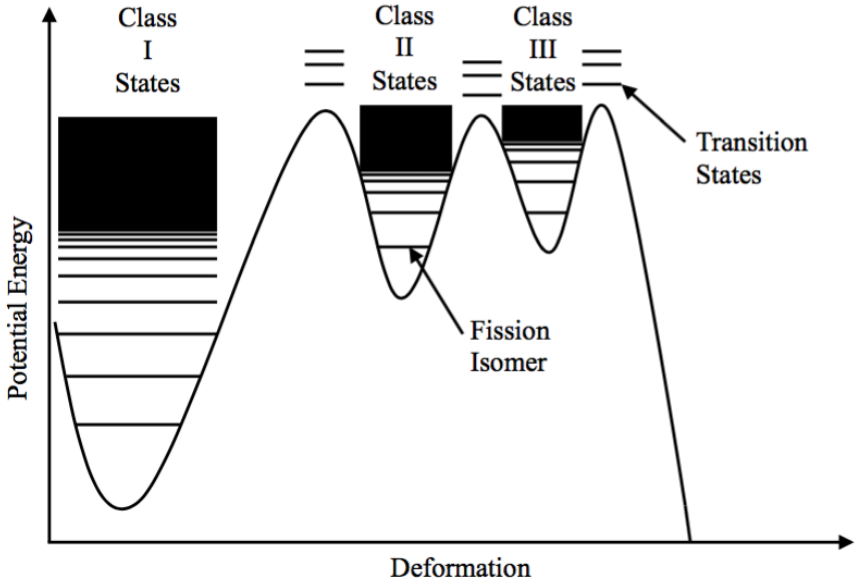

Figure 3.2: Schematic of class I-III isomeric excitation states and transition states within the fission barrier, based on Ref. [22].

internal barriers and the structure of the states involved. In situations where the energy of a class I state is close to that of a class II or III state, a higher degree of mixing can be expected, resulting in an increased probability of the nucleus in a class I excitation state penetrating the full barrier and undergoing scission.

The effect of intermediate states in the potential well of the fission barrier may be illustrated with the relatively simple case of a class I excitation coupling to a class II β vibrational state in a double-humped fission barrier. The calculation is performed for an undamped transition resonance in which the strength of the β-vibrational state is not distributed over neighboring states in the second minimum. The probability of the class I state's undergoing fission can be written as[35]

$$P_{fI} = \frac{D_I}{2\pi} \frac{\Gamma_A \Gamma_B / \Gamma_{\gamma I}}{(E - E_\beta)^2 + W^2/4}, \tag{3.2.1}$$

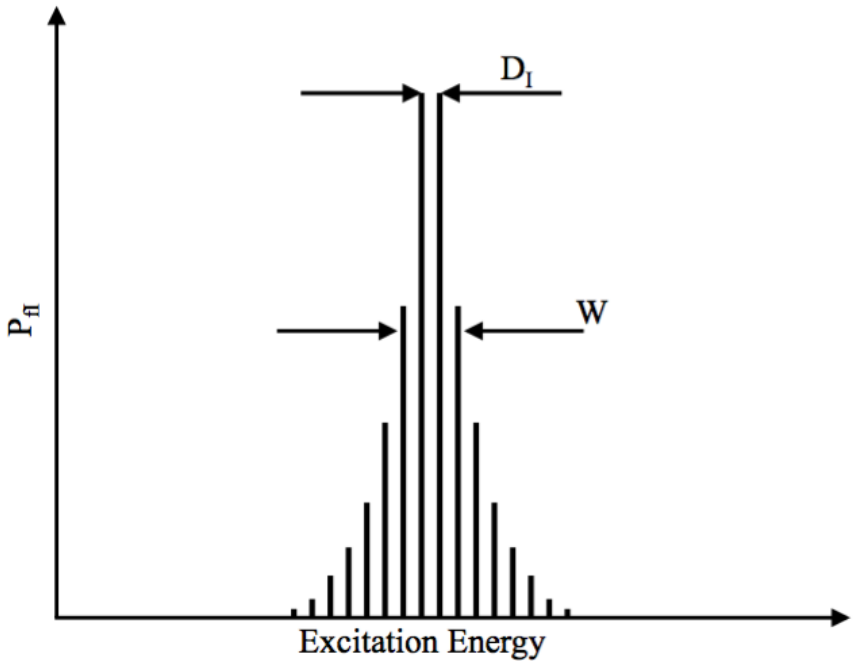

Figure 3.3: Barrier penetration probability for class I states close to the energy of a class II β-vibrational state, with level density D_I and resonance width W.

where the width of the resonance is given by

$$W = \sqrt{(\Gamma_A + \Gamma_B + \Gamma_{\gamma II})^2 + \frac{2}{\pi}\Gamma_A\Gamma_B\frac{D_I}{\Gamma_{\gamma I}}} \tag{3.2.2}$$

and D_I is the level distance between class I states. E and E_β are the energies of the class I and β-vibrational states, E_A and E_B are the inner and outer fission barrier heights, Γ_A and Γ_B are the widths for tunneling through the inner and outer fission barriers, and $\Gamma_{\gamma I}$ and $\Gamma_{\gamma II}$ are the γ-decay widths for states in the first and second minima. The widths $\Gamma_{A,B}$ can be calculated using the Hill-Wheeler transmission coefficient $P_{A,B}$[22] as[35]

$$\Gamma_{A,B} = P_{A,B}\frac{\hbar\omega_{II}}{2\pi} = \left[1 + e^{\frac{2\pi(E_{A,B}-E)}{\hbar\omega_{A,B}}},\right]^{-1}\frac{\hbar\omega_{II}}{2\pi} \tag{3.2.3}$$

where $\hbar\omega_{II}$ is the phonon energy of the β-vibration, and $\hbar\omega_{A,B}$ is curvature of the parabolic

barrier minima. The fission cross section is then given by

$$\sigma = \sigma_{cI} P_{fi}, \tag{3.2.4}$$

where σ_{cI} is the cross section for the formation of the compound class I state in the first minimum.

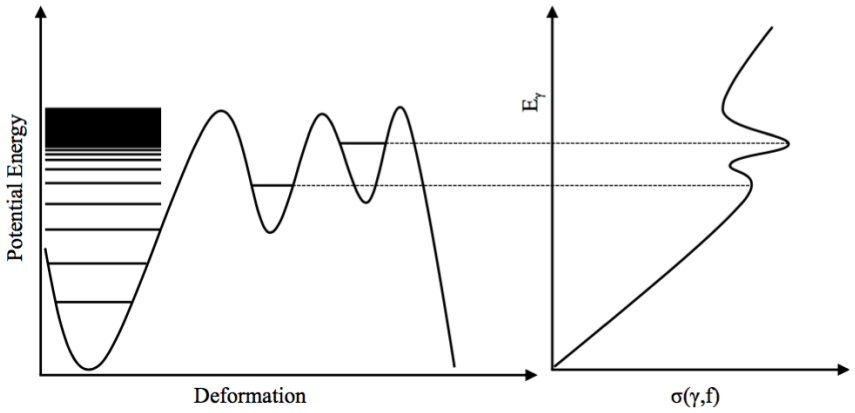

Figure 3.4: Schematic diagram of photofission resonances due to transition states in the fission barrier, based on Ref. [22].

A schematic plot for P_{fI} is shown in Fig. 3.3 with a strong enhancement in the fission probability of excited states with energies close to the class II β-vibrational state. Thus the presence of states within the fission barrier leads to resonances in the photofission cross section. The assumption that fission primarily occurs by tunneling through the barrier via one of these states means that each transition state can be thought of as a separate channel for fission. The transition states are made particularly distinct by their large level spacing when compared with the $\sim$ 1eV level spacing around 6 MeV excitation energy for the ground state nucleus. This level spacing is a consequence of the fact that a majority of the excitation energy goes into deformation. The deformed nucleus then behaves like a cold, ground state nucleus with large level spacing between the lowest energy transition states. Observations of resonances in high resolution measurements of the photofission cross section can then be used to map out the fission barrier as shown in Fig. 3.4. The experimentally accessible cross

section resonances will be broadened by damping of the vibrational state, and additionally will be limited by the resolution of the probing γ-ray beam.

3.3 Fission Fragment Angular Distributions

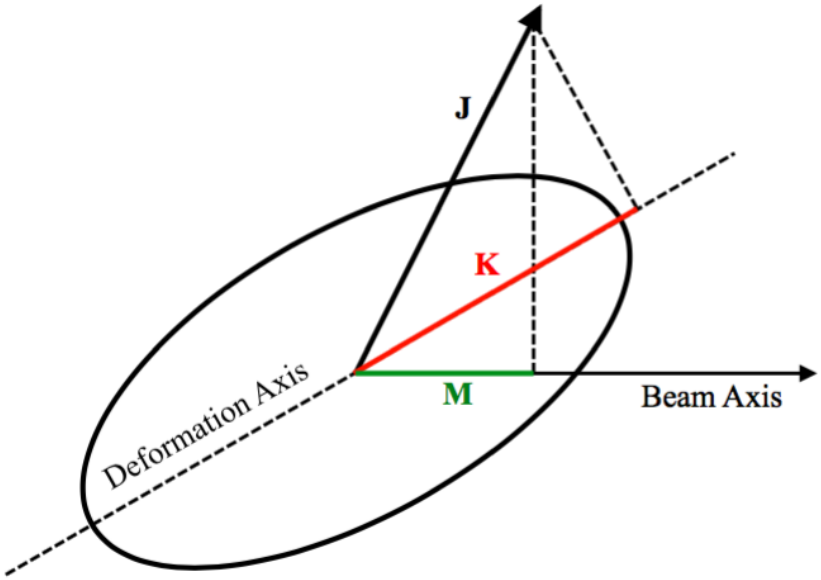

Figure 3.5: J, K and M quantum numbers for the transition nuclear states in Bohr formalism.

The first theoretical model of fission to describe the angular distribution of the fission fragments was developed by A. Bohr[17], using the fission channels described in section 3.2. The deformed nucleus (see Fig. 3.5) is described using the quantum numbers J, K and M where J is the total angular momentum, K is the projection of J onto the nuclear symmetry axis, and M is the projection of J onto a space-fixed axis which for the remainder of this work will be taken to be the beam axis.

As the nucleus traverses the fission barrier J and M will remain constant by virtue of momentum conservation. However, K has no such restriction; it is reasonable to assume that the nucleus will undergo many different deformations and vibrations throughout the fission barrier. However Bohr's model assumes that once the nucleus reaches the saddle point in a particular (J,K,M) state, those quantum numbers will remain good until scission. At

that point the two nascent fragments will be repelled by mutual Coulomb repulsion and fly apart along the nuclear symmetry axis. The angular distribution of the fission fragments is then given as the angular distribution of the nuclear symmetry axis. The saddle point configuration of the nucleus may be treated as a spinning symmetric top with the well known angular distribution

$$W^J_{MK}(\theta) = \frac{2J+1}{2}|d^J_{M,K}(\theta)|^2, \tag{3.3.1}$$

where $d^J_{M,K}(\theta)$ are the Wigner rotation functionals given by[36]:

$$\begin{aligned} d^J_{M,K}(\theta) = &\sum_n (-1)^{n-K+M} \frac{\sqrt{(J+K)!(J-K)!(J+M)!(J-M)!}}{(J+K-n)!n!(J-n-M)!(n-K+M)!} \\ &\times \left(\cos\frac{\theta}{2}\right)^{2J-2n+K-M} \left(\sin\frac{\theta}{2}\right)^{2n-K+M}. \end{aligned} \tag{3.3.2}$$

However, $\pm K$ are indistinguishable from one another given that either results in the same fission axis, so they are given equal weight and summed. Consequently K may be taken to be $|K|$. In the special case of photofission of an even-even nucleus, M can only have the values ± 1, so the two cases may be summed over with equal weight as

$$W^J_K(\theta) = \frac{2J+1}{2}\left(\frac{1}{2}\right)\left[|d^J_{+1,K}(\theta)|^2 + |d^J_{-1,K}(\theta)|^2\right]. \tag{3.3.3}$$

Equation 3.3.3 describes the angular distribution of fission fragments from an unpolarized beam. When the incident γ-ray beam polarization is accounted for, the distribution becomes[37]

$$W^J_K(\theta,\phi) = \frac{2J+1}{2}\left(\frac{1}{2}\left[|d^J_{+1,K}(\theta)|^2 + |d^J_{-1,K}(\theta)|^2\right] + P_\gamma \omega_L cos2\phi d^J_{+1,K}(\theta) d^J_{-1,K}(\theta)\right), \tag{3.3.4}$$

where ω_L is $+1$ for electric transitions and -1 for magnetic transitions, ϕ is the angle relative

to the polarization axis and P_γ is the degree of polarization of the beam given by

$$P_\gamma = \frac{N_{||} - N_\perp}{N_{||} + N_\perp}. \tag{3.3.5}$$

Here $N_{||}$ is the number of photons polarized parallel to the choice of polarization axis and $N_\perp$ is the number with the opposite polarization state. To express the angular distributions from contributing fission channels, recall from section 3.1 that both magnetic and higher multipolarity transitions will be suppressed and can be neglected. Considering only electric dipole and quadrupole transitions the angular distributions of the fission fragments are shown in Table. 3.1, where a 100% polarized beam has been assumed. A polarization asymmetry $\Sigma(\theta)$ is defined as

$$\Sigma(\theta) = \frac{W(\theta, 0) - W(\theta, \pi/2)}{W(\theta, 0) + W(\theta, \pi/2)} \tag{3.3.6}$$

which is equal to the difference in the yield in the plane of polarization and out of the plane of polarization divided by the total. In Table. 3.1 the polarization asymmetry has been evaluated at $\theta = 90°$, or perpendicular to the beam axis. The observed fission fragment angular distribution will be a linear combination of the $W_K^J(\theta, \phi)$ distributions weighted by the relative contribution of each fission channel (J, K). If the angular distributions for the electric dipole and quadrupole excitations are summed with relative weighting coefficients, the resulting angular distribution will have the form

$$W(\theta, \phi) = a + b\sin^2(\theta) + c\sin^2(2\theta) + \cos(2\phi)[b\sin^2(\theta) + c\sin^2(2\theta)], \tag{3.3.7}$$

where c is an energy dependent coefficient that corresponds to quadrupole excitations and b contains both quadrupole and dipole terms.

For low excitation energies where the higher order multipole transitions are further suppressed, the quadrupole terms may be neglected in favor of just the (1,0) and (1,1)

J	K	$W(\theta,\phi)$	$\Sigma(90°)$
1	0	$\frac{3}{4}\sin^2\theta + \frac{3}{4}\cos 2\phi sin^2\theta$	1
1	1	$\frac{3}{4} - \frac{3}{8}\sin^2\theta - \frac{3}{8}\sin^2\theta\cos 2\phi$	-1
2	0	$\frac{15}{16}\sin^2 2\theta + \frac{15}{16}\cos 2\phi\sin^2 2\theta$	0
2	1	$\frac{5}{4} - \frac{5}{8}\sin^2\theta - \frac{5}{8}\sin^2 2\theta + \frac{5}{8}\sin^2\theta\cos 2\phi - \frac{5}{8}\sin^2\theta\sin^2 2\phi$	1
2	2	$\frac{5}{8}\sin^2\theta + \frac{5}{32}\sin^2 2\theta - \frac{5}{8}\sin^2\theta\cos 2\phi + \frac{5}{32}\sin^2 2\theta\cos 2\phi$	-1

Table 3.1: Angular distributions of E1 and E2 transition states of even-even nuclei for polarized beam in the Bohr formalism.

electric dipole transitions. This assumption simplifies the angular distribution to

$$W(\theta,\phi) = a + b\sin^2(\theta) + b\cos(2\phi)\sin^2(\theta), \tag{3.3.8}$$

where a and b are normalized so that $a + b = 1$. The polarization asymmetry then reduces to

$$\Sigma(\theta) = \frac{b\sin^2(\theta)}{a + b\sin^2(\theta)} \tag{3.3.9}$$

and $\Sigma(90°) = b$. The relative contributions of the fission channels may then be probed by measurements of the polarization asymmetry.

A potential flaw in Bohr's formalism was pointed out by Kadmensky[38] in the assumption that the fission fragments are emitted exactly along the nuclear deformation axis. From the uncertainty relation between the nuclear deformation axis and the orbital angular momentum l of the fragments, if the deformation axis is perfectly known then the angular momentum is completely undefined. This leads to contributions from $0 \leq l \leq \infty$, where the high l contributions are completely unphysical.

Kadmensky addresses this issue by developing his own formalism[38][39][40] in which the uncertainty relation smears the distribution of the fission fragments appropriately. The contributing l states are explicitly summed over the range $0 \leq l \leq l_m$ where l_m is the maximum contributing angular momentum. When $l_m = \infty$ the Kadmensky formalism reproduces the

Bohr predictions but it deviates for finite l_m values. If l_m is estimated to be ~ 25 by summing the final spins of the fission fragments and the spins carried by prompt γ-rays and neutrons emitted during fission[39], the fission fragment angular distributions predicted by Kadmensky differ from Bohr's predictions by only a few percent. Given the good agreement between Bohr and Kadmensky approaches, for the purposes of the present work the Bohr formalism is sufficient for adequately describing the angular distribution of the fission fragments.

The fission channel formalism has been remarkably successful at describing the angular distributions of fission fragments, with a wealth of of experimental measurements in agreement with the predicted features of the distributions[15][41][42][43]. As will be described in the next section, information about the angular distribution of the fission fragments is also carried by the neutrons emitted during fission.

3.4 Fission Neutrons

A majority of the energy released by fission goes towards accelerating the fission fragments, and is expressed as their kinetic energy. The remaining fission energy exists in the fragments either as internal excitation energy or stored as deformation which is then converted to excitation energy when the fragments relax to their equilibrium shape. The fragments can then de-excite by emitting neutrons and γ-rays. The rest of this section (and the present work) will focus on the neutrons emitted by fission fragments. Since the energy to liberate neutrons depends on the mass division, compound nuclear excitation energy, and kinetic energy release of fission, fission neutrons provide an avenue for gaining insight into the fission process.

Neutrons emitted during the fission process may be grouped into three distinct timescales: pre-scission and scission, prompt, and delayed. Pre-scission and scission neutrons are emitted just before, during, or immediately after scission by one of several possible processes. The dominant process is thought to be emission at the time when the nucleus separates[44].

As the nucleus moves from saddle to scission, the connection between the two binary components which will ultimately separate can be characterized as a thin neck with shrinking diameter. At scission the neck ruptures and the remaining stubs are absorbed into the nascent fragments. In that moment the neutrons can still be described by their pre-scission wave functions, but now find themselves in a new potential created by the separated fragments. The neutron wave functions can couple to the continuum and neutrons can be emitted. Scission neutrons are characterized by their angular distribution as they are emitted from a stationary nucleus or fragment. The resulting distribution is thought to be mostly isotropic, with small anisotropies caused by the scattering and absorption of the neck neutrons by the fission fragments[45]. Scission neutrons are estimated to contribute on the order of at most 10% of the total fission neutrons[4].

Prompt fission neutrons constitute the vast majority of neutrons emitted during fission, with 2-4 typically emitted in a fission event. These neutrons are assumed to be emitted by the fully accelerated fission fragments and therefore have an angular distribution which is correlated with that of the fragments. This assumption can be shown to be reasonable by considering the timescales for fragment acceleration and neutron emission. The fission fragments will be fully accelerated from mutual Coulomb repulsion with a timescale of 10^{-20} s[4]. The neutron emission timescale of the excited fragment has been calculated with a statistical model as[46]

$$\tau = \frac{2A^{1/3}}{U - B_n} e^{B_n/T} \times 10^{-21}\,\text{s}, \tag{3.4.1}$$

where τ is the lifetime of the excited fragment state prior to neutron emission, A is the fragment mass (~ 100), U is the excitation energy of the fragment (taken to be on the order of 10 MeV), B_n is the neutron binding energy (~ 5 MeV) and T is the temperature of the nucleus, given by

$$T = \sqrt{\frac{10(U - B_n)}{A}}. \tag{3.4.2}$$

With this order of magnitude estimate, the neutron emission timescale is $\sim 10^{-18}$ s, two

orders of magnitude longer than the fragment acceleration timescale. Thus the neutrons can be treated as being emitted by fully accelerated fission fragments.

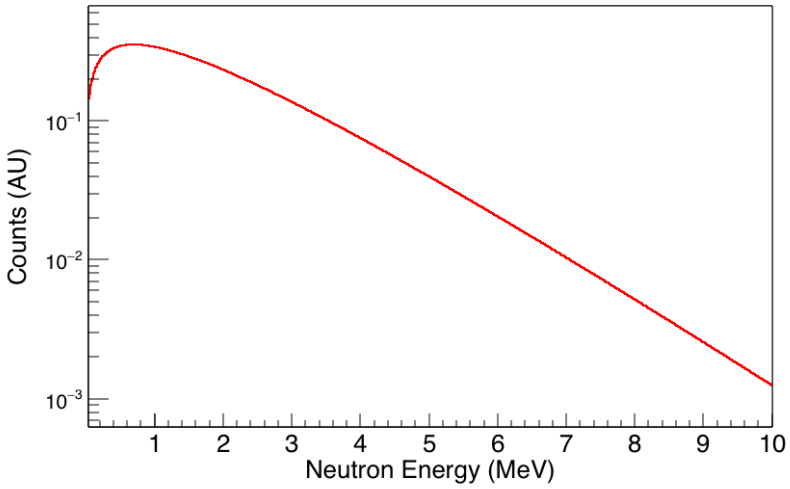

Figure 3.6: Calculated neutron spectrum for ^{238}U(γ,f) at $E_\gamma = 10$ MeV, using Watt parameters from Ref. [47].

It is usually assumed that the prompt fission neutrons are emitted isotropically in the fragment rest frame, "boiling" off the hot nucleus with no preferred direction. This simplification ignores anisotropies in neutron emission caused by fragment deformation, in which neutrons will be preferentially emitted at the narrow ends of a deformed nucleus where the nuclear binding force is reduced. For the purposes of the present work these effects are considered to be negligible compared with the anisotropies introduced by the boost the emitted neutrons receive from the fission fragment. Using an evaporative model the spectrum of the neutrons in the fragment rest frame is given by[4]

$$P(E_n) \propto E_n e^{E_n/T}, \tag{3.4.3}$$

where $P(E_n)$ is the probability of emitting a neutron with energy E_n and T is the temperature of the nucleus. The spectrum may be thought of as a Maxwell-Boltzman distribution weighted by the neutron velocity ($\sqrt{E_n}$) to bias towards emitting faster neutrons.

Following conversion from the fragment rest frame to the laboratory frame, the prompt fission neutrons receive a significant boost as the fragment is traveling at approximately 1 MeV/nucleon. The neutron spectrum in the laboratory frame is given by the Watt spectrum[4]

$$P(E_n) \propto e^{-E_n/T} \sqrt{\sinh\left(\frac{4E_nE_f}{T^2}\right)}, \tag{3.4.4}$$

where E_f is the fragment energy per nucleon. A calculated Watt spectrum is shown in Fig. 3.6 for the photofission of ^{238}U with $E_\gamma = 10$ MeV.

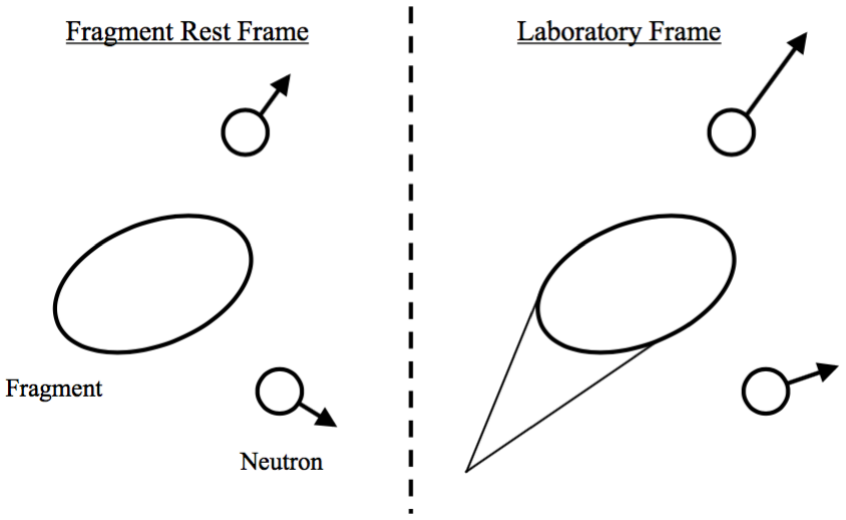

Figure 3.7: Diagram showing the effect of the boost from the fission fragment on the prompt fission neutrons. The arrow lengths correspond to the relative velocities of the fragments and neutrons.

In addition to influencing their energy spectrum, the boost from the energetic fission fragments has a significant impact on the angular distribution of the prompt fission neutrons. Fig 3.7 shows the effect of the boost caused by the moving fragment on the neutrons; those which are emitted in the direction of the fragment motion receive the largest boost in energy. The overall prompt neutron angular distribution will resemble a smeared version of the fission fragment angular distribution, with an additional energy dependence where the distribution of the highest energy neutrons will most closely match underlying fragment distribution. This correlation between neutron energy and emission angle is explored in more detail in

section 7.4.

After fully de-exciting and coming to a stop the fission fragments are still capable of emitting delayed neutrons, which follow a β-decay of the fragment in the rare situation where the β-decay energy of the parent nucleus is greater than the neutron binding energy of the daughter nucleus. Delayed neutrons are emitted on timescales of milliseconds to minutes after fission, and consequently do not contain any information about the energetics of the fission process or the angular distribution of the fragments. The contribution of delayed neutrons to the total fission neutrons is on the order of $\sim 1\%$[4] and can be neglected for the purposes of this work.

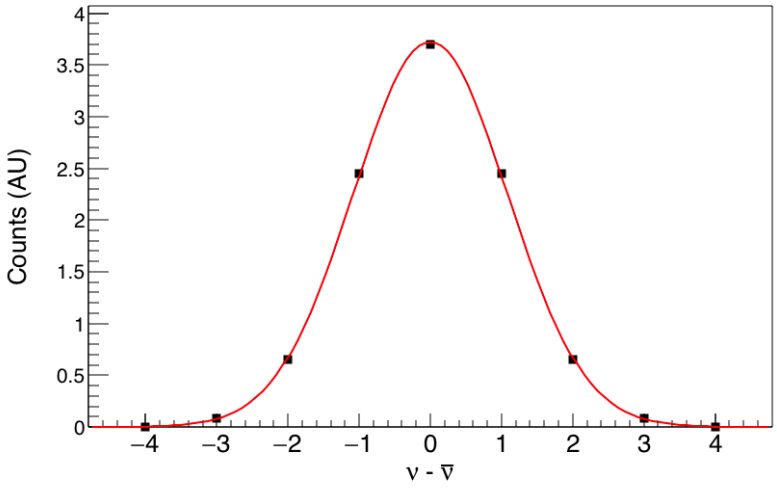

Figure 3.8: Schematic prompt fission neutron multiplicity distribution, relative to the mean multiplicity $\overline{\nu}$. The multiplicity distribution is modeled as a Gaussian function with a mean $\overline{\nu}$ and a spread $\sigma = 1.08$.

In addition to their energy spectrum and angular distribution, prompt fission neutrons are characterized by their multiplicity, or the number of neutrons emitted per fission. Since the prompt fission neutrons are emitted through an evaporative process, the multiplicity for a particular event is purely statistical. Fission neutron multiplicity distributions are typically Gaussian, with a mean $\overline{\nu}$ between 2 and 4 and a standard deviation σ of 1 to 1.5. A sample multiplicity distribution for fission is shown in Fig. 3.8, centered around the mean neutron

multiplicity $\overline{\nu}$. In general the mean of the multiplicity distribution increases with increasing excitation energy of the fissioning nucleus in a linear fashion. The potential modifications to this general rule at excitation energies well below the fission barrier as will be discussed in section 4.4.

The fission neutron multiplicity is sensitive to the prompt neutron emission mechanism as well as the properties of the fission fragments: kinetic energies, excitation energies and masses. The relationship between the mass of a fission fragment and the number of emitted neutrons is shown in Fig. 3.9 for ^{239}Pu(n_{th},f). Rapid changes in the multiplicity distribution would therefore be indicative of a change in the contributing fission modes such as the availability of a new fission channel. In summary, prompt photofission neutrons contain a wealth of information about the energetics of the fission process, and represent a valuable tool for photofission measurements.

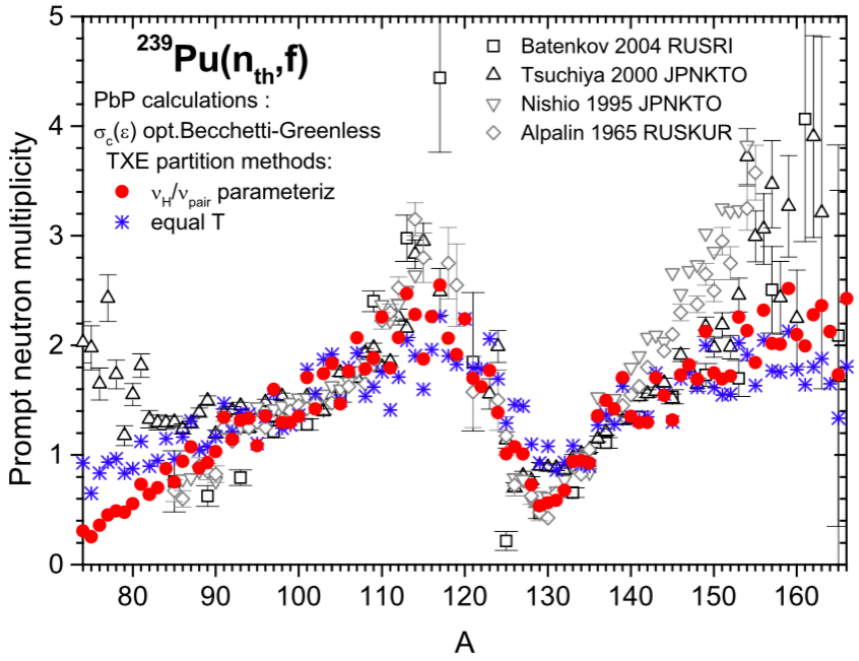

Figure 3.9: The number of neutrons emitted by a fission fragment as a function of the fission fragment mass for ^{239}Pu(n_{th},f)[48]. Experimental data (black and white markers) are compared with theoretical point-by-point calculations with different methods for partitioning the excitation energy between the pair of fission fragments (red and blue markers).

CHAPTER 4: PREVIOUS PHOTOFISSION MEASUREMENTS

4.1 Introduction

There have been many photofission measurements performed in the study of the fission process. This chapter will focus on describing the measurements which probe the properties of photofission at sub-barrier energies. There has been much debate and disagreement between theoretical predictions and experimental measurements over the existence of a well formed third minimum in the fission barrier of many nuclei. Theoretical calculations generally predict a shallow or nonexistent third minimum. The number of experimental results supporting the existence of deep third minima in a number of actinides has been growing in recent years, with data collected through a variety of experimental techniques including transfer reactions[49][50][51], neutron induced fission and photofission[13]. Fission barrier parameters are crucial inputs for cross section calculations on the Th-U fuel cycle of next generation nuclear reactors. The selectivity of photofission measurements allows for the investigation of fission resonances in the first and second potential energy minima.

For this work, ^{232}Th and ^{238}U have been chosen as the isotopes of interest because for both nuclei there have been measurements consistent with a triple-humped fission barrier which are not supported by theoretical calculations. The existing cross section measurements and their analysis will be discussed in section 4.2. A previous measurement of the prompt photofission neutron polarization asymmetries for ^{232}Th and ^{238}U will be described in section 4.3, and the existing prompt neutron multiplicity data will be covered in section 4.4.

4.2 Photofission Cross Sections

4.2.1 Photofission of ^{232}Th

There are about a dozen measurements of the ^{232}Th(γ,f) reaction cross section below $E_\gamma = 6$ MeV available in the literature, and 10 have been listed in table 4.1. To put the region of the photofission cross section spanned by this collection of data into perspective, Fig. 4.1 shows the experimentally measured ^{232}Th(γ,f) reaction cross section over the full giant dipole resonance (GDR), between 10 MeV and 20 MeV, where the cross section reaches its maximum. By far the measurement with the highest precision at low energies is the one performed by Smirenkin and Soldatov[52]. Bremsstrahlung γ-ray beams produced by microtron driven electron beams were directed onto a 0.1mm thick ^{232}Th foil, which was monitored by mica plates on either side. Fission fragments were detected by the tracks they left in the mica plates. Because of the broad nature of the bremsstrahlung spectrum, the fission cross section is integrated over the overlap of the γ-ray beam spectrum. The underlying photofission cross section is then determined using an iterative unfolding technique. Measurements were taken with electron beam energy steps of 25 keV to allow for high resolution studies of the cross section.

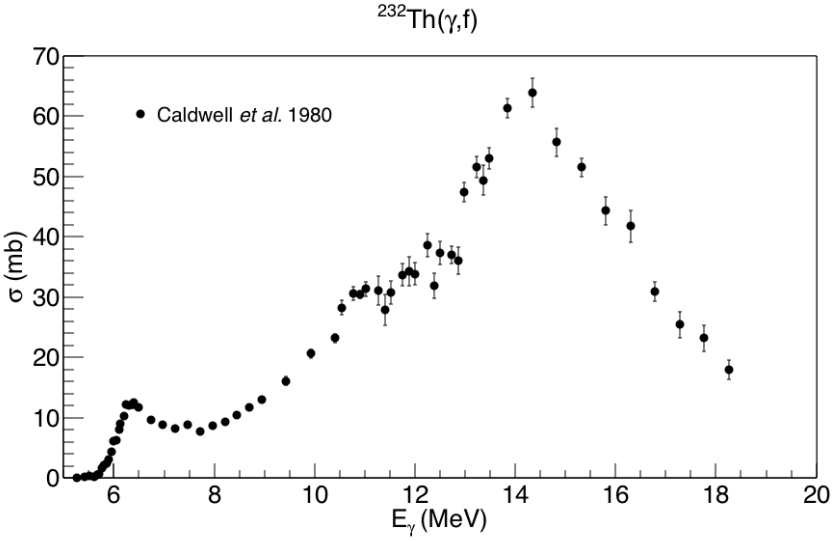

Figure 4.1: ^{232}Th(γ,f) reaction cross section over the GDR[58]. The present work measures the region below 6 MeV.

First Author	Year	E_γ Range (MeV)	Beam	Spread	σ_{sys}	σ_{stat}
Rabotnov[53]	1970	5.17-7.6	Brem.	Brem.	n/a	19%
Mafra[54]	1972	5.43-9	(n,γ)	mono	"appreciable"	80%
Yester[55]	1973	5-8	(n,γ) Compton	n/a	30%	67%
Dickey[56]	1975	5.1-7.9	Tagged-γ	2%	15%	126%
Bowman[57]	1978	3.5-5.5	Brem.	Brem.	"perhaps a factor of 2"	48%
Caldwell[58]	1980	5.3-18	e^++e^-	6%	7%	15%
Knowles[59]	1982	4.96-6.76	Tagged-γ	0.2%	20%	28%
Zhang[60]	1986	5.8-11.9	(p,γ)	10%	10%	6%
Findlay[61]	1986	5.32-7.11	Brem.	Brem.	10%	8%
Smirenkin[52]	1995	4.78-8.88	Brem.	Brem.	"disregard errors"	7%

Table 4.1: Previous measurements of the ^{232}Th(γ,f) reaction cross section at energies below 6 MeV. Quoted statistical uncertainties are given for the closest data point to $E_\gamma = 5.5$ MeV.

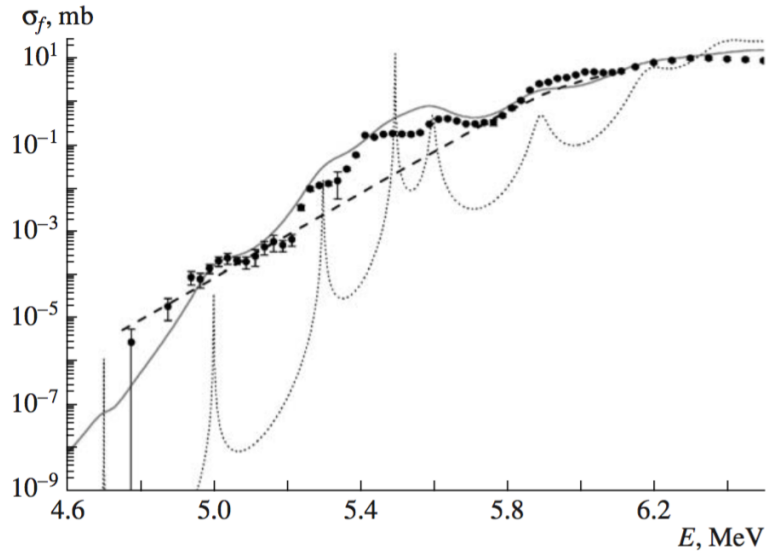

Figure 4.2: Measured ^{232}Th(γ,f) reaction cross section[52] with cross section calculated from barrier fit[62]. The dotted curve is the calculated photofission cross section without including damping, which would allow for the vibrational transition states to interact with other states within the fission barrier. The solid curve is the calculated photofission cross section with damping. The dashed curve is a characterization of the exponential part of the photofission cross section and may be disregarded for the present work.

The data were then re-analyzed[62] to determine the structure of the ^{232}Th fission barrier. The authors attempted to reproduce the measured photofission cross sections by assuming some barrier structure and calculating the resulting penetrability and cross section, and then tuning the parameters of the barrier to improve the fit. A comparison between the measured and calculated cross sections is shown in Fig. 4.2. There are some deviations, particularly in the region of $5.3 - 5.6$ MeV, but overall the fit is in agreement with the measured cross section.

The fission barrier structure of the best fit is shown in Fig. 4.3, with a 1.8 MeV deep third minima being necessary to reproduce the observed cross section. The fission barrier is characterized by the heights of the maxima, E_{A-C}, the heights of the minima, E_{I-III}, and the curvature of the potential energy surface at the maxima and minima $\hbar\omega_{1-5}$. This inferred third well is significantly deeper than the well depth of $< 0.5MeV$ predicted by theoretical calculations of the ^{232}Th fission barrier[29][26][28]. The stark disagreement between

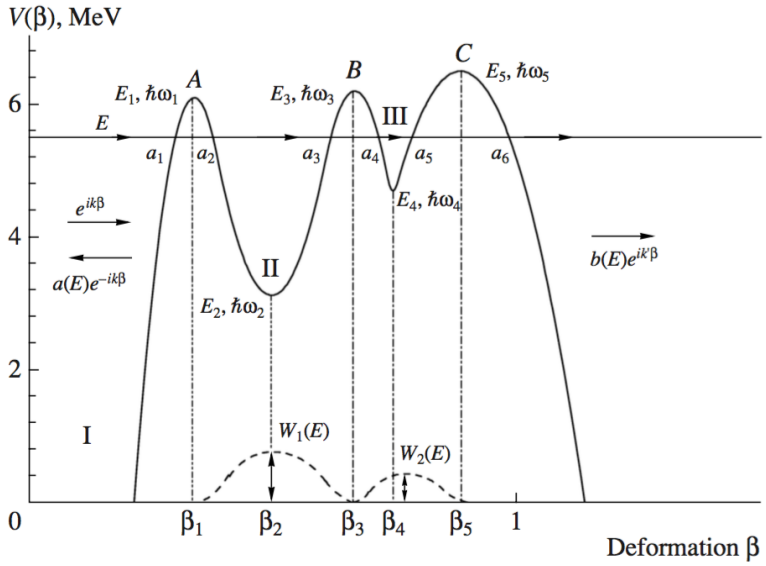

Figure 4.3: Inferred fission barrier structure for ^{232}Th[62].

theoretical predictions and the experimentally determined third minimum warrants further investigation. Currently there is only a single set of ^{232}Th(γ,f) cross section measurements which covers the excitation energy range where resonances associated with the third minimum are expected[52]. The lack of systematic error analysis for the measurement justifies a new validation measurement. The γ-ray beams used in the present work had a broader energy resolution ($\sim$ 300 keV) than what was achieved in the previous work by unfolding bremsstrahlung data taken in 25 keV steps, but the present work will be able to measure the magnitude of the ^{232}Th photofission cross section with significantly improved systematic errors.

4.2.2 Photofission of ^{238}U

The ^{238}U(γ,f) reaction cross section over the GDR is shown in Fig. 4.4. There are 8 recent measurements of the ^{238}U(γ,f) reaction cross section which extend below 6 MeV, of which 3 have sufficiently small errors and large enough coverage of the excitation energy region of interest to be discussed. The earliest of these measurements was performed by Dickey and Axel[56] with a nearly mono-energetic tagged photon beam. In that experiment, 8.4 or 9.7 MeV electrons produced by a superconducting linac were directed onto a converter

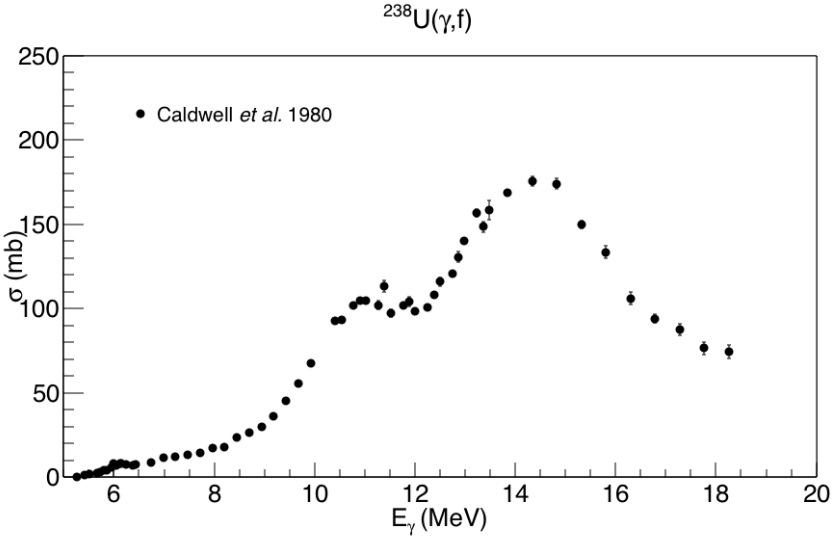

Figure 4.4: ^{238}U(γ,f) reaction cross section over the GDR[58]. The present work will measure the region below 6 MeV.

thin enough that the electrons were likely to only interact once at most, producing a single bremsstrahlung γ-ray. The scattered electron was detected with an electron spectrometer to determine the energy of the γ-ray, given by the difference between the energy of the electron beam and the scattered electron energy.

Photofission neutrons were detected with NE213 liquid scintillator neutron detectors. Pulse shape discrimination was used to suppress γ-ray backgrounds. Additionally the time-of-flight between the pulsed γ-ray beam being incident on the target and the neutron being detected was used to reject uncorrelated neutrons and separate the lower energy neutrons from the ^{238}U(γ,n) reaction. The ^{238}U(γ,f) cross section was determined by only including neutrons with energy greater than 300 keV, as they could only be produced by fission.

The second measurement of the ^{238}U(γ,f) reaction cross section was performed by Caldwell and Dowdy using γ-ray beams from in-flight positron annihilation[58]. Mono-energetic positron beams were directed onto a thin Be converter where they would annihilate on an electron to produce two γ-rays, with a strongly forward peaked beam because of the momentum of the positron. The γ-ray beam was collimated to a half-angle divergence of 7.24 mrad to improve the resolution of the beam to 5%.

First Author	Year	E_γ Range (MeV)	Beam	Spread	σ_{sys}	σ_{stat}
Manfredini[63]	1965	5.4-7.7	(n,γ)	Mono.	10%	16%
Rabotnov[53]	1967	4.8-8	Brem.	Brem.	n/a	79%
Mafra[54]	1972	5.4-9	(n,γ)	Mono.	"Appreciable"	20%
Kahn[64]	1972	5-8.4	(n,γ)	5%	22%	60%
Anderle[65]	1973	5-8	(n,γ)	5%	30%	56%
Dickey[56]	1975	5.1-7.8	tagged-γ	mono	15%	50%
Caldwell[58]	1980	5.3-18	e^++e^-	5%	7%	16%
Csige[13]	2013	4.8-6.1	HIγS	3%	n/a	5%

Table 4.2: Previous measurements of the ^{238}U(γ,f) reaction cross section at energies below 6 MeV. Quoted statistical uncertainties are given for the closest data point to $E_\gamma = 5.5$ MeV.

Photofission neutrons were detected with a neutron detector consisting of 48 BF_3 proportional counter tubes, each 2.54 cm in diameter and 51 cm in length, embedded in 4 coaxial rings within a 61 cm cube of paraffin moderator. Each ring of 12 proportional counters was read out separately since the ratio of counts from one ring to another can be used to determine the average neutron energy. Additionally, the delay between γ-ray beam pulses was sufficiently long that neutrons from one fission event would be fully detected or escape the detector before the next beam pulse, allowing for the prompt neutron multiplicities to be measured.

The most recent measurement of the ^{238}U cross section was performed by Csige *et al.*[13], who measured the fission fragments directly instead of the neutrons they emit. An array of 23 $^{238}UO_2$ parallel plate avalanche counters was exposed to an inverse Compton scattered γ-ray beam produced by the HIγS facility. The production and properties of γ-ray beams generated at HIγS will be discussed in more detail in section 5.3. Both fission fragments were detected in coincidence to suppress α-decay backgrounds, with an estimated 70% efficiency. The flux of the γ-ray beam was measured by placing a thin copper plate in the beam path and detecting the Compton scattered γ-rays with a 120% high purity germanium detector

(HPGe).

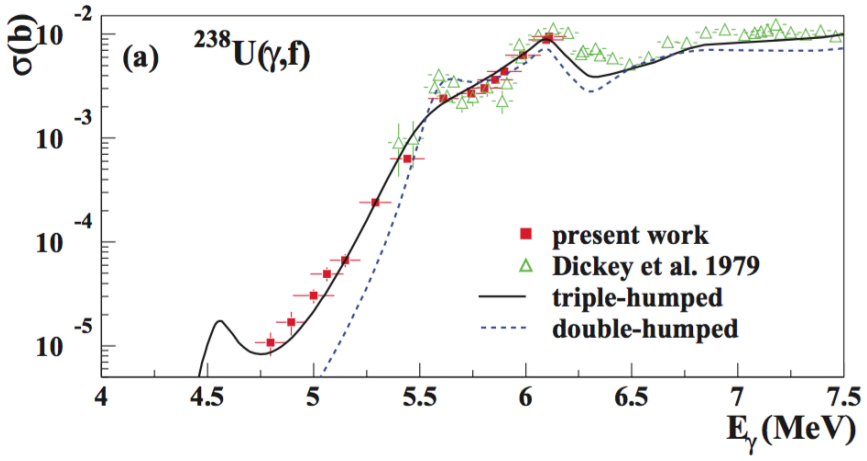

Figure 4.5: Measured ^{238}U(γ,f) reaction cross section compared with calculated cross sections for double- and triple-humped fission barriers[13].

The measured photofission cross section is shown in Fig. 4.5, along with calculated cross sections from an inferred double- and triple-humped fission barrier. The theoretical evaluation of the cross section was calculated using the EMPIRE-3.1 code[66], which determines the fission transmission coefficients with Hill-Wheeler formalism[67] followed by Hauser-Feshbach statistical model calculations[68] to allow the fission channel to compete with neutron emission. The fission barriers were extracted by tuning the barrier heights and curvatures and comparing the resulting photofission cross section to the experimental data. The authors were unable to reproduce the larger than expected cross sections at the low energy side of the fission excitation function measurement without including a third minimum in the fission barrier, as shown in Fig. 4.6, with the low energy tail of the cross section attributed to a potential resonance due to the third minimum at 4.55 MeV. A direct measurement of this resonance would validate the triple-humped barrier interpretation, and is one of the main motivations for the present work.

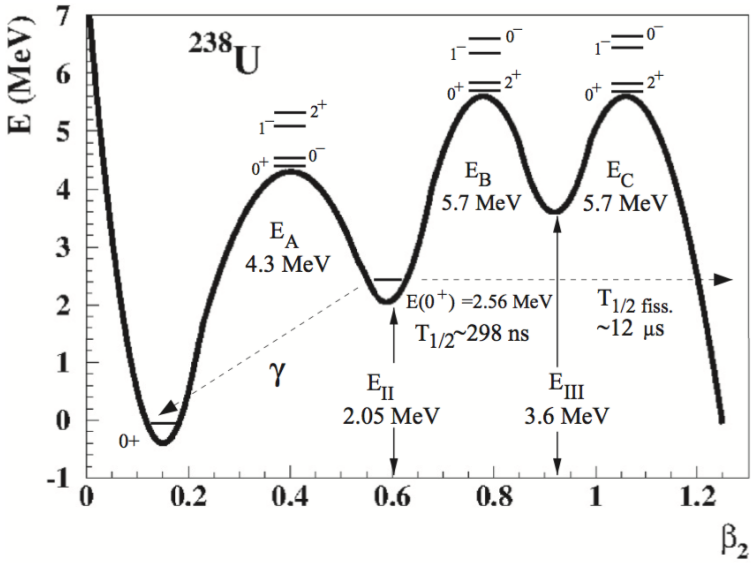

Figure 4.6: Inferred fission barrier structure for ^{238}U[13].

4.3 Photofission Neutron Polarization Asymmetries

There has only been one experimental measurement of the prompt neutron polarization asymmetries in the photofission of ^{232}Th and ^{238}U, performed by Mueller *et al.*[14][69][70]. The experiment used linearly-polarized γ-ray beams provided by HIγS to induce photofission in ^{232}Th and ^{238}U as well as other actinides and detected the photofission neutrons with an array of 18 BC-501A liquid scintillator neutron detectors (see Fig. 4.7). Pulse shape discrimination and time-of-flight cuts were used to suppress γ-ray backgrounds.

Figure 4.7: Neutron detector arrangement for Mueller *et al.*[14].

The measured polarization asymmetries for ^{232}Th and ^{238}U are shown in Fig. 4.8. The neutron polarization asymmetry is defined as

$$\Sigma_n(\theta) = \frac{W(\theta,\phi=0) + W(\theta,\phi=180) - W(\theta,\phi=90) - W(\theta,\phi=270)}{W(\theta,\phi=0) + W(\theta,\phi=180) + W(\theta,\phi=90) + W(\theta,\phi=270)} \tag{4.3.1}$$

where $W(\theta,\phi)$ is the neutron yield at a polar angle relative to the beam axis θ and azimuthal angle relative to the polarization axis ϕ.

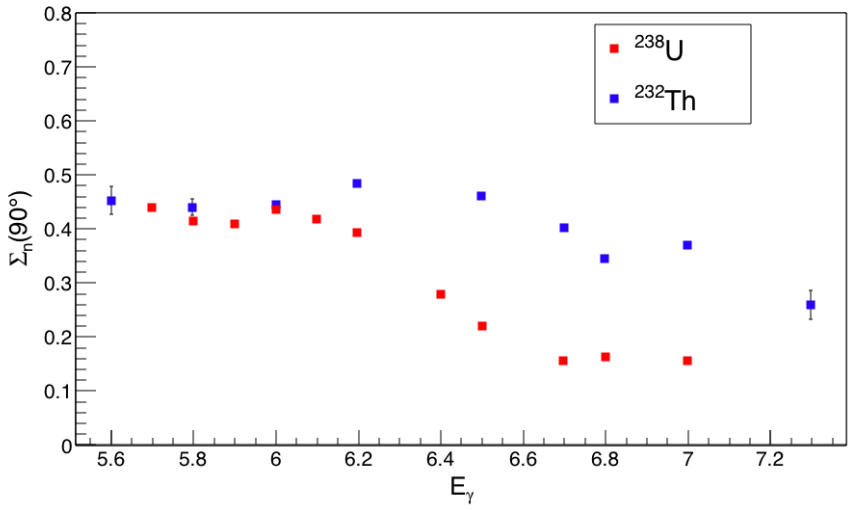

Figure 4.8: Neutron polarization asymmetries measured by Mueller *et al.*[14]. Error bars correspond to statistical uncertainties.

The large asymmetry at low E_γ is due to fission primarily proceeding through the (J^π,K) channel (1^-,0) which, as discussed in section 3.3, has a large polarization asymmetry. At higher E_γ there are contributions from the (1^-,±1) channels which have a negative asymmetry, so the combined angular distribution from all contributing channels is overall less asymmetric.

The asymmetries are shown for all detected neutrons with energies above a 1.5 MeV threshold since the pulse shape discrimination technique does not effectively separate the γ-ray background for smaller pulse heights. A majority of the fission neutron energy spectrum falls below this threshold (see Fig. 3.6), so only a fraction of the fission neutrons are measured. Given the correlation between the neutron emission angle relative to the fission fragment and its energy (see Fig. 3.7), it is expected that the neutron polarization asymmetry for all energies will be smaller as the angular distribution of the lower energy neutrons won't follow the fragment angular distribution as directly and will be more spread out.

The present work measured the photofission neutron polarization asymmetries for a range of E_γ that overlaps the previous measurement and extends to lower E_γ. In the overlap region this work probed the effect that the lower energy photofission neutrons have on the

polarization asymmetries. In the lower E_γ region, the present work allows a search for changes in the polarization asymmetries which would be associated with the turn-on of a resonant state in the fission barrier, complementing the photofission cross section measurements.

4.4 Photofission Neutron Multiplicities

There are two measurements[61][71] of the prompt photofission neutron multiplicities for ^{232}Th in the E_γ region of interest for the present work ($E_\gamma \leq 6$ MeV), and the one measurement[71] for ^{238}U which partially overlaps the E_γ region of interest ($E_\gamma \leq 6.3$ MeV). Findlay *et al.*[61] measured the ^{232}Th prompt photofission neutron multiplicities induced by bremsstrahlung γ-ray beams. Photofission neutrons were detected by an array of 56 BF_3 proportional counters suspended in oil moderator. Measurements were taken in end point energy steps of 50 keV below 6.5 MeV and 100 keV above 6.5 MeV, and an unfolding technique was employed to determine the underlying multiplicity distribution as a function of excitation energy. The ^{232}Th and ^{238}U neutron multiplicity data from Caldwell *et al.*[71] were generated from the same set of measurements performed by Caldwell and Dowdy[58] which is described in section 4.2.2.

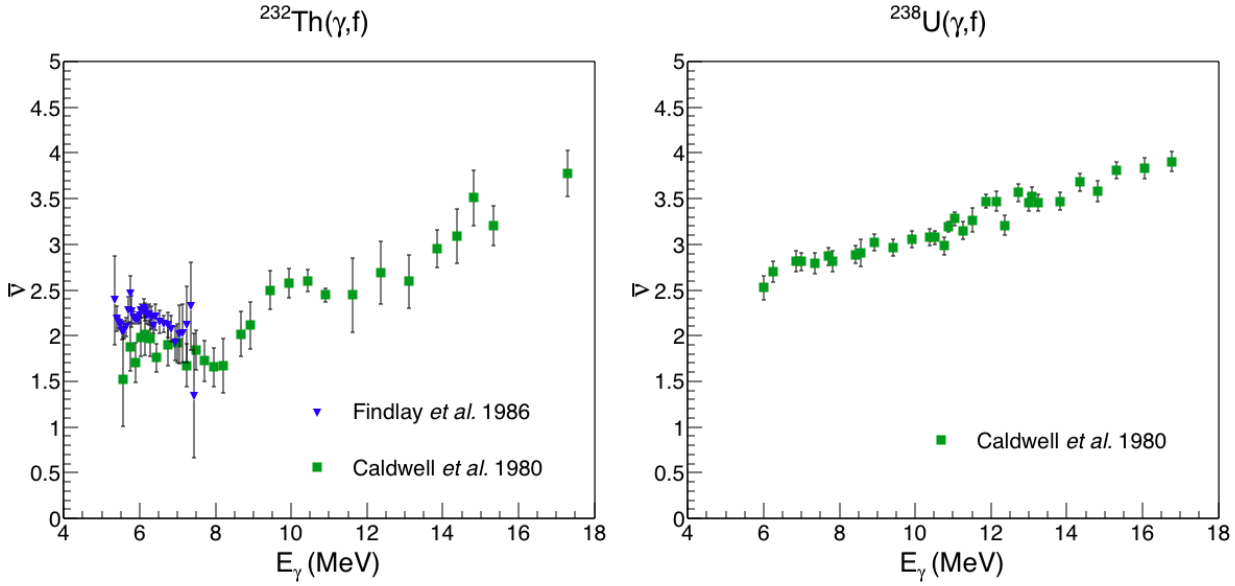

(a) ^{232}Th(γ,f) $\overline{\nu}$[61][71]. (b) ^{238}U(γ,f) $\overline{\nu}$[71].

Figure 4.9: Prompt photofission neutron multiplicities for ^{232}Th and ^{238}U.

The measured prompt neutron multiplicities, $\overline{\nu}$ are shown in Fig. 4.9. At higher E_γ the increase of $\overline{\nu}$ with energy is roughly linear, but at sub-barrier E_γ there is an apparent plateau in ^{232}Th. Additionally there is systematic disagreement between the two measurements, so

an improved measurement of $\overline{\nu}$ for ^{232}Th is necessary for constraining the photofission cross sections.

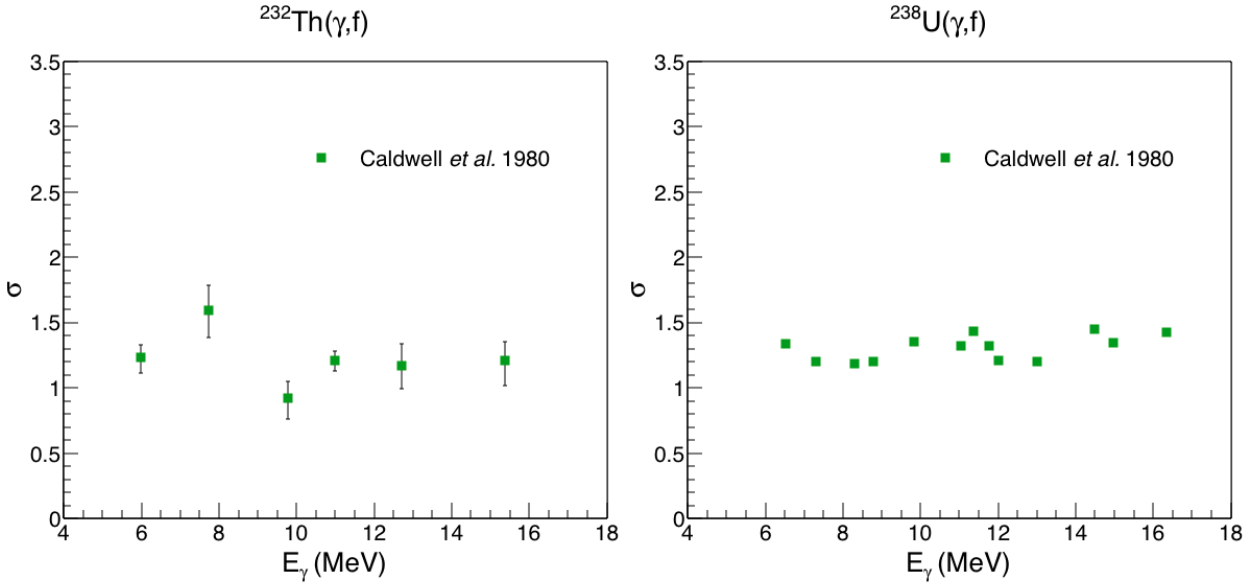

(a) ^{232}Th(γ,f) σ[71]. (b) ^{238}U(γ,f) σ[71].

Figure 4.10: Prompt photofission neutron spreads for ^{232}Th and ^{238}U.

The prompt neutron multiplicity distribution is also defined by a spread σ with the assumption that the distribution can be modeled with a Gaussian function. The data of Caldwell *et al.*[71] represents the only measurement of σ for the sub-barrier photofission of ^{232}Th and ^{238}U. In the case of both isotopes the existing data do not overlap with the E_γ region of interest for the present work.

CHAPTER 5: THE EXPERIMENT

5.1 Introduction

Measurements were performed at the High Intensity γ-ray Source (HIγS) facility[72], which produced the high-flux, quasi-monoenergetic polarized γ-ray beams necessary for this work. The γ-ray beams were incident on either a ^{232}Th or ^{238}U target, inducing photofission and emitting neutrons. Additionally a ^{nat}Pb and D_2O target were used for measuring backgrounds and characterizing the detector. The fission neutrons were detected by a high-efficiency neutron detector with multiple ^{3}He proportional counters. Signals were recorded from each proportional counter individually to preserve asymmetries about the polarization axis of the γ-ray beam. Production of the γ-ray beams will be discussed in more detail in sections 5.3 and 5.4. Sections 5.5 and 5.6 will cover the description of the neutron detector and the data acquisition system, section 5.7 will describe the targets, and a more detailed account of the experiment follows in section 5.2.

5.2 Experiment

Neutrons were detected by the INVS (described in section 5.5), which was positioned in the Upstream Target Room (UTR) of the HIγS facility. The γ-ray beam first passed through the collimator hut where it was collimated to 12 mm diameter and then passed through a thin plastic scintillator beam flux monitor (discussed in section 5.4). To limit the rate of detection of background neutrons generated outside of the detector, a $\sim$ 20 cm thick layer of 30% borated polyethylene was constructed around the INVS. The γ-ray beam then traveled into the UTR where it was incident on the target. The HPGe (described in section 5.4) was positioned downstream of the target and during normal operation was moved off

of the beam axis. A polycarbonate vacuum pipe under rough vacuum extended from the collimator hut to past the INVS detector to prevent backgrounds due to the γ-ray scattering in the air. The targets for the photofission experiment or for γ-ray beam diagnostics were mounted in the vacuum pipe in the longitudinal and axial center of the INVS detector. The full experimental configuration is shown in Fig. 5.1.

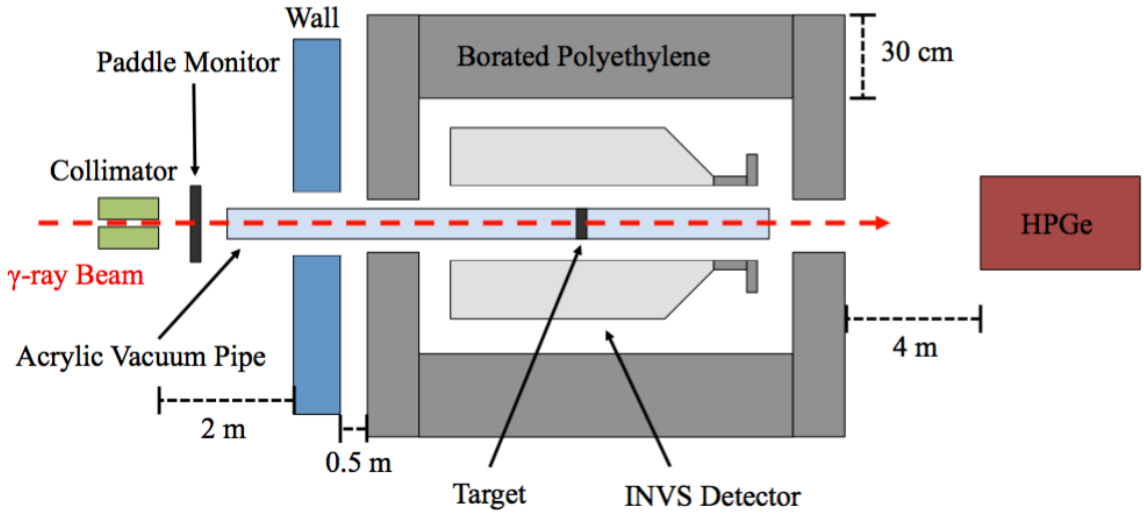

Figure 5.1: Experiment arrangement (not to scale) of detector, target and flux monitor.

5.3 HIγS γ-ray Beams

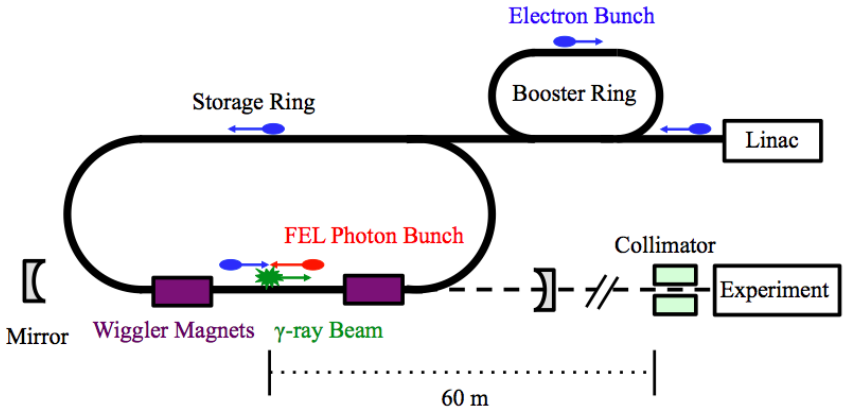

Figure 5.2: Schematic of the HIγS facility.

The HIγS facility produced γ-ray beams by a Compton scattering process in which low energy photons generated with a free electron laser (FEL) collide with counter propagating high energy electrons, boosting the photon energy into the γ-ray regime. A schematic of the free electron laser facility is shown in Fig. 5.2. Electrons were accelerated by a linac and injected into bunches in the booster ring, where the electrons were accelerated to match the energy of the storage ring, between 240 MeV and 1.2 GeV. The electrons were then injected into the storage ring in 2 bunches which traveled around the ring 180° out of phase. A series of wiggler magnets along one side of the storage ring caused the electrons to oscillate and emit photons as they traveled through. A pair of mirrors on either end of the beam line formed an optical cavity which trapped the FEL photons. After the FEL photon bunch was reflected by a mirror and traveling in the opposite direction, it encountered the second electron bunch at the collision point and inverse Compton scattering would occur. A head-on collision between a photon and electron raised the photon's energy from $1.17 - 6.53$ eV to $1 - 100$ MeV, depending on the energy of the FEL photons and the energy of the electrons in the storage ring. The scattered energetic photons, which were boosted to γ-ray energies, traveled through the mirror and on to the collimator and target area, 60 m from the collision point.

The resulting γ-ray beams were nearly mono-energetic and bright, with typical flux on target of $\sim 10^8$ γ/s. For this work γ-ray beams were produced in the range of 4.3-6.3 MeV with typical energy resolution of $\leq 3\%$. To produce the $4.3 - 6.3$ MeV γ-ray beams the accelerator was operated with 780 nm FEL photons, electron storage ring energies of $420 - 520$ MeV and a typical electron storage ring current of 90 mA. A 12 mm diameter Pb collimator was used to limit the γ-ray beam size and improve energy resolution. Additionally the γ-ray beams were 100% linearly or circularly polarized since the Compton scattering interaction preserved the polarization of the photon. The polarization of the γ-ray beam was the same as the polarization of the FEL photons, which was determined by the orientation of the wiggler magnetic fields. HIγS had wiggler magnets for both circularly and linearly polarized

light. Most of the present work was performed with linearly polarized γ-ray beams, but some data were taken with circularly polarized beams to calibrate the detectors and account for any geometry induced asymmetries.

5.4 γ-ray Beam Diagnostics

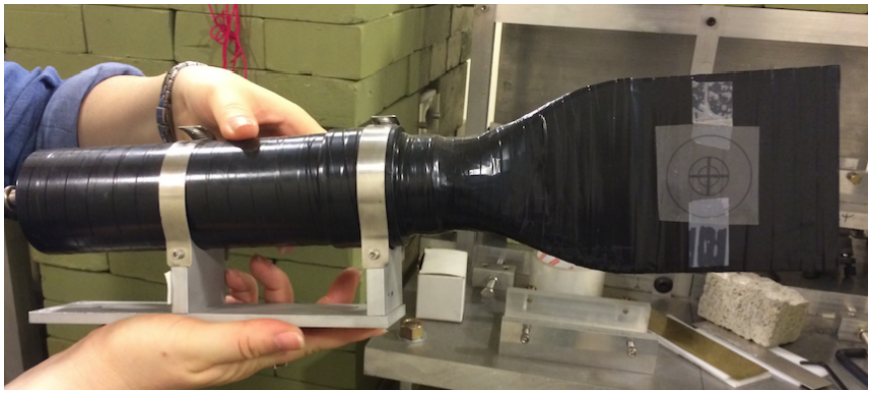

Figure 5.3: Scintillating paddle used as the γ-ray beam flux monitor

The relative flux of the γ-ray beam was monitored in real time during the experiment by placing a thin sheet of plastic scintillator upstream of the main experimental target and detector assembly. The flux monitor (Fig. 5.3) consists of a 10 cm x 10 cm x 1 mm sheet of polyvinyltoluene affixed to a photomultiplier tube (PMT) by a light guide. The PMT signal was sent through a discriminator to generate a logic pulse when the signal exceeded a threshold. The rate of the logic pulses was displayed in real time to verify that the γ-ray beam was on target and that the flux remained fairly constant. Additionally the discriminator logic pulses were recorded by a scaler in the CODA DAQ. During the data taking period the purpose of the paddle was to be a purely relative flux monitor and beam diagnostic tool, so no effort was taken to make an absolute efficiency calibration of the monitor. The absolute flux monitor was going to be a D_2O target observed by a pair of liquid scintillator neutron detectors, which would count neutrons produced through the D(γ,n) reaction. This flux monitor system had been deployed at HIγS in the past with no issues, but never for such low γ-ray beam and neutron energies. The light output response

of the BC501A scintillator is not as well known for such low neutron energies, and as a result different parameterizations of the light yield produced different pulse height spectra and therefore different neutron detection efficiencies. Among several light yield curves tested, the efficiency of the flux monitor changed by over a factor of 2. Additionally the dependence of the flux monitor efficiency on γ-ray beam energy depended strongly on the choice of light yield data. Ultimately the flux monitor based on deuteron photodisintegration was rejected in favor of instead using the scintillating paddle as the absolute flux monitor for the HIγS γ-ray beam. The calibration method is described in detail in section 6.5.

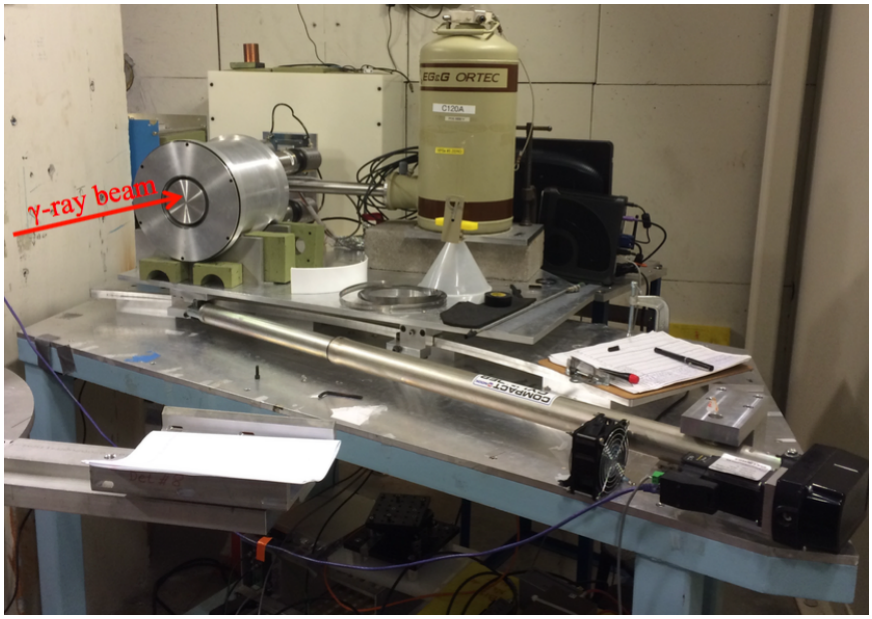

Figure 5.4: HPGe detector and moveable table platform, in the 0° position.

The energy spectrum of the γ-ray beam was measured with a 120% High Purity Germanium Detector (HPGe), pictured in Fig. 5.4. The HPGe was mounted on a motorized table which could be be set to two positions: one in which the HPGe detector was directly in the path of the γ-ray beam (the 0° position), and the other in which the HPGe detector was moved out of the beam path. During normal operation the HPGe detector was positioned out of the γ-ray beam to prevent damage to the detector. In order to measure the energy spectrum of the γ-ray beam, a series of copper attenuators was placed in the path of the beam upstream of the collimator, reducing the intensity to about 10^3 γ/s. The attenuation of

the γ-ray beam in copper changes slowly and smoothly with energy, so the energy spectrum of the γ-ray beam was unaffected by the attenuation. Once the copper attenuators were in place the HPGe detector was moved into the 0° position to measure the spectrum of the γ-ray beam.

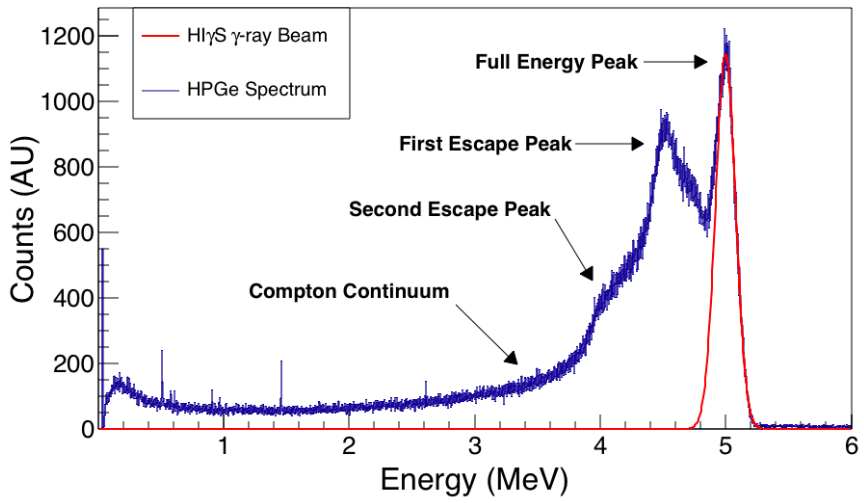

Figure 5.5: 5.0 MeV γ-ray beam spectrum obtained with the HPGe detector at 0°.

The HPGe detector signal was shaped and amplified by a spectroscopy amplifier, and the resulting signal was sent into a Canberra Multiport II multichannel analyzer (MCA). Spectra were acquired from the MCA with the GENIE 2000 software package. A typical γ-ray beam spectrum obtained with the HPGe detector is shown in Fig. 5.5. The full energy peak is populated by events where a γ-ray deposits all of its energy into the detector. The first and second escape peaks correspond to events where one or two 511 keV γ-rays leave the detector without depositing energy. The 511 keV γ-rays are produced by the annihilation of a positron generated through pair production in the detector. Consequently the first and second escape peak are located at 511 keV and 1022 keV below the full energy peak, respectively. The Compton continuum consists of events where the incident γ-ray Compton scatters off an electron within the detector and exits the detector, with only the electron depositing energy. The analysis of the HPGe spectra is detailed in section 6.2.

A γ-ray beam imaging apparatus was used to verify the alignment of the beam to the

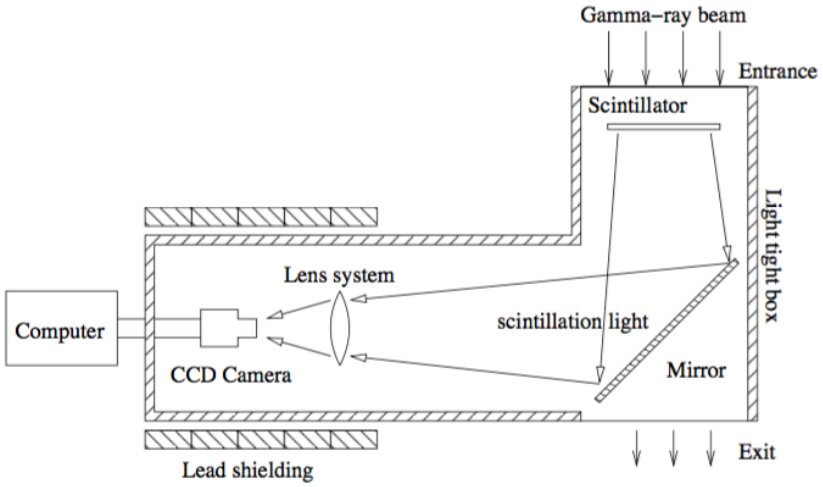

Figure 5.6: HIγS γ-ray beam imaging system[73].

collimator and targets. The γ-ray beam imager consists of a scintillating plate, a mirror and a CCD camera, arranged as in Fig. 5.6 to capture an image of the fluorescent light emitted by interactions between the γ-ray beam and the plate. Dense materials in the path of the γ-ray beam cast a shadow, and the resulting images were used to verify that the collimator and target were well aligned with the beam. The alignment of the collimator to the γ-ray beam was determined by the shape of the collimated beam on the imager as shown in Fig. 5.7. The target alignment for this work was verified by mounting a metal nut on the center of the target holder, shown in Fig. 5.8

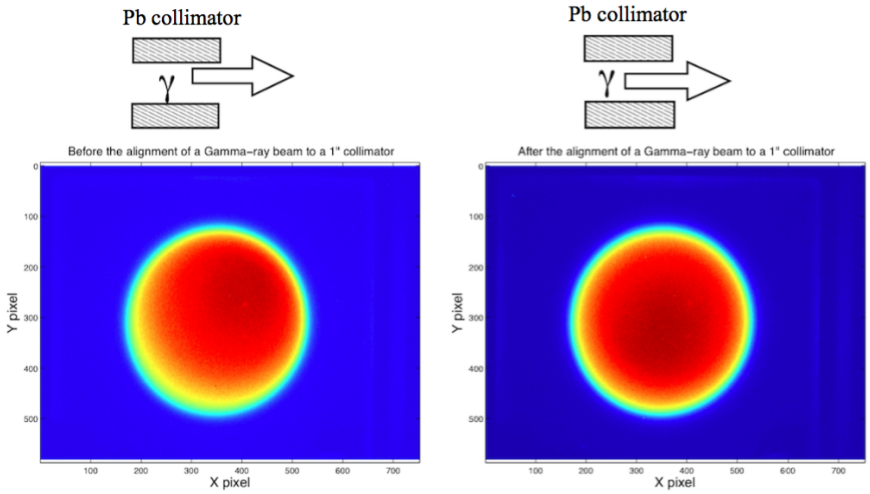

Figure 5.7: Example images taken with the γ-ray beam imager of a misaligned and aligned collimator[73].

(a) Alignment target.

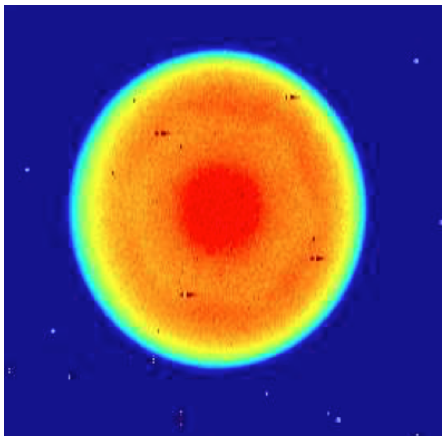

(b) Image of alignment target taken by γ-ray beam imager.

Figure 5.8: Alignment of target to γ-ray beam.

5.5 Neutron Detector

The model-IV Inventory Sample neutron detector[74] (INVS) consisted of 18 ^{3}He proportional counters embedded in a cylindrical shell of polyethylene moderator (Fig. 5.9). The proportional counters had a diameter of 2.54 cm, an active length of 39 cm and a ^{3}He gas pressure of 6 atm. The tubes were arranged in 2 concentric rings with radii 7.24 cm and 10.60 cm, with each ring containing 9 equally spaced proportional counters. The polyethylene detector body was 46.2 cm long and 30.5 cm in diameter with an 8.9 cm diameter axial cavity for placing a neutron generating target.

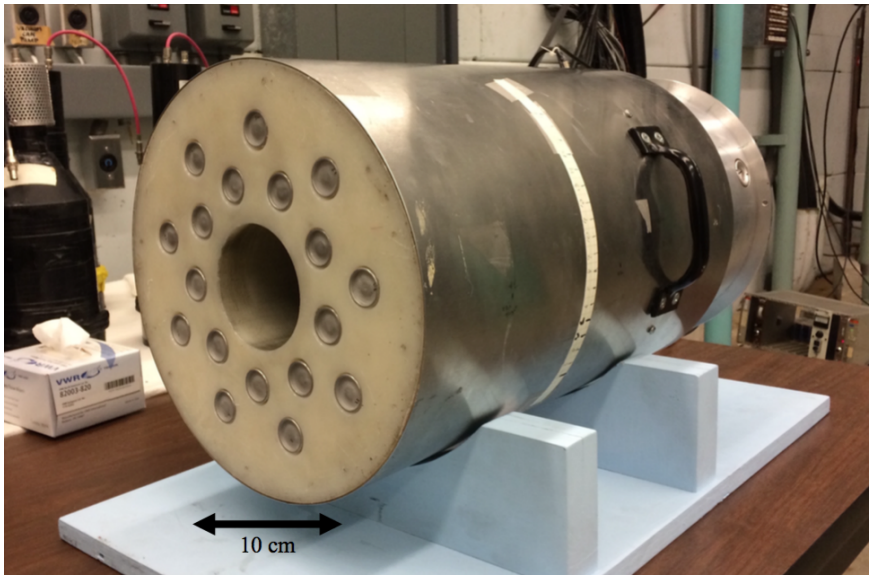

Figure 5.9: INVS detector.

Neutrons were brought into thermal equilibrium with room temperature through elastic scattering off of the ^{1}H and ^{12}C nuclei in the polyethylene, with typical neutron energies of $\sim$0.025 eV. The thermal neutrons could then be detected by capturing on the ^{3}He in the proportional counter volume. The proton and triton produced by the ^{3}He(n,p)^{3}H reaction shared an energy of 763.8 keV, depositing their energy primarily by ionizing the ^{3}He gas. The free electrons were accelerated towards an anode wire in the center of the proportional counter which was biased to +1780 V. The accelerated electrons became energetic enough to further ionize the ^{3}He gas to produce more free electrons, resulting in a Townsend avalanche

with charges collected on the central anode wire. A charge sensitive preamplifier amplified the charge avalanche signal producing a large voltage pulse.

As designed at Los Alamos National Laboratory the INVS initially had preamplifier and discriminator circuits built into the detector. The proportional counters were grouped into 3 preamplifier channels by electrically connecting the anodes of the counters: 4 and 5 tubes from the inner ring, and 9 from the outer ring. The logic signal outputs of the 2 channels that made up the inner ring were then combined so that the detector would output counts in the inner ring, the outer ring, and the total counts as TTL signals. This detector configuration had no sensitivity to the angular distribution of neutrons, in particular any asymmetries induced by a linearly-polarized γ-ray beam. Further the signal analysis electronics functioned as a black box making it impossible to determine if γ-ray interactions in the ^{3}He tubes were not registered as neutron pulses. Finally the existing signal analysis electronics were not designed to generate timestamps for each neutron detection event. Since one of the goals of this work is to measure the prompt fission neutron multiplicities, the DAQ needed to record neutron detection times so that neutrons from the same fission event could be correlated in the subsequent analysis.

The INVS was modified for the present experiment to allow for single tube readout by removing the original preamplifier and discriminator circuits and installing 18 SHV connections with direct access to each of the proportional counter anodes. An array of Cremat CR-110 charge sensitive preamplifiers[75] was mounted in a single enclosure (Fig. 5.10) with each preamplifier connected to a single proportional counter. The outputs of the preamplifiers were then sent to the data acquisition system.

5.6 Data Acquisition

Two separate data acquisition systems (DAQ) were used with the INVS: a real-time analysis system based on NIM signal processing electronics and scalers, and a digitizer-based DAQ for offline analysis. A schematic for the full DAQ is shown in Fig. 5.11.

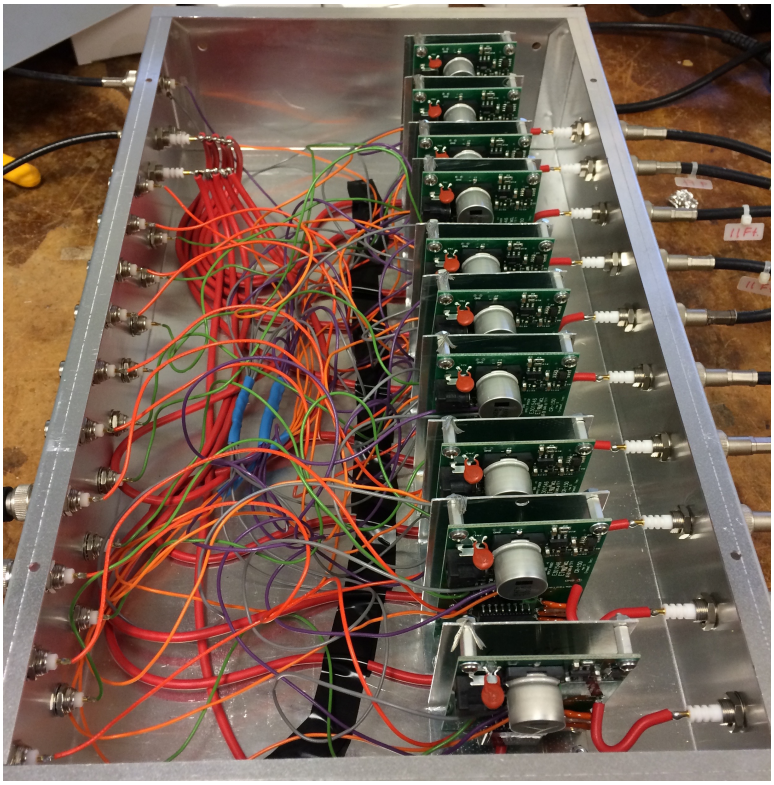

Figure 5.10: Cremat preamplifier array for the INVS detector.

In the real-time DAQ system, signals from the preamplifiers were sent through a fast timing-filter amplifier (TFA), a constant fraction discriminator (CFD) and finally to a scaler which was read out by the proprietary software CODA[76]. The CODA software name comes from CEBAF Online Data Acquisition system, where CEBAF stands for Continuous Electron Beam Accelerator Facility. The CODA scalers could be read in real time and were used as diagnostic tools during the run. The 16-channel fast amplifier used in this work, a CAEN N568B, output signals with the same polarity as the input unlike most TFAs which invert the polarity. Since the CFDs required negative amplitude signals, an inverter and fan-out module was used to flip the TFA signals.

The digitizer DAQ system utilized a CAEN V1730 16-channel digitizer with a sample rate of 500 megasamples/s (MS/s). Waveforms were read out and saved using CAEN's Wavedump application. The digitizer recorded 15 preamplifier channels, with the 16th channel reserved for a 1 Hz pulser for synchronizing digitizer time stamps and monitoring dead

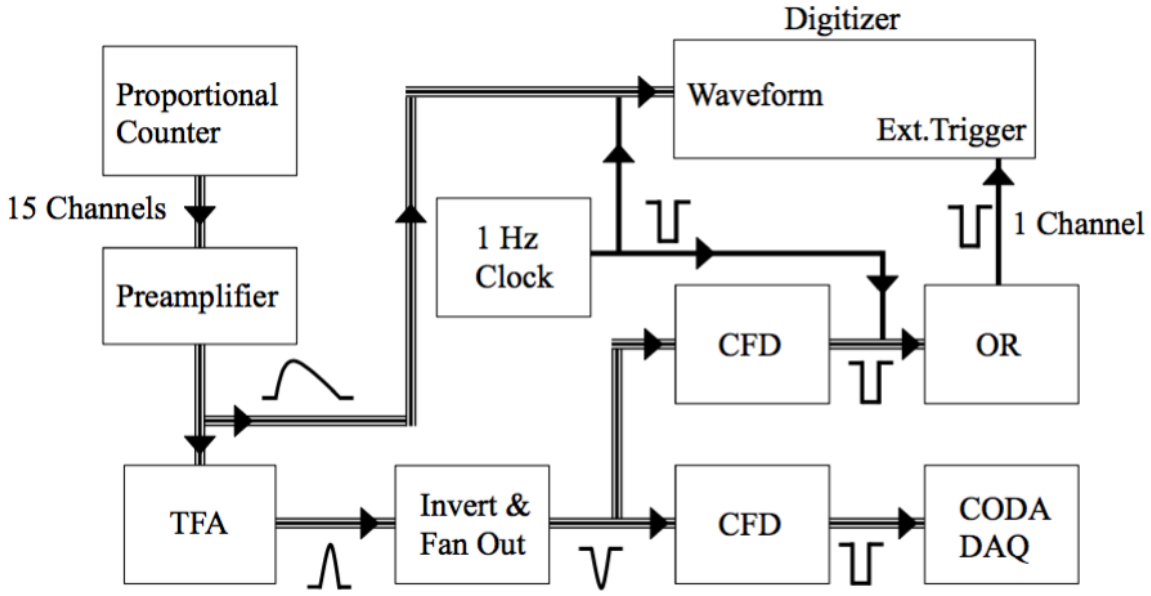

Figure 5.11: DAQ logic diagram.

time. The Wavedump software only supported triggering on a user-set threshold, which led to problems when the baseline shifted in the preamplifier output because of the long pulse decay times. To remedy this problem the digitizer was triggered by an an external trigger. The external trigger was generated by taking the outputs of the TFA in the CODA DAQ for the 15 preamplifier channels and sending them through another CFD with a lower threshold intentionally set to include both real neutron-capture events and background γ-ray Compton scatter events (see section 6.3.1 for more details).

5.7 Targets

The present experiment used two isotopes for the investigation of the fission process. The ^{238}U target was composed of 8 disks with thicknesses ranging from 0.55 mm to 0.81 mm (detailed in Table 5.1) with a total thickness of 5.06 mm and mass of 53.67 g.

The ^{232}Th target was composed of 5 identical disks of thickness 2.00 mm, diameter of 25.40 mm and mass of 59.5 g. The disks were made of natural thorium which was 99.98% ^{232}Th with only trace amounts of $^{227-231,234}$Th, so the contribution from the other isotopes of

Disk Label	Thickness (mm)	Diameter (mm)	Mass (g)
A	0.62	27.87	6.157
B	0.58	28.00	6.259
C	0.55	27.93	6.564
D	0.60	27.95	7.100
E	0.68	27.95	7.054
F	0.59	27.82	6.590
G	0.63	27.92	6.969
H	0.81	27.92	6.977

Table 5.1: List of disks which compose the ^{238}U target.

thorium can be neglected. The ^{232}Th decays via α-emission with a branching ratio of 78.2% for $E_\alpha = 4.01$ MeV[77], presenting a possible neutron background through (α,n) with target holder materials. Given the mass of the thorium target and the 1.4×10^{10} y half life of ^{232}Th an α-decay background of 240 kHz is expected. These α-particles are above the threshold for (α,n) interactions for many nuclei including ^{13}C, so a copper target holder was used because the copper isotopes present in ^{nat}Cu have (α,n) reaction thresholds above E_α[78]. The ^{238}U and ^{232}Th targets are shown in Fig. 5.12.

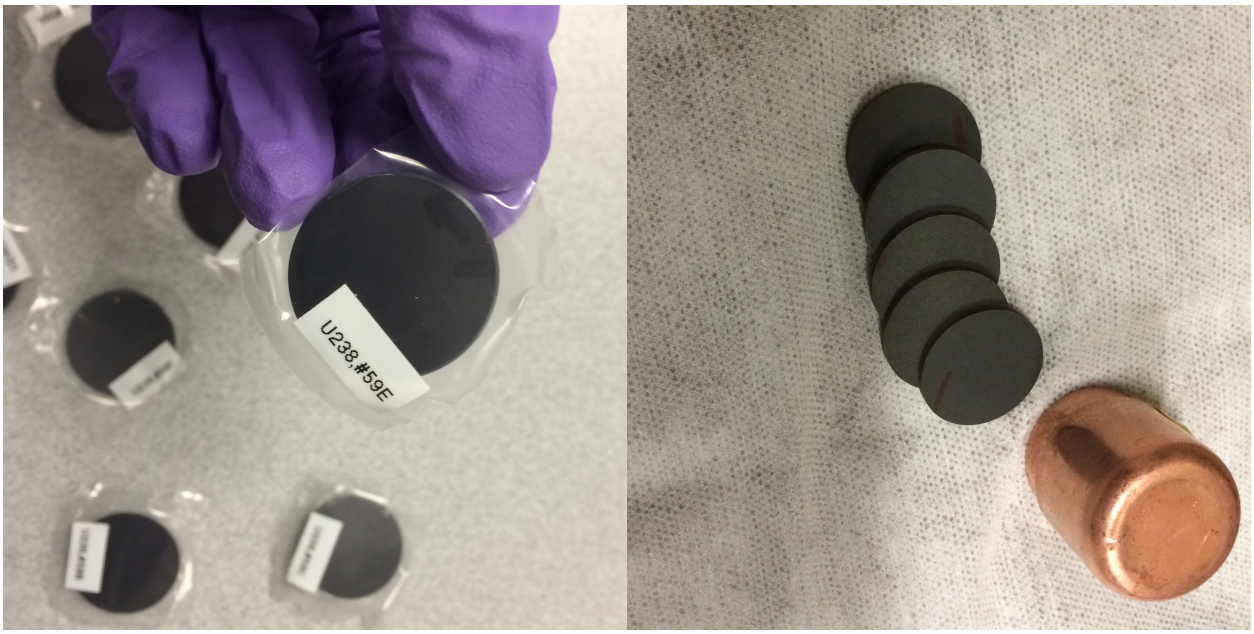

(a) One disk of the ^{238}U target. (b) ^{232}Th target and copper holder.

Figure 5.12: ^{232}Th and ^{238}U targets.

Additional targets were used for background measurements and for detector characterization. A D_2O cell with thickness 1.46 cm and diameter 3.7 cm was used to verify simulations of the detector response to neutrons generated by the D(γ,n) reaction. A ^{nat}Pb target of thickness 1.6 cm and diameter 2.54 cm was used to measure backgrounds caused by γ-rays scattering off of the target, as detailed in Section 8.3.4. The targets were mounted in a polycarbonate vacuum pipe which served as the target holder.

CHAPTER 6: DATA REDUCTION & ANALYSIS I

6.1 Introduction

The present work used two γ-ray detectors and a neutron detector, each of which requires thorough characterization. This chapter will detail the calibration efforts which were necessary for the present measurement. Section 6.2 will discuss the calibration of the HPGe detector which measured the spectrum of the γ-ray beam and section 6.5 will explain the calibration of the scintillating paddle which monitored the γ-ray beam flux. The analysis of the waveforms output by the INVS detector is discussed in sections 6.3 and 6.3.1. A GEANT4 Monte Carlo model of the INVS detector is discussed in section 6.4. The calibration of the simulated INVS neutron detection efficiency and sensitivity to neutron angular distributions will also be covered.

6.2 HPGe Detector

The energy spectrum of the HPGe detector was calibrated using several γ-ray emitting sources and a naturally occurring room backgrounds. The sources and γ-ray energies are

Isotope	E_γ (keV)
^{22}Na	511
	1274.53
^{60}Co	1173.237
	1332.501
^{133}Ba	356.017
	383.851
^{137}Cs	1175.63
^{208}Tl	2614.533

Table 6.1: Isotopes and their emitted γ-rays which were used to calibrate the HPGe energy spectrum.

listed in Table 6.1. Fig. 6.1 shows the linear fit which was used to determine the conversion between MCA channel number and energy.

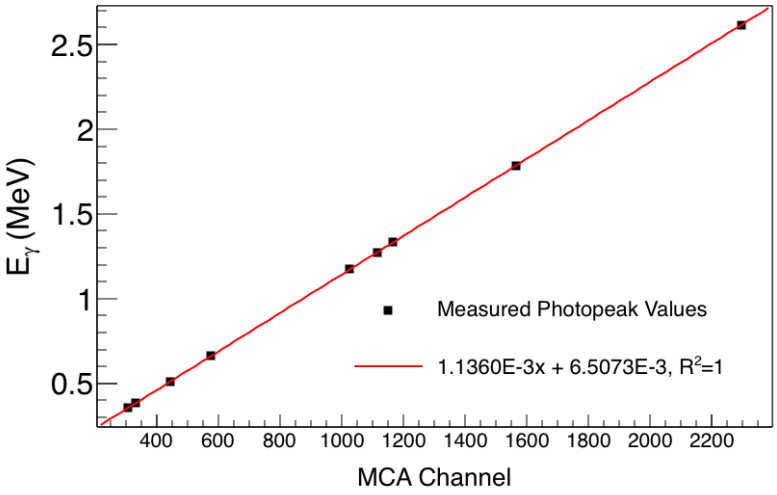

Figure 6.1: Calibration fit for HPGe pulse height spectrum.

Once the HPGe energy spectrum was calibrated the measured HIγS γ-ray beam energy profile could be fit. The γ-ray beams produced by HIγS have a Gaussian energy profile, with the beam spectrum completely described by a mean and a spread. Compton scattering and escape of pair-produced 511 keV γ-rays introduced structure into the spectrum that the HPGe observes; however they were not present in the primary γ-ray beam. To prevent these detector induced effects from impacting the fitting of the γ-ray beam spectrum, only the high energy side of the spectrum was fit. Fig. 6.2 shows the HPGe spectrum and fit to the beam profile. Over all the beam energy measurements made in this work, with $4.3 \leq E_\gamma \leq 6.3$, the spread averaged $\sigma = 1.42\%$ and the mean deviated from the nominal value by an average of 6.5 keV, or about 0.1% .

6.3 Digital Waveforms from the INVS

The digitized waveforms of the preamplifier outputs of the ^{3}He proportional counters were analyzed after the conclusion of the experiment. The digitizer acquisition window was

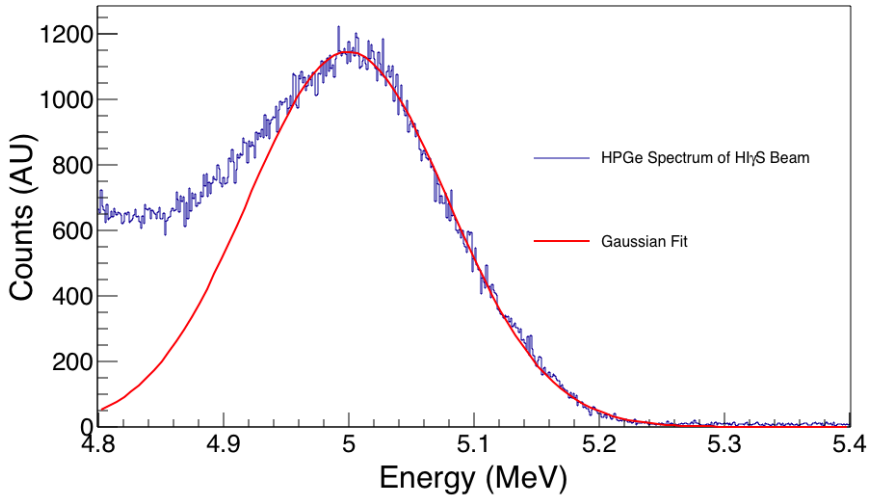

Figure 6.2: Gaussian fit to HIγS γ-ray beam spectrum.

4.1 μs long, consisting of 2050 samples at 500 MS/s. The digitizer recorded a trace for all 16 channels every time it received a trigger signal. In addition each waveform had an associated timestamp based on a 125 MHz internal clock in the digitizer. The timestamp was stored as an unsigned long integer with a maximum value of $2^{32} - 1$, or $\sim$34 s. When the maximum value that the timestamp integer could store was exceeded the highest bit of the timestamp would flip and the number would roll over to 2^{31}, so the 1 Hz pulser channel was used to correct for the time shifts to produce continually increasing timestamps.

Additionally the 1 Hz pulser served as a live time monitor. Under normal operation there should be no dead time in the digitizer as the full wave form is recorded, so even if multiple events overlapped in the same trigger window they would all be recorded. However due to the high sampling rate and relatively long acquisition window the digitizer generated a large amount of data for each trigger, which meant at high enough trigger rates the digitizer would produce data faster than it could be transferred and stored on the DAQ computer. The maximum trigger rate that the digitizer could handle without data loss was approximately 1000 Hz, so caution was taken to keep the trigger rate below about 500 Hz by limiting the γ-ray beam flux with attenuators at higher energies where the photofission cross sections were greater. As long as the trigger rate was kept reasonable, the 1 Hz clock consistently

indicated no dead time.

6.3.1 Pulse Shape Discrimination

Neutron detection events were identified in the digitized preamplifier waveforms through the use of a pulse shape discrimination (PSD) technique developed for ^{3}He proportional counters[79]. The PSD was needed since in addition to ^{3}He(n,p)^{3}H neutron detections in which the proton and triton deposit energy in the proportional counter (PC) volume through ionization, γ-ray beam produced Compton scatter electrons which could also deposit energy in the PC gas through ionization. ^{3}He-based PCs are known for being relatively insensitive to γ-ray backgrounds, but HIγS produces high enough γ-ray fluxes to create a detectable background. In particular for this experiment the $\sim 10^8$ γ/s HIγS beam scattered off of a thick ^{238}U or ^{232}Th target resulting in approximately 20% of the incident beam undergoing Compton scattering, with a large fraction of it directed into the INVS.

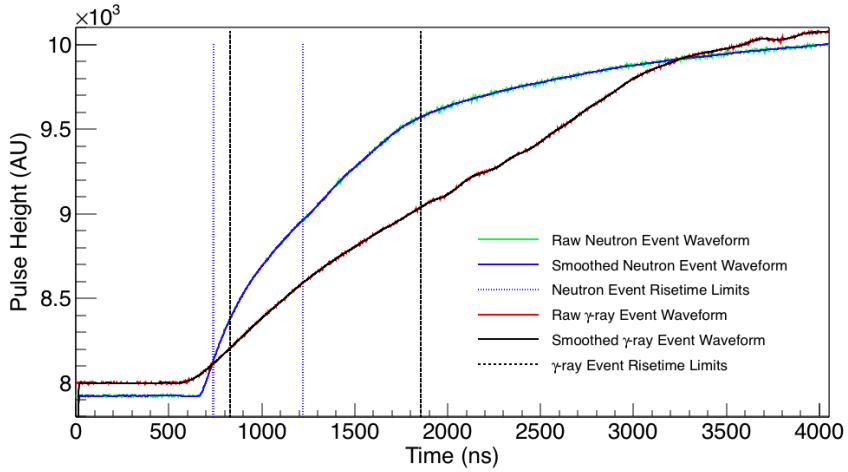

Figure 6.3: Digitized preamplifier waveforms for neutron detection event and γ-ray event with similar amplitudes. The risetime limits for each waveform mark when the pulse rises 10% and 50% above the baseline.

The difference in stopping power in the PC gas between electrons and heavy ions could be exploited to differentiate between neutron and γ-ray events. The length of the ionization track in the PC corresponds to the risetime of the pulse. In the present experiment the saved

digitizer waveforms were analyzed to extract the risetime, pulse height, timestamp and tube number from every pulse. The analysis routine assumed one pulse per digitizer channel for each trigger, so a majority of the extracted pulses were just baseline noise. A Gaussian smoothing routine was applied to the waveforms to reduce high-frequency noise. Then the pulse height and risetime were extracted, with the pulse height defined as the maximum value in the waveform minus the baseline, and the risetime defined as the difference in times between the pulse reaching 10% and 50% of the pulse height above the baseline. Fig. 6.3 shows the smoothing and risetime and pulse height extraction process for a typical neutron capture pulse and a Compton-scattered electron pulse. After rising during the first 2 μs the pulse amplitude changes very slowly as it approaches the peak value, so the full rising edge of the waveform was not recorded in the interest of decreasing the amount of necessary data collected per digitizer trigger.

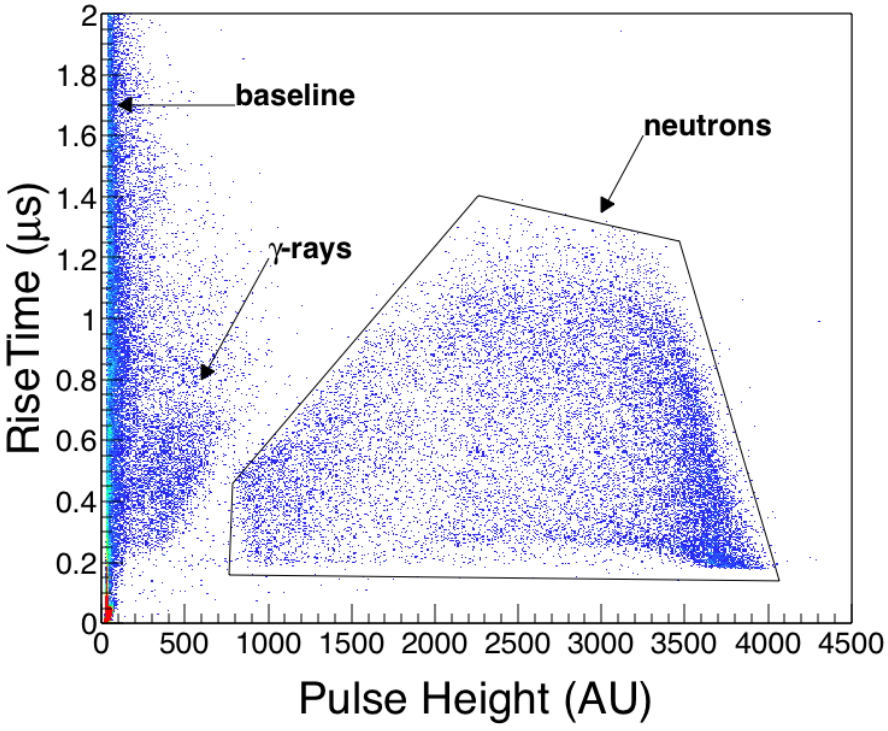

Figure 6.4: PSD plot for a γ-ray beam incident on a ^{232}Th target.

A PSD plot for one of the counters in the INVS when a γ-ray beam was incident on a

^{232}Th target is shown in Fig. 6.4. There are 3 distinct regions in the PSD plot corresponding to different types of events. The neutron event region has a well defined correlation between risetime and pulse height, with the pulses being produced by either a proton, a triton or a combination of the two. From momentum conservation the ^{3}He(n,p)^{3}H reaction emits a 573 keV proton and a 191 keV triton. These reaction products could either deposit all of their energy in the PC gas through ionization, or they could hit the aluminum walls of the gas volume and deposit some or all of their energy to produce "wall effects"[80]. The summed effects of the ionization caused by the heavy ions led to PC pulses with a unique but well defined PSD distribution. The second PSD region seen in Fig. 6.4 is the γ-ray Compton scatter event area. Electrons have a lower stopping power than heavy ions so they deposited less energy over a longer track length, resulting in longer risetimes. Thus Compton scatter events with large enough pulse heights to be misidentified as a neutron capture event would have long track lengths and therefore longer pulse risetimes, and will occupy a different region in PSD space. The third distinct PSD region which lies along the vertical axis is simply baseline noise when another channel triggers the digitzer.

The PSD cut region clearly separates the neutron events from the γ-ray background while preserving a majority of the neutron counts. If only pulse height spectra were recorded then rejecting the γ-ray background would require setting a pulse height threshold which would also reject a certain fraction of neutron events.

As a verification of the PSD properties of each type of pulse two data sets were compared: one in which a γ-ray beam was incident on a D_2O target to produce neutrons through the D(γ,n) reaction, and one in which a γ-ray beam was incident on a ^{nat}Pb target to scatter the beam into the detector and produce primarily γ-ray Compton scatter events. Fig. 6.5 shows the resulting PSD plots with the neutron event and γ-ray event regions more prominent in the D_2O and ^{nat}Pb target data sets respectively.

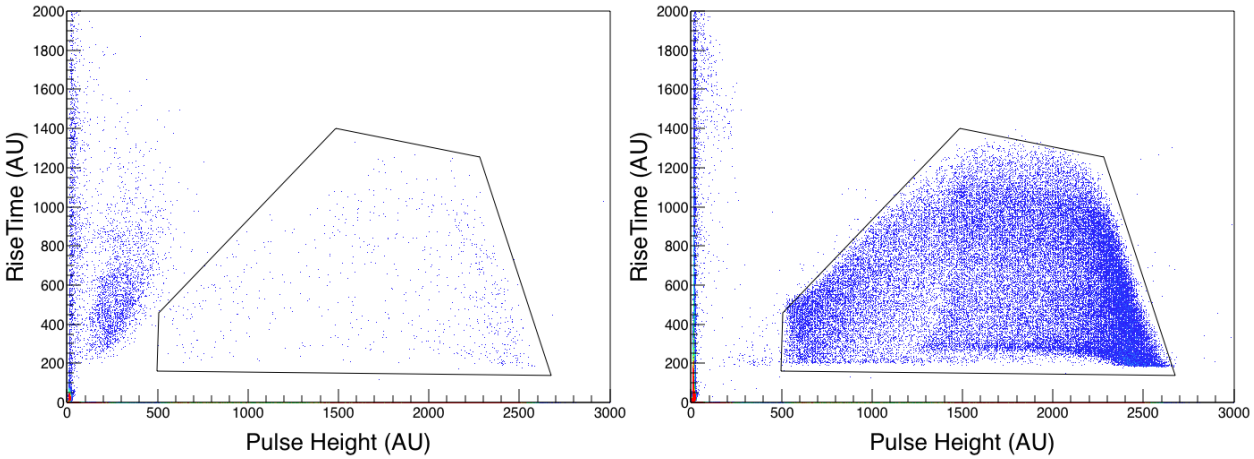

(a) PSD plot obtained with ^{nat}Pb target. (b) PSD plot obtained with D_2O target.

Figure 6.5: PSD plots for events generated by the (γ,γ') and (γ,n) reactions.

6.4 GEANT4 Model of the INVS

6.4.1 Introduction

The interpretation of the measured neutron yields strongly depends on understanding interactions between neutrons and the experimental hardware. Neutrons detected in the present work can interact with the actinide target in which they are produced, the target holder and vacuum pipe, the polyethylene moderator of the INVS detector, the ^{3}He gas volume of the PC tubes and the thick layer of borated polyethylene shielding surrounding the INVS detector. All of these interactions must be accounted for to understand the INVS neutron detection efficiency and the detector's response to asymmetries in the neutron angular distribution. This section discusses the development and characterization of a Monte Carlo simulation of the INVS detector.

6.4.2 GEANT4

The INVS detector was simulated using GEANT4 (version 4.10.01.p02), a C++ based toolkit for modeling the interactions of particles in matter[81]. By defining a detector and target geometry and a particle generator, one can compute the passage of particles through

the experimental setup in an event-by-event manner. This Monte Carlo approach models the INVS neutron detection efficiency in addition to accounting for the effects of interactions within the target material. The GEANT4 libraries contain a variety of models for computing physical processes, such as scattering and energy deposition, so it is up to the user to choose a list of relevant physical processes and preferred models for those processes. All simulations in this work used the predefined physics list "FTFP_BERT_HP" which models hadronic interactions with the Fritiof string model[82] for energies above 4 GeV and the Bertini Cascade model[83] for energies below 5 GeV. The γ-ray interactions and charged particle-induced ionization are modeled with the standard GEANT4 electromagnetic process physics code, "G4EmStandardPhysics." Most relevant to these simulations is the choice of the high precision model NeutronHP[84] for calculating neutron propagation through matter at energies below 20 MeV. NeutronHP uses extensive experimental datasets and is the most accurate way of modeling neutron interactions at energies relevant for this work.

The full INVS geometry was built into the GEANT4 simulation, including not only the detector but also any other materials present, such as the target, target holder, and shielding around the detector. A variety of simulations were used for this work, but the logic was the same for all. An event begins when a neutron is generated in the target material with some momentum and energy, propagates through the simulated geometry, and interacts with materials primarily through scattering. A fully thermalized neutron that enters the ^{3}He volume can be captured on a ^{3}He to produce a proton and triton. The simulation treats the ^{3}He gas region as the active detector, recording all interactions that occur within an event and storing them as hits. Once all particles have left the simulation world volume or are stopped the event ends and the hits are analyzed. The presence of a unique triton in one of the sensitive detector regions is considered a neutron detection, and that detection is saved to a data file by recording the PC tube number and detection time. This logic allows for multiple neutrons to be detected within a single event, as each neutron detection will create a unique triton within the simulation. Fig. 6.6 shows a simulated neutron detection

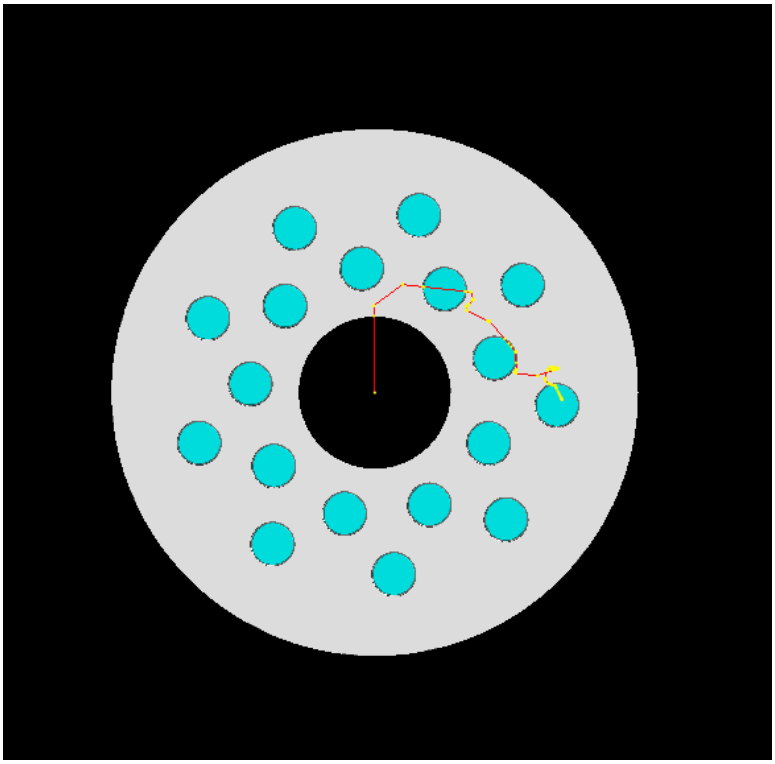

Figure 6.6: Visualization of simulated INVS with neutron detection event. The neutron's path is marked by the red line, originating in the center of the detector and scattering in the polyethylene moderator until it thermalizes and is detected by one of the PC tubes.

event.

6.4.3 Detector Efficiency Calibration

The GEANT4 simulation of the INVS does not account for potential sources of inefficiency like imperfect charge collection by the PCs, loss of ^{3}He gas pressure within the PCs and detection threshold settings. Thus it is expected that the simulated efficiency will need to be scaled by an overall scaling factor which is determined by measuring the efficiency with a particular neutron source and comparing the result with the simulation. A calibration measurement was attempted during the experiment by placing a D_2O target in the center of the detector with the HIγS beam's producing neutrons through D(γ,n), with the γ-ray beam flux measured with a flux monitor consisting of a second D_2O target observed by a pair of BC501A liquid scintillator neutron detectors. However the pulse height distributions

recorded by the flux monitor detectors could not be reproduced through simulation. Section 6.5 discusses the problems encountered with this flux monitor scheme. Without a direct measurement of the γ-ray beam flux, the D(γ,n) data could not be used to calibrate the absolute INVS detector efficiency. Instead, data from measurements performed in a previous detector characterization effort were used to calibrate the GEANT4 simulation of the INVS.

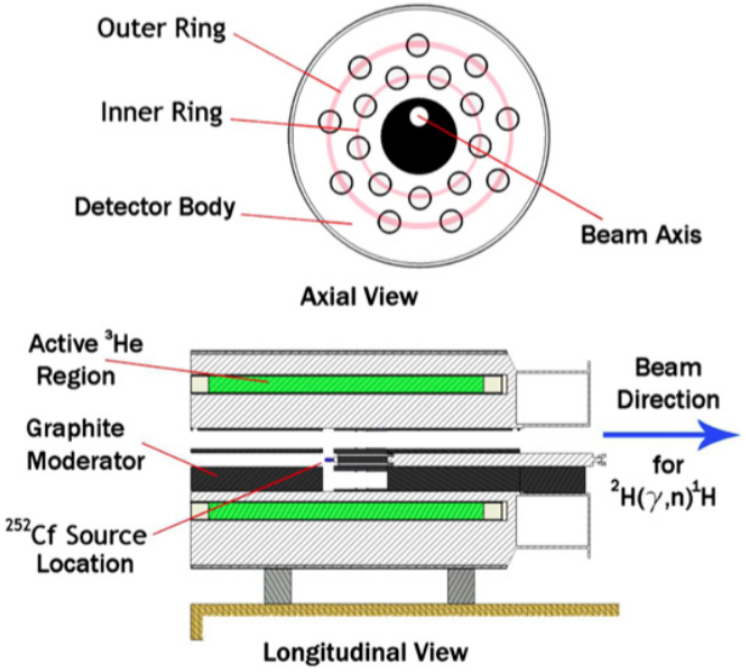

Figure 6.7: Detector and target geometry for D(γ,n) calibration measurement[85].

Arnold *et al.*[85] measured the efficiency of the INVS using nearly mono-energetic neutrons from the D(γ,n) reaction. The experimental geometry is shown in Fig. 6.7. A 7.62 cm long D_2O target was placed in a graphite moderator, at the longitudinal center of the INVS but offset from the axial center by 2.9 cm. Circularly-polarized γ-ray beams produced by the HIγS facility were directed at the D_2O target to produce neutrons. The γ-ray beams were collimated to a diameter of 1.2 cm and ranged in energy from 2.48 to 4.10 MeV, with a typical energy resolution of 1-3% FWHM. Statistical uncertainties were limited to 1% and the systematic uncertainty was $< 3\%$, with the largest contributions coming from the D(γ,n) reaction cross section (1%) and target thickness (0.5%).

The GEANT4 simulation was modified to incorporate the detector and target geometry

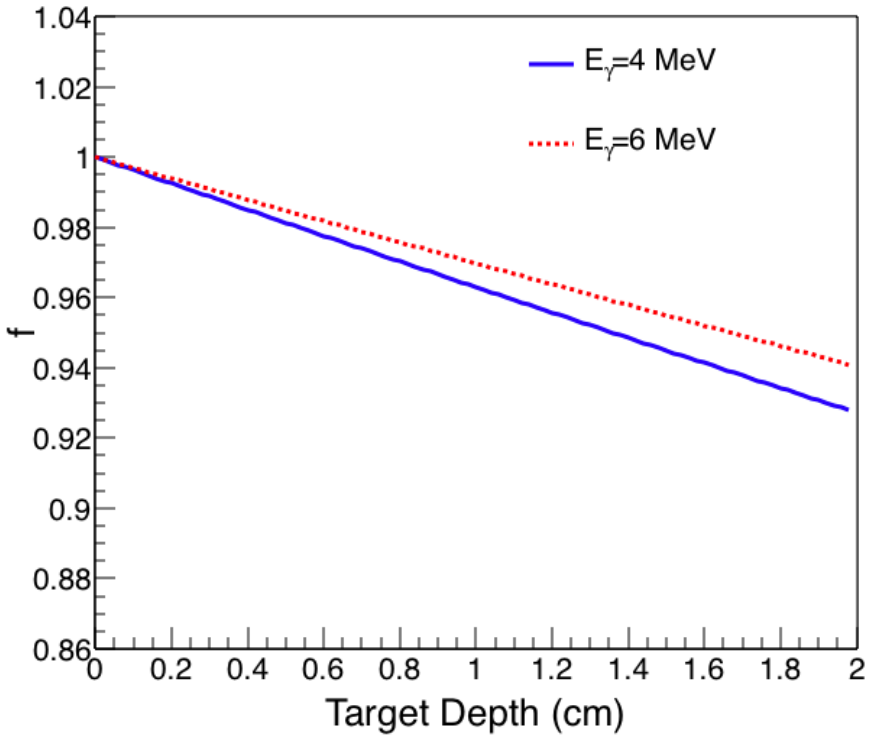

Figure 6.8: γ-ray beam interaction weighting function which accounts for the attenuation of the beam within a thick D_2O target. The function is shown for E_γ=4 MeV and E_γ=6 MeV.

of the D(γ,n) calibration measurements. Neutrons were produced in the simulation using a specially written neutron generator designed for reproducing similar measurements at HIγS. In the simulation the user specifies a γ-ray beam mean energy and FWHM. For each neutron generation event, the simulation samples a Gaussian probability distribution with the specified mean and spread to choose the energy of the γ-ray which will produce a neutron through the D(γ,n) reaction. A location for generating the neutron is chosen from within the cylindrical volume representing the intersection of the γ-ray beam and the D_2O target. The radial position is chosen at random; however the position along the length of the target is weighted to account for the attenuation of the γ-ray beam within the thick target. The weighting function f, shown in Fig. 6.8, is proportional to $e^{-x\mu\rho}$, where x is the depth within the target, ρ is the density of heavy water (1.11 g) and μ is the energy-dependent mass attenuation coefficient for heavy water. The mass attenuation coefficient is determined

by interpolating between data sets provided by NIST[86].

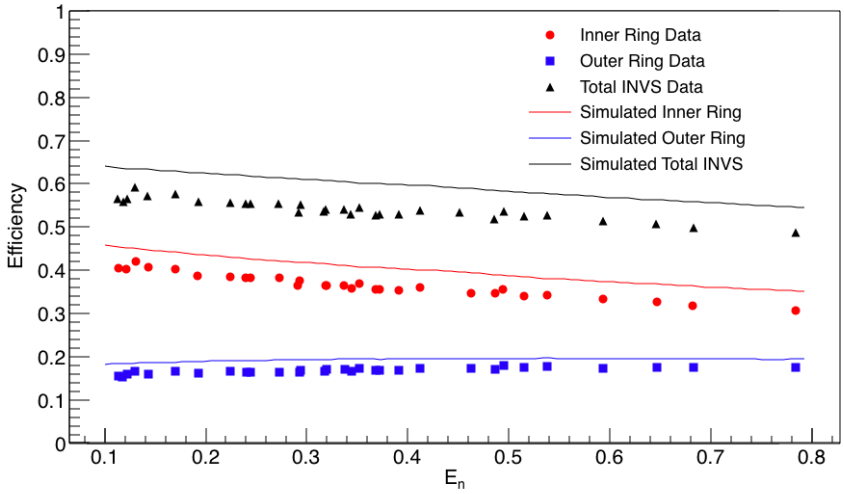

Figure 6.9: Comparison of D(γ,n) reaction efficiency measurements and GEANT4 simulation.

Once a location is selected the emission angle of the neutron is determined by sampling the angular distribution in the center of momentum (COM) frame, described in further detail in appendix A. The resulting efficiencies determined by the GEANT4 simulation are shown in comparison with the D(γ,n) reaction measurements in Fig. 6.9. As expected, the simulation predicts a higher efficiency than what is observed as the simulation does not account for inefficiencies from charge recombination in the ^{3}He PCs or threshold settings in the electronics. There is very good agreement between the efficiency curves and the data apart from an overall scaling factor of 0.892 ± 0.003 (stat) ± 0.03 (sys) for the inner ring and 0.876 ± 0.004 (stat) ± 0.03 (sys) for the outer ring. The scaled simulation efficiency curves are plotted against the data in Fig. 6.10. The ratios of the scaled simulation to the experimentally measured efficiencies are shown in Fig. 6.11, with the largest deviations being a few percent.

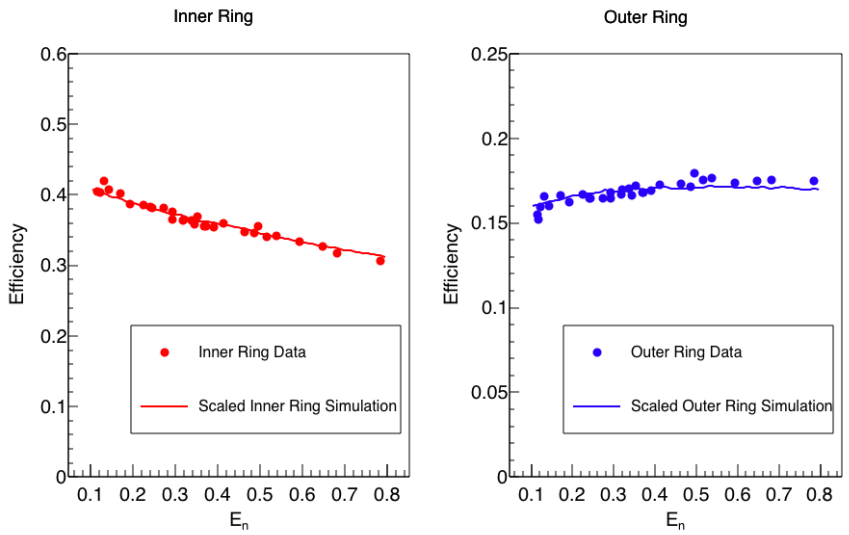

Figure 6.10: Scaled simulated efficiency compared to measured efficiency.

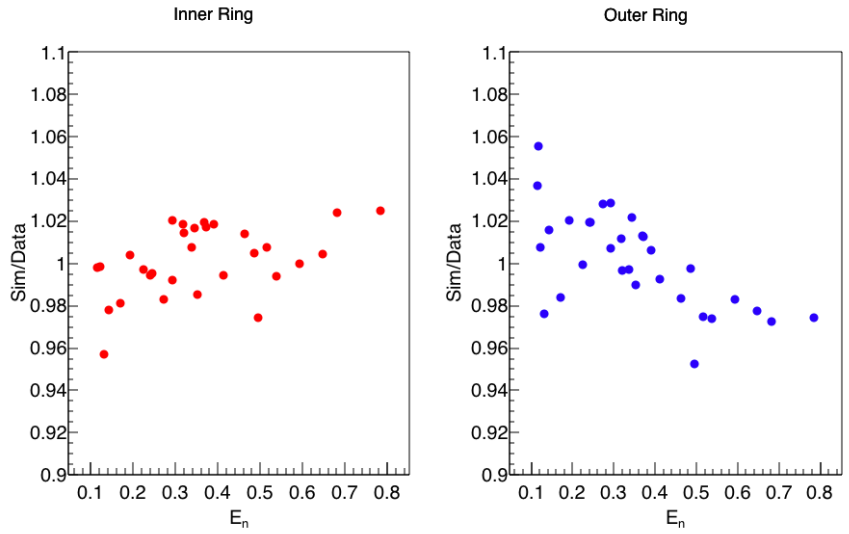

Figure 6.11: Residual plot of the D(γ,n) reaction efficiency measurements and simulations.

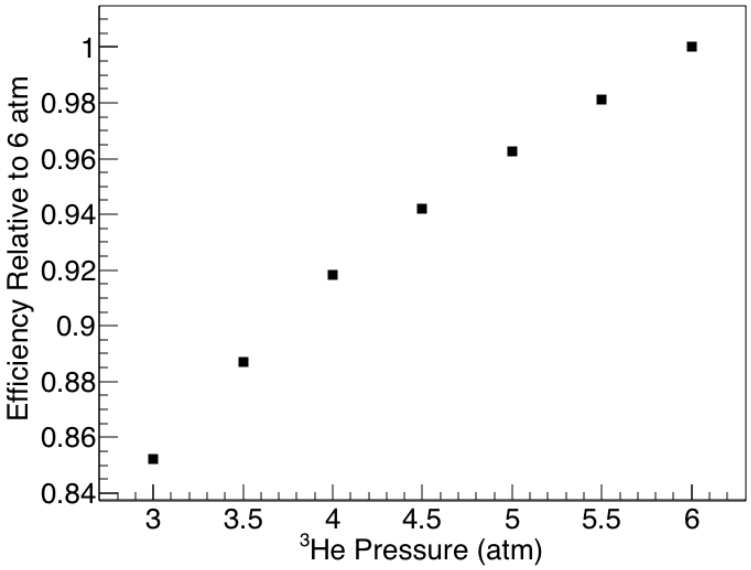

Figure 6.12: Relative efficiency of INVS as a function of ^{3}He gas pressure.

As mentioned earlier in this section, the difference in efficiency between simulation predictions and measurements are potentially the result of several factors. A loss of ^{3}He pressure, or simply having less pressure than the nominally quoted value, would lower the INVS efficiency as shown in Fig. 6.12. Additionally, inefficiencies in charge collection in the PCs because of electron recombination are not considered. The simulation assumes a 100% detection efficiency for each ^{3}He(n,p)^{3}H reaction, while the results are consistent with simulations which instead sum the total energy deposition by the recoiling proton and triton within the PC gas volume. A typical spectrum from one such simulation is plotted in Fig. 6.13. The full energy peak at 764 keV is populated by events in which both the proton and triton deposit their full energy in the ^{3}He gas volume. A sharp ledge at 573 keV occurs as a result of events in which the triton exits the PC without depositing any of its 191 keV. The second ledge at 191 keV occurs as a consequence of momentum conservation. If a ^{3}He(n,p)^{3}H reaction event occurs near the wall of the PC and the triton exits without depositing any energy the proton must be traveling in the opposite direction into the gas volume. A SRIM (Stopping Range of Ions in Matter)[87] calculation gives a predicted range of a 191 keV proton in 6

atm ^{3}He of 2.4 mm, meaning that it will deposit all of its energy within the 25.4 mm diameter gas volume. Thus the minimum expected pulse height for a neutron capture event is equivalent to 191 keV. For comparison a 573 keV triton has a SRIM projected range of 7.5 mm, meaning it too would deposit its full energy if directed into the gas volume from the edge.

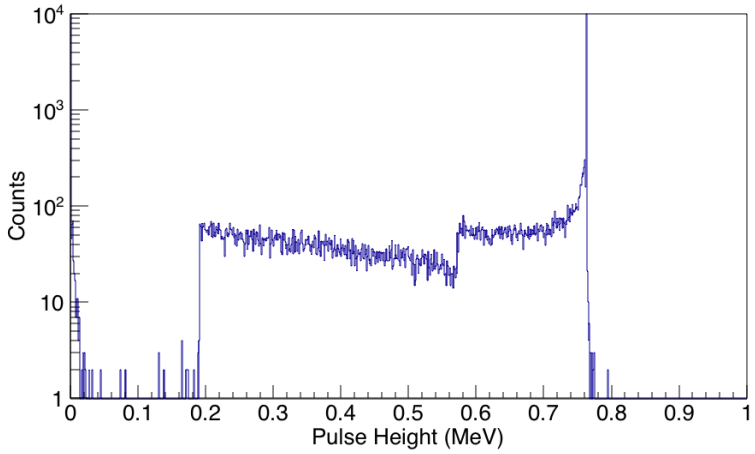

Figure 6.13: Simulated ^{3}He PC pulse height spectrum.

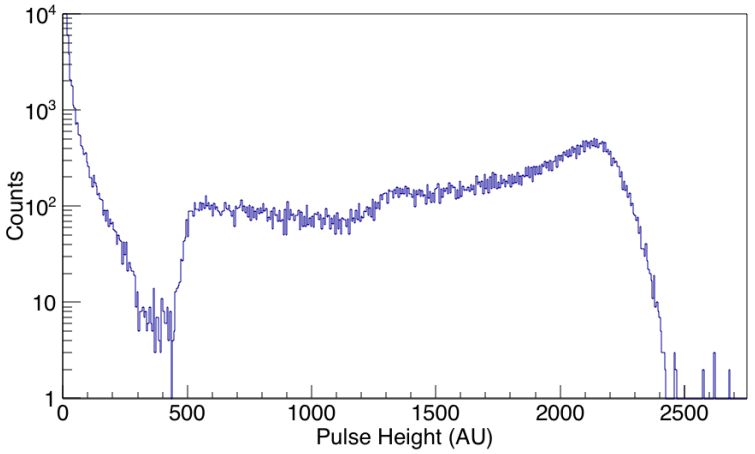

Figure 6.14: Measured ^{3}He PC pulse height spectrum.

A typical spectrum observed in the INVS ^{3}He counter is shown in Fig. 6.14. The spectrum is not directly comparable to the simulation because the short duration of the digitizer window did not capture the full pulse height, spreading and shifting the full energy

peak down in energy. The wall effect features are clearly apparent and the simulated ^{3}He PC spectrum agrees qualitatively with the measured spectrum.

At this point the GEANT4 simulation of the INVS has been calibrated to model the detector as it existed when the D(γ,n) reaction data were taken. However, that measurement was made before the INVS was upgraded to record the preamplifier signal from each channel separately into a digitizer. Thus an additional step must be taken to calibrate the change in efficiency between the original and modified detector readout electronic systems. The change in efficiency only impacts the constant scaling factor between the simulated INVS detector efficiency and the experimental efficiency. Since this scaling factor is not energy dependent it does not matter which neutron energy spectrum used for the relative calibration before and after the detector upgrade.

Prior to the upgrade a relative efficiency measurement was taken with an AmBe neutron source. This measurement was then reproduced with the upgraded DAQ to determine the change in efficiency. The same AmBe source was used in both measurements to reduce sources of systematic error in the calibration. In particular the shape of the neutron energy spectrum produced by an AmBe source strongly depends on the internal geometry of the Am and Be mixture. The α-particles emitted by ^{241}Am lose energy through straggling, with the resulting α-particle spectrum depending on the thickness of the Am grains. The ^{12}C nucleus formed by α-capture on ^{9}Be has several available energy states where the branching to each state depends on the energy of the α-particle. The decay scheme for each excited ^{12}C state results in a different neutron energy spectrum, and thus each AmBe source has a unique neutron spectrum which depends on the size of the Am grains[88]. The INVS detector efficiency is very sensitive to the incident neutron energy and consequently AmBe sources can only be used for relative efficiency measurements.

Using the same 19.1 mCi AmBe source, the relative INVS efficiency after the upgrade was measured to be 0.866 ± 0.001 for the inner ring and 0.885 ± 0.001 for the outer ring. The GEANT4 simulation is then scaled by 0.790 ± 0.003 (stat) ± 0.02 (sys) for the inner

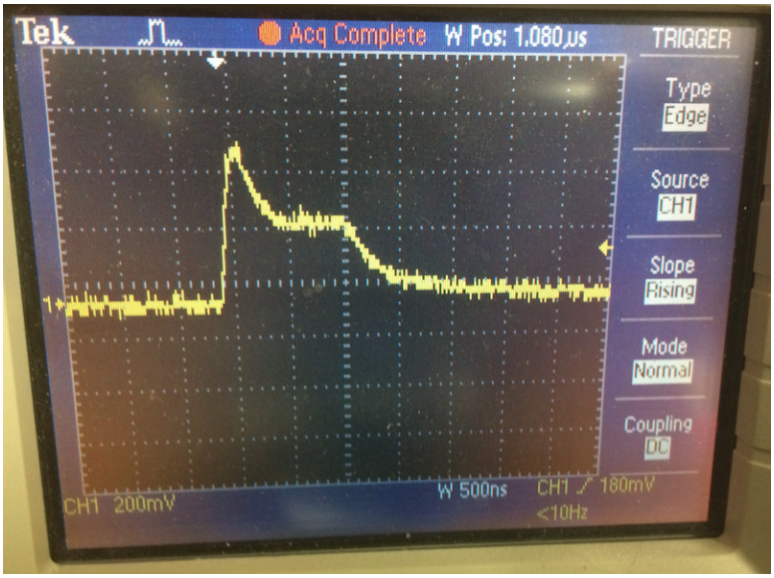

Figure 6.15: FOUT signal from CAEN N568B for neutron detection event.

ring and 0.775 ± 0.004 (stat) ± 0.02 (sys) for the outer ring. The further loss in efficiency is likely caused by the signal quality of the fast amplifier. A fast, differentiated, amplified signal was obtained from the 'FOUT' output of a 16 channel CAEN N568B and then sent through a constant fraction discriminator (CFD) to generate the data-taking trigger signal. This particular module was chosen because there was no other way to gather enough fast amplifier channels. The N568B FOUT signal has a 100 ns differentiation time constant, which is much too fast for the ~ 5 μs risetime of the preamplifier pulses. The poor match between the fast amplifier time constant and the preamplifier risetimes leads to a messy fast amplifier signal in which a single waveform can have more structure than a single peak, as shown in Fig. 6.15. This results in having a single large pulse in the preamplifier occasionally generate a fast amplifier signal with multiple peaks where no individual peak exceeds the CFD threshold. Simultaneous observations of the CFD logic signal and the preamplifier signal with an oscilloscope verified that roughly 10% of valid neutron event pulses were not generating a trigger. While any loss in detector efficiency is not ideal, because the ^{3}He PC spectrum does not change with neutron energy, the loss of efficiency will be a constant multiplicative factor that impacts the INVS efficiency equally at all energies.

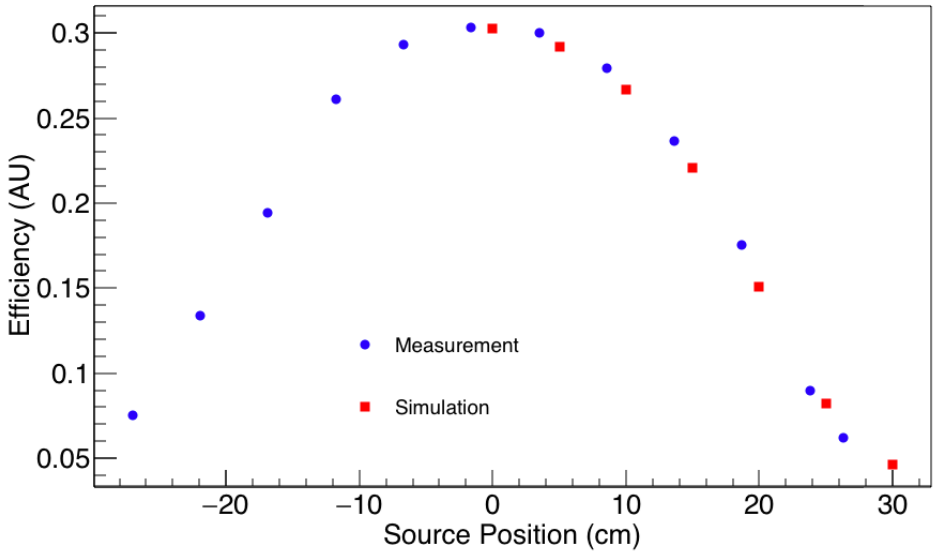

Figure 6.16: Relative INVS efficiency as a function of neutron axial source position. The source activity is not precisely known so the measured efficiency is only a relative measurement. The simulated INVS efficiency has been scaled by 1.07 to best match the measured relative efficiency.

To further validate the GEANT4 model of the INVS, the relative detector efficiency was measured for different axial source positions and compared with simulation. The measurements were made with the AmBe neutron source, and the simulation assumed an isotropic point source with a typical AmBe neutron spectrum. The results are plotted in Fig. 6.16. The simulated efficiency is scaled by an arbitrary overall constant of 1.07 to match the measured relative efficiency, a consequence of the fact that the AmBe neutron spectrum for this particular source is not precisely known and thus the absolute detector efficiency can not be simulated. The calibrated INVS detector efficiency with all 18 PCs is shown in Fig. 6.17 as a function of the neutron energy and angle θ relative to the γ-ray beam axis.

6.4.4 Neutron Asymmetry Calibration

Calibration data were taken to account for the different relative efficiencies of each PC. A beam of circularly polarized 5.5 MeV γ-rays was incident on the ^{232}Th target and neutron counts were recorded for each PC. The relative efficiency in each tube was determined by

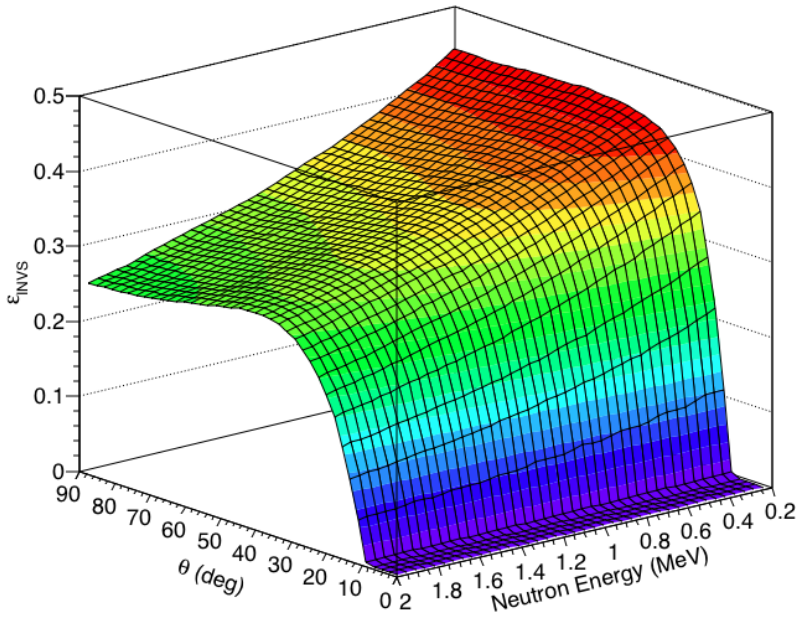

Figure 6.17: Calibrated INVS neutron detection efficiency for all 18 ^{3}He PCs, as a function of neutron energy and angle relative to the beam axis.

normalizing to the average counts per tube in the inner or outer ring. The results are plotted in Fig. 6.18. The sinusoidal pattern in the inner ring of PCs (1-8) is consistent with a small misalignment of the INVS relative to the γ-ray beam and target. As detailed in section 5.7 the target, target holder and γ-ray beam were aligned to precision better than 1 mm by the beam imaging system. However, the detector was positioned independently with a precision of a few mm. Fig. 6.19 shows the results of introducing a 5 mm offset in the simulation, with the magnitude of the induced efficiency asymmetry in good agreement with the data. Once the different tube efficiencies are accounted for the small target offset has no effect on the detector efficiency so all analysis has been done with a centered target.

6.4.5 Model Validation

In order to validate the GEANT4 model of the INVS detector, the detector response to neutrons from the D(γ,n) reaction with a linearly-polarized, 4.3 MeV γ-ray beam was simulated and compared with experimental data. The neutrons were generated in the simulation

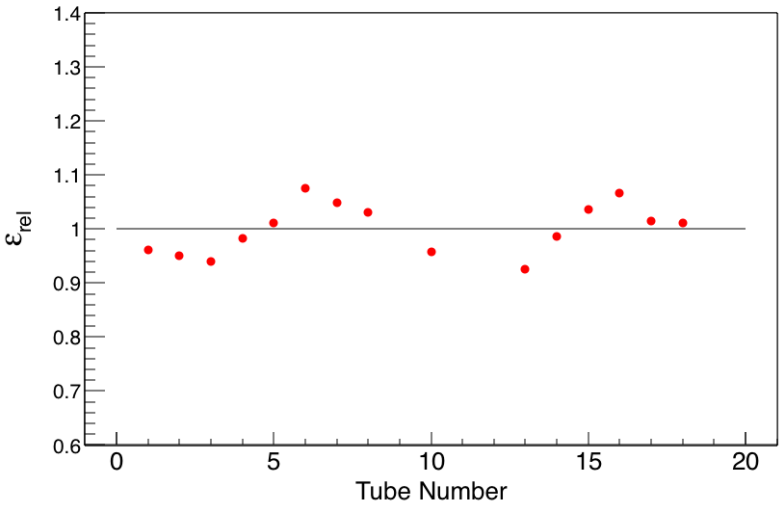

Figure 6.18: Relative efficiencies of each PC, normalized to the average counts per tube in the inner or outer ring. Statistical uncertainties are smaller than the marker size.

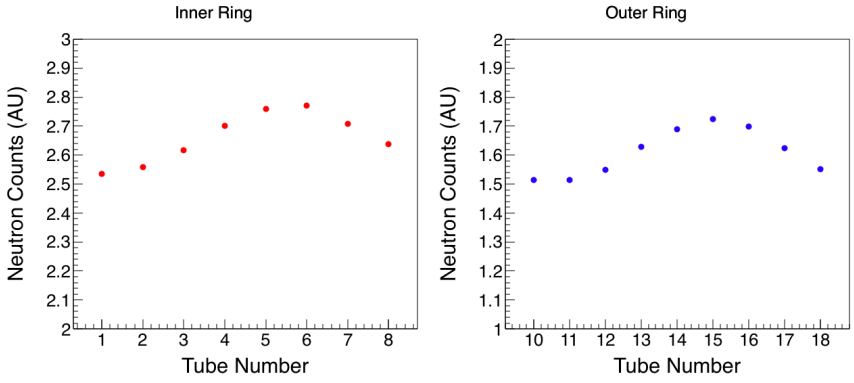

Figure 6.19: Simulated response of INVS to a 5 mm source offset.

using the same method as described in Section 6.4.3, but with a modified neutron angular distribution which took into account the effects of the polarized γ-ray beam:

$$\sigma(\theta,\phi) = \frac{\lambda^2}{96\pi^2}\left[|S|^2 + \frac{27}{2}|P|^2\sin^2\theta(1+\cos 2\phi)\right]. \tag{6.4.1}$$

Equation 6.4.1 follows the formalism of Schreiber *et al.*[89], in which θ is the angle of neutron emission relative to the γ-ray beam axis, ϕ is the angle relative to the polarization axis of the beam, λ is the wavelength of the γ-ray, and $|S|^2$ and $|P|^2$ are the M1 (s wave) and E1 (p wave) strengths respectively. The energy dependent E1 and M1 strengths for this work

come from theoretical calculations by Tornow *et al.*[90].

The first validation parameter is the ring ratio, R, defined as the average counts per tube in the inner ring divided by the average counts per tube in the outer ring, where the simulation only includes the tubes used in the measurement. The simulated R of 1.46 ± 0.05 (sys) agrees with the experimental value, 1.444 ± 0.005 (stat). The systematic uncertainty in the simulation comes from the uncertainties in the scaling factors for the inner and outer ring efficiencies. Enough events were included in the simulation to keep the statistical uncertainties over an order of magnitude below that of the systematics.

The well-defined asymmetry in the ϕ angular distribution can be used to validate the response of the simulated INVS detector to asymmetric neutron distributions. A distribution of the form $a(1 + b\cos 2\phi)$ was fit to the inner and outer detector rings in the simulation and measurement, where b is the asymmetry value. However, while the GEANT4 simulation reproduced the relative efficiencies of the detector rings, it significantly under-predicted the detector asymmetries. The measurement yielded an asymmetry of 0.132 ± 0.002 for the inner ring and 0.252 ± 0.003 for the outer ring, while the simulated asymmetries were 0.118 ± 0.001 and 0.223 ± 0.002 for the inner and outer ring, respectively. Increasing the density of the polyethylene moderator of the INVS in the GEANT4 simulation has the effect of increasing the detector asymmetry for both rings, as shown in Fig. 6.20. The probability of a neutron scattering on the H and C in the polyethylene is proportional to both the density of the material and the neutron scattering cross sections of the H and C nuclei, so increasing the density of the polyethylene in the simulation is equivalent to increasing the scattering cross section. Ultimately a polyethylene density of 1.05 g/cm^3 was necessary to reproduce the detected neutron asymmetries in the inner and outer ring of the INVS detector, with the simulated inner ring asymmetry being 0.132 ± 0.001 and the outer ring being 0.248 ± 0.002. The simulation results are plotted alongside the measured data in Fig. 6.21

Given the fact that the asymmetry simulation requires unrealistically dense polyethylene, approximately 10% greater than the standard value of 0.940 g/cm^3 used in the INVS

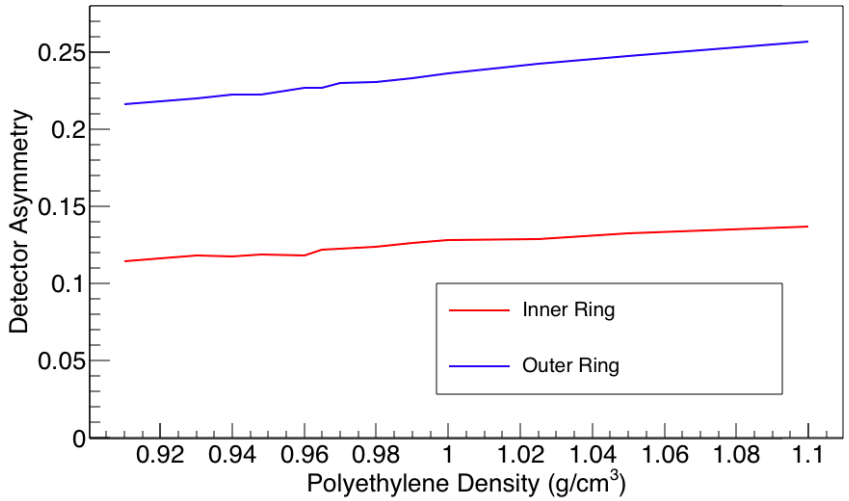

Figure 6.20: Simulated detector asymmetry for D(γ,n) reaction neutrons generated with a 4.3 MeV linearly-polarized γ-ray beam, as a function of polyethylene density.

efficiency characterization simulations, two distinct GEANT4 simulations of the INVS detector were used in this work. The first is the main simulation which models the overall efficiency and the ring ratio using the standard polyethylene density of 0.940 g/cm^3; the second models the detected neutron asymmetries using the higher polyethylene density of 1.05 g/cm^3. Since the neutron asymmetry measurements are all purely relative, the INVS asymmetry simulation does not need to have a calibrated efficiency. The simulation results are fit with the same $a(1 + b\cos 2\phi)$ function as the data, and the values of the asymmetry parameter b are compared. This process is discussed in more detail in section 8.4.1.

6.5 γ-ray Beam Flux Monitor Calibration

As discussed in section 5.4 the γ-ray beam flux was monitored with a thin, plastic scintillator paddle. Incident γ-rays can interact with the scintillator by either Compton scattering electrons or by pair-producing an electron and positron. Because the scintillator is so thin, the electrons and positrons will behave approximately as 'minimum ionizing' particles, depositing the same amount of energy into the paddle regardless of their energy[91].

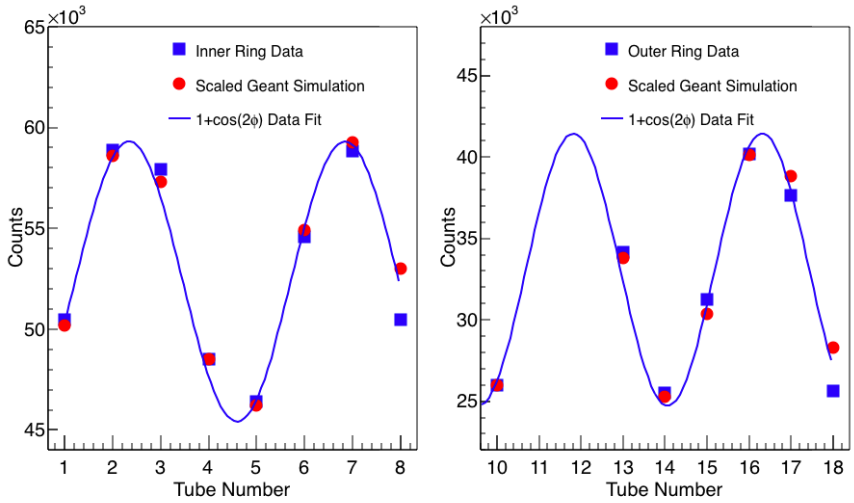

Figure 6.21: Comparison between simulated and measured neutron yields for the D(γ,n) reaction at E_γ=4.3 MeV. The simulated yields are scaled to fit the experimental data with independent scaling factors for the inner and outer rings. The largest deviations between simulation and experiment for a single tube are 5%.

As a result the paddle spectrum does not change significantly with the energy of the incident γ-ray beam, and any energy dependence in the paddle efficiency reflects the Compton scattering and pair production cross sections. To account for these effects the paddle was modeled with a GEANT4 simulation. Fig. 6.22 shows normalized pulse height spectra for incident 5 MeV and 6 MeV γ-ray beams, with both spectra being equivalent because of the minimum ionizing nature of the thin scintillator. The efficiency of the paddle as a function of threshold energy is shown in Fig. 6.23. It is clear from Fig. 6.23 that the choice of threshold setting will have a large impact on the efficiency of the flux monitor.

Knowing the efficiency of the paddle flux monitor for a particular γ-ray beam energy allows the threshold to be determined. In the absence of a dedicated calibration measurement, the best available measurement of the γ-ray beam flux comes from the detection of photofission neutrons from ^{238}U. The most precise measurement of the ^{238}U(γ,f) cross section at γ-ray energies of relevance is the one by Csige *et al.*[13]. This data set is particularly well suited for use in calibration because the measurements were made using HIγS beams with

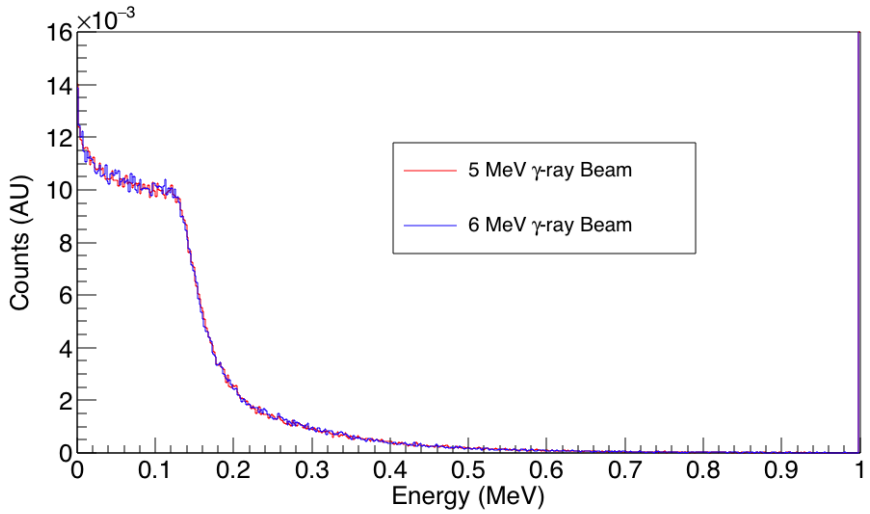

Figure 6.22: Simulated paddle spectra for incident 5 MeV and 6 MeVγ-ray beams. The plateau corresponds to the minimum ionizing energy deposited by an electron or positron.

similar energy resolution, so the observed cross sections which are the result of the integration of the γ-ray beam spectrum over the ^{238}U(γ,f) cross section are directly comparable with the current work.

Data taken at E_γ=5.6 MeV were used to calibrate the flux monitor, because at this energy the ^{238}U(γ,f) cross section is large enough to be reliably measured, there is a plateau in the cross section so there is not a strong dependence on beam energy profile, and the beam energy is well below the ^{238}U(γ,n) threshold that contaminates the present work at higher energies. Additionally, the ^{238}U(γ,f) cross section is large enough that background rates are not significant for either measurement. In order to convert the observed neutron production cross section into a fission cross section, it needs to be divided by the mean fission neutron multiplicity, $\bar{\nu}$. The $\bar{\nu}$ for ^{238}U(γ,f) was one of the fission observables measured in the present work and determined to be $\bar{\nu} = 2.46$ (more details may be found in section 9.3). With this value of $\bar{\nu}$, the paddle efficiency at $E_\gamma = 5.6$ MeV was measured to be 3.07×10^{-4}, which corresponds to a paddle threshold of 0.227 ± 0.004 MeV. Fig. 6.24 shows the paddle efficiency as a function of γ-ray energy using this calibrated threshold setting.

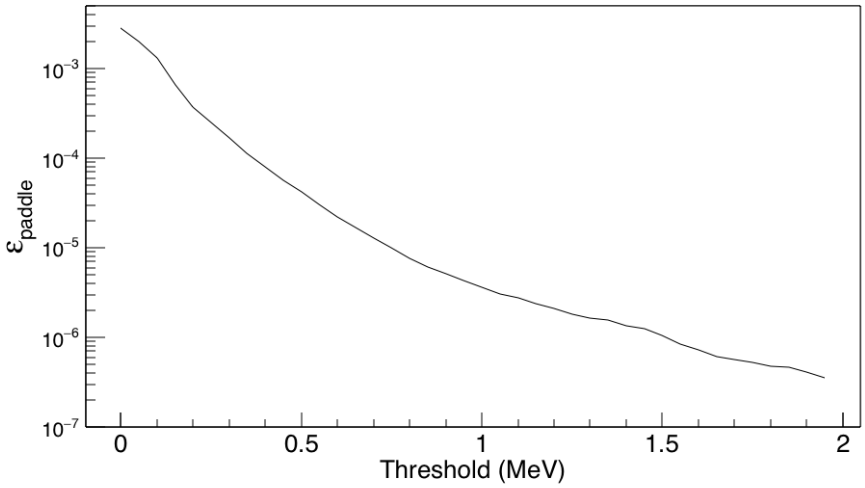

Figure 6.23: Simulated paddle efficiency for a range of threshold settings.

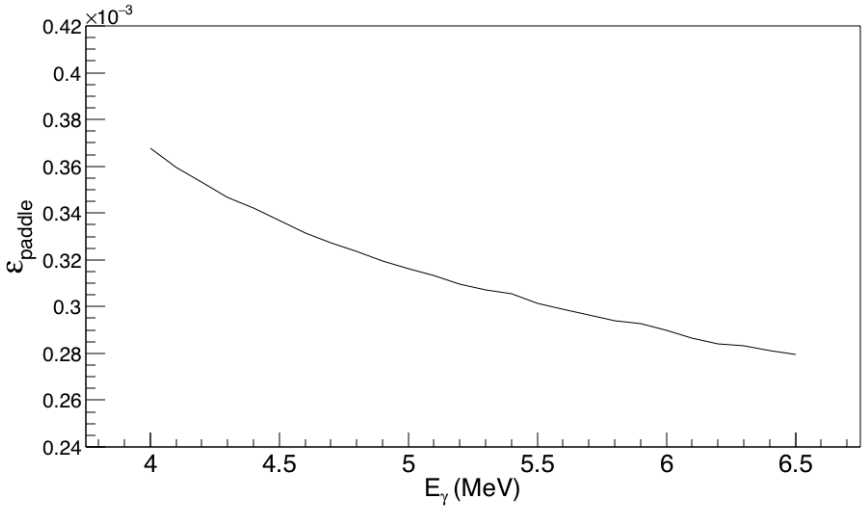

Figure 6.24: Simulated paddle efficiency as a function of energy using the calibrated threshold of 0.227 MeV.

CHAPTER 7: MODELING PHOTOFISSION NEUTRONS

7.1 Introduction

As one of the primary motivations for this work is to provide data on photofission observables, it should come as no surprise that there are not many accurate models of neutrons emitted during fission. Although most of the underlying physics of the fission process is well understood qualitatively, an accurate quantitative model of fission does not exist, as discussed in section 1.1. Consequently the ability to calculate fission observables like neutron multiplicities and energy spectra is limited. Traditional fission calculations like the Madland-Nix model[92] predict averaged quantities, like the average prompt neutron multiplicity or the average excitation energy. This approach yields no information about correlations between properties like neutron emission angle, neutron energy, multiplicity, etc, which the present work tried to address.

7.2 FREYA

A new Monte Carlo-based technique for modeling fission observables has recently been created which uses a combination of experimental data and physics models. FREYA, the Fission Reaction Event Yield Algorithm, is an event-by-event fission model currently being developed at LLNL[93]. By calculating neutron emission for specific instances of fragment masses and excitation energies, FREYA inherently provides correlations between various observables, including the neutron energy and angle of emission relative to the direction of the fission fragment. Fission neutrons generated by FREYA can then be used in the GEANT4 simulations of the experiment to model accurately the effects of correlated neutrons arising from single fission events.

Currently FREYA only supports neutron-induced fission of ^{233}U, ^{235}U and ^{239}Pu and spontaneous fission of ^{238}U, ^{240}Pu, ^{244}Cm and ^{252}Cf. However, by keeping the physics models and experimental data sets entirely separate, the code is designed to be easily extended to additional nuclei[47]. FREYA begins modeling fission with an excited compound nucleus, so it is a valid procedure to extend the code to modeling photofission. This extension is accomplished by treating photofission of nucleus ^{A}Z as neutron-induced fission of ^{A-1}Z where the incident neutron energy E_n given by

$$E_n = E_\gamma - S_n. \tag{7.2.1}$$

Here, E_γ is the γ-ray energy and S_n is the neutron separation energy of the parent nucleus.

7.2.1 Pre-fission Neutrons

Beginning with an excited compound nucleus of well defined excitation energy E, FREYA first determines if any neutrons are emitted prior to fission. There are two processes which can lead to neutron emission: pre-equilibrium neutron emission and pre-fission neutron emission. Pre-equilibrium emission occurs when a neutron is emitted before the compound nucleus is equilibrated. This process is very unlikely at the low excitation energies used in this work, so it was not included in the calculations. Pre-fission neutrons are emitted if the equilibrated compound nucleus has an excitation energy greater than the neutron separation energy. After neutron emission the nucleus is still capable of fissioning in a process known as multichance fission, where nth chance fission occurs after n neutrons are emitted. Again at the low, sub-barrier excitation energies relevant to this work, multichance fission is suppressed, although it is not explicitly disabled in the present calculations.

7.2.2 Fragment Masses and Charges

Following pre-fission neutron emission the nucleus is split into two fragments, one light and one heavy. The mass of one of the fragments, A_f, is determined by sampling a fragment

mass probability distribution, $Y(A_f)$, and the other is given by the remaining mass from the parent nucleus. In the absence of experimental data, this distribution is modeled with a 5 Gaussian functions; 2 Gaussians to model the mass distribution caused by the spherical shell closure at $N = 82$, 2 Gaussians to model the deformed shell closure at $N = 88$, and a single Gaussian to model the broad, symmetric distribution known as the superlong mode[94]. When $Y(A_f)$ data exist for a single incident neutron energy, FREYA samples that mass distribution for all excitation energies. Experimental $Y(A_f)$ data for ^{232}Th(γ,f) and ^{238}U(γ,f) are not available, however neutron-induced fission data exists for both isotopes, and are plotted in Fig. 7.1[19]. The use of neutron-induced fission data requires the assumption that increasing the mass of the compound nucleus by one nucleon will have little effect on the fragment mass distributions. This assumption is not entirely correct, but in the absence of sufficient photofission data, it is a reasonable approximation.

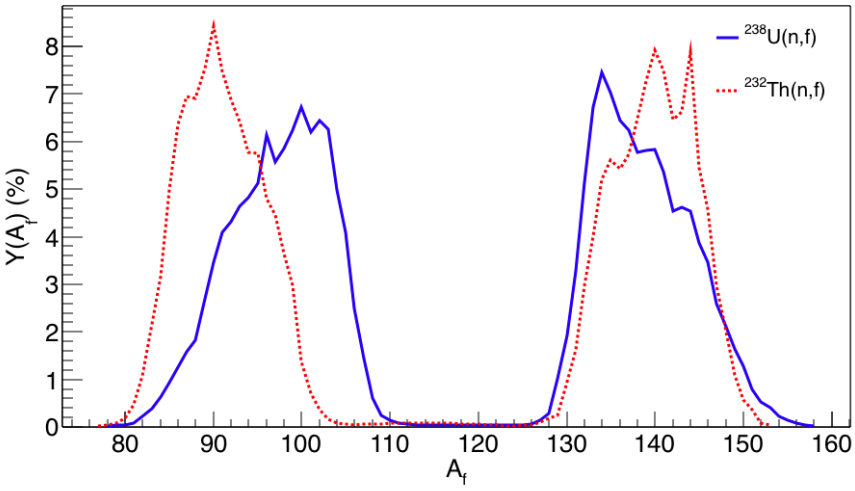

Figure 7.1: Experimental $Y(A_f)$ data from fast neutron-induced fission of ^{232}Th and ^{238}U that was used in this work. Fragment yields come from a compilation of neutron-induced fission yields which combine data from the core of a fast reactor with fission neutron spectrum yields[19].

The nuclear charge of the first fission fragment, Z_f, is chosen by sampling a probability

distribution of the form

$$P(Z_f, A_f) \propto \exp\Big(-\frac{(Z_f - \overline{Z}_f(A_f))^2}{2\sigma_Z^2}\Big), \tag{7.2.2}$$

where the mean of the distribution is defined with the assumption that the charge-to-mass ratio of the fragment is the same as the fissioning nucleus, $\overline{Z}_f(A_f) = A_f(Z_0/A_0)$. Further there is a requirement that $|Z_f - \overline{Z}_f(A_f)| \leq 5\sigma_Z$ with the dispersion σ_Z being a measured value[95]. The charge in the complementary fragment is then chosen to conserve the charge of the fissioning parent nucleus.

7.2.3 Fragment Kinetic Energies and Excitations

Once the fission fragment masses and charges are selected, the next step is to determine their kinetic and excitation energies. The total energy available to the fragments, Q_{LH}, comes from the difference between the total mass of the excited fissioning nucleus (after emission of neutrons prior to fission) and the ground state masses of the fission fragments,

$$Q_{LH} = M(^{A_0}Z_0) - M(^{A_L}Z_L) - M(^{A_H}Z_H). \tag{7.2.3}$$

In the next step, Q_{LH} is divided into the total kinetic energy (TKE) and total excitation energy (TXE) of the fragments. The average total kinetic energy of the fragments is defined in terms of the heavy fragment mass,

$$\overline{\mathrm{TKE}}(A_H, E_N) = \overline{\mathrm{TKE}}_{\mathrm{DATA}}(A_H) + d\mathrm{TKE}(E_N). \tag{7.2.4}$$

Here, $\overline{\mathrm{TKE}}_{\mathrm{DATA}}(A_H)$ is experimental data, and $d\mathrm{TKE}(E_N)$ is a correction parameter which depends on the energy of the incident neutron. As with the mass distributions, photofission data for $\overline{\mathrm{TKE}}(A_H)$ is not available for ^{232}Th and ^{238}U, so neutron-induced fission data were used instead with 2.97 MeV neutrons on ^{232}Th[96] and 1.7 MeV neutrons on ^{238}U[97]. Since

$d\mathrm{TKE}(E_N)$ is a tunable correction factor which very directly influences the energy available for the fragments to emit neutrons, its value is determined by varying the parameter until FREYA accurately reproduces the energy dependent fission neutron multiplicity. In this work $d\mathrm{TKE}(E_N)$ was set to 8.045 for ^{238}U and 3.331 for ^{232}Th. Varying $d\mathrm{TKE}(E_N)$ by 0.001 typically results in a change to the mean neutron multiplicity by $\sim 0.1\%$. Smaller changes had no apparent impact, and occasionally it would take a change of $d\mathrm{TKE}(E_N)$ by 0.003 for the multiplicity to respond, consistent with a truncation occurring at some point in the FREYA calculations.

Once $\overline{\mathrm{TKE}}$ is calculated the total fragment excitation energy is determined by energy conservation,

$$\overline{\mathrm{TXE}} = Q_{LH} - \overline{\mathrm{TKE}}. \tag{7.2.5}$$

FREYA assumes that the two fragments are in thermal equilibrium, so the excitation energy is tentatively divided by mass, $\widetilde{E}_f^* = (A_F/A_0)\overline{\mathrm{TXE}}$. These excitation energies are then refined by

$$E_f'^* = \frac{a_f(\widetilde{E}_f^*)}{a_L(\widetilde{E}_L^*) + a_H(\widetilde{E}_H^*)}\overline{\mathrm{TXE}}, \tag{7.2.6}$$

where the subscripts L and H denote the light or heavy fragment, respectively. The level density parameter $a_f(\widetilde{E}_f^*)$ is based on the formalism of Kawano *et al.*[98], which describes the number of available excited nuclear states for the fragments to occupy as a function of excitation energy. Increasing the density of available states for the fragment at a given energy increases the likelihood that the fragment will be emitted at that excitation energy. The level density parameter is given by

$$a_f(\widetilde{E}_f^*) = \frac{A_f}{e_0}\Big[1 + \frac{\delta W_f}{U_f}(1 - e^{-\gamma U_f})\Big], \tag{7.2.7}$$

where the damping coefficient $\gamma = 0.05$[99], the statistical "heat" of the excitation energy $U_f = E_f^* - \Delta_f$, Δ_f is the pairing energy of the fragment, and δW_f is the shell correction calculated by Koura *et al.*[100]. An asymptotic level density parameter e_0 depends on the

nucleus being modeled, but currently FREYA assumes that $e_0 = 10.0724$ MeV for all nuclei. Experimental data suggest that light fragments are more excited, potentially because of greater deformation at the scission point, so average excitation energies are adjusted to match the data using

$$\overline{E}_L^* = xE_L', \tag{7.2.8}$$

and

$$\overline{E}_H^* = \overline{\mathrm{TXE}} - \overline{E}_L^*, \tag{7.2.9}$$

with the parameter $x > 1$. Setting $x = 1.2$ for ^{238}U results in good agreement between the $\overline{\nu}$ calculated by FREYA and the empirical model of Lengyel *et al.*[101] which was fit to experimental data (Fig. 7.2a). The evaluation of Ref. [101] was chosen as the benchmark to reproduce in FREYA, instead of the standard ENDF/B-VII evaluation of the experimental ^{238}U(γ,f) reaction $\overline{\nu}$ data, because the ENDF/B-VII fit's slope did not agree as well with the FREYA simulated data. Attempts to fit ^{232}Th $\overline{\nu}$ data with FREYA were less successful. However, this inconsistency may arise from the fact that the experimental data sets have large uncertainties and are not in agreement with one another, as demonstrated by the disparity between the ENDF/B-VII and the evaluations of Lengyel *et al.* The ENDF/B-VII evaluation was chosen for the ^{232}Th benchmark because the slope agreed with the FREYA results better than the data of Lengyel *et al.* The value of $x = 1.2$ (along with $d\mathrm{TKE}(E_N) = 3.331$) gives the best agreement with the ENDF fit to data at lower excitation energies which are more relevant to this work.

The final step in determining the excitation energy of the fission fragments is to account for thermal fluctuations defined by

$$E_f^* = \overline{E}_f^* + \delta E_f^*, \tag{7.2.10}$$

where δE_f^* is a normal distribution with variance $\sigma_f^2 = 2\overline{E}_f^* T_f$ and the fragment temperature

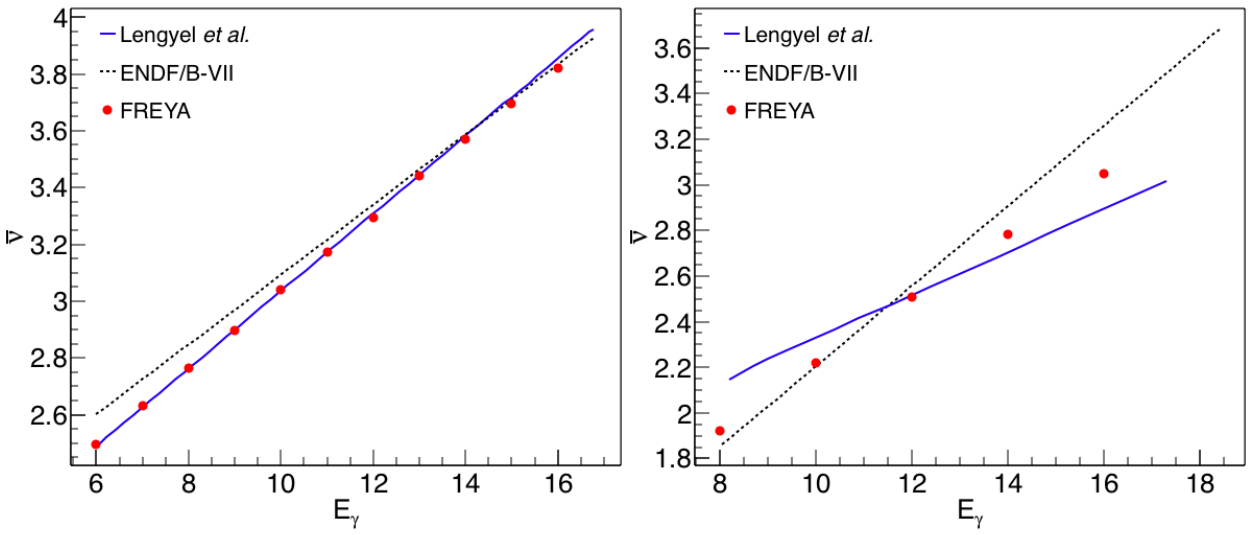

(a) ^{238}U (b) ^{232}Th

Figure 7.2: Comparison between FREYA $\overline{\nu}$ and ENDF/B-VII[77], Lengyel *et al.*[101] evaluations of the existing ^{238}U(γ,f) reaction and ^{232}Th(γ,f) reaction $\overline{\nu}$ data.

$T_f = \sqrt{\frac{E_f^*}{a_f}}$. To conserve energy, the total kinetic energy is adjusted accordingly with

$$\mathrm{TKE} = \overline{\mathrm{TKE}} - \delta E_L^* - \delta E_H^*, \tag{7.2.11}$$

where δE_L^* and δE_H^* are δE_f^* for the light and heavy fragments, respectively.

7.2.4 Neutron Emission

Prompt fission neutrons are emitted with a timescale of $\sim 10^{-18}$ s after scission, while prompt γ-rays are emitted in the range of 10^{-15}–10^{-7} s[102]. Therefore FREYA assumes the fully accelerated fission fragments de-excite by first evaporating neutrons and then emitting photons. Single neutrons are emitted iteratively until there is no longer enough excitation energy to eject another. The Q-value for neutron emission by a fragment of mass $M(^AZ)^* =$

$M(^{A}Z) + E_f^*$ is given by

$$\begin{aligned} Q_n &= M(^{A}Z)^* - M(^{A-1}Z) - m_n \\ &= M(^{A}Z) + E_f^* - M(^{A-1}Z) - m_n. \end{aligned} \tag{7.2.12}$$

Defining the neutron separation energy as $S_n(Z, A) = -M(^{A}Z) + M(^{A-1}Z) + m_n$ further simplifies the expression to

$$Q_n = E_f^* - S_n(Z, A). \tag{7.2.13}$$

The Q-value represents the maximum possible excitation energy of the daughter nucleus, where the emitted neutron carries no kinetic energy. The maximum temperature of the daughter nucleus is then given by $T_{\max} = \sqrt{\frac{Q_n}{a_d}}$, where a_d is the level density parameter of the daughter nucleus. The kinetic energy of the evaporated neutrons in the rest frame of the fragment is then sampled from a distribution of the form

$$f_n(\epsilon_n) \sim \epsilon_n e^{-\epsilon_n / T_{\max}}. \tag{7.2.14}$$

The excitation energy of the daughter nucleus is given by energy conservation, $E_d^* = Q_n - \epsilon_n$. This process is repeated until neutron emission is no longer energetically possible. The remaining fragment excitation energy is then depleted through photon emission.

7.3 Photofission Neutron Spectra

One of the major advantages of simulating photofission neutrons with FREYA is that the code is capable of producing neutron spectra at excitation energies below the fission barrier. The current models for neutron spectra from photofission rely on adapting the neutron spectra from neutron-induced fission where there are more experimental data available. Neutron spectra for neutron-induced fission are typically modeled with a Watt spectrum[77], with

the form

$$W(a,b,E') = Ce^{-aE'}\sinh\left(\sqrt{bE'}\right), \tag{7.3.1}$$

where E' is the emitted neutron energy, the normalization C is written as

$$C = \sqrt{\pi\frac{b}{4a}}\frac{e^{\frac{b}{4a}}}{a}, \tag{7.3.2}$$

and a and b are energy dependent parameters. The parameter b varies weakly with the incident neutron energy and is taken to be 1.0, while a is parameterized as

$$a = a_0 + a_1E_n + a_2E_n^2, \tag{7.3.3}$$

where E_n is the incident neutron energy and a_0, a_1 and a_2 are isotope specific constants derived from fits to experimental data[103]. To modify the formula to be applicable to photofission, the incident neutron energy is substituted with

$$E_n \rightarrow E_\gamma - S_n, \tag{7.3.4}$$

where E_γ is the incident γ-ray energy and S_n is the neutron separation energy. Additionally, the a_0, a_1 and a_2 constants are taken from an isotope with one fewer neutrons, so to calculate photofission on ^{238}U the coefficients from ^{237}U are used. This model is only a rough approximation of the photofission neutron spectrum. Additionally, it is not defined for energies below the neutron separation energy, where the entirety of the present work was performed.

FREYA does not have these limitations and can provide data well below S_n. As a rough validation of the FREYA photofission model, photofission neutron spectra were compared with the modified neutron Watt spectrum at $E_\gamma = 7$ MeV, an energy at which both models are capable of generating results. The comparison between FREYA and the modified Watt spectrum for the ^{238}U(γ,f) reaction is shown in Fig. 7.3, with overall good agreement between

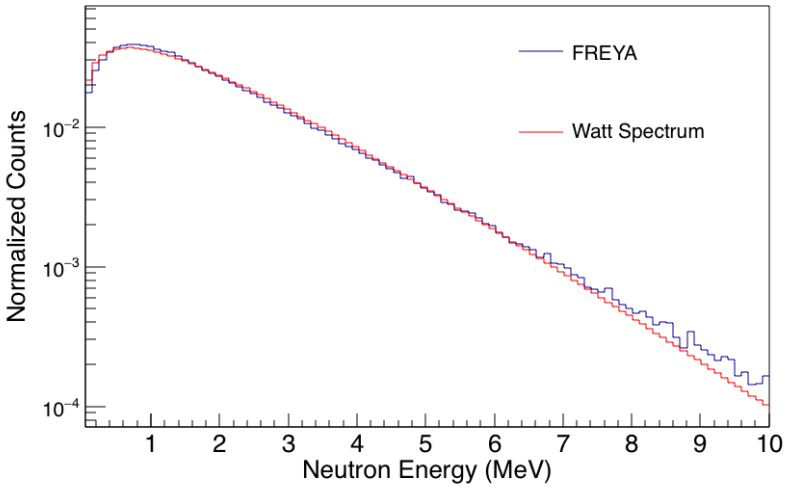

Figure 7.3: Comparison between FREYA ^{238}U photofission neutron spectrum and modified Watt spectrum at $E_\gamma = 7$ MeV.

the two models. FREYA ^{232}Th photofission neutrons are compared with a modified Watt spectrum for at $E_\gamma = 7$ MeV in Fig. 7.4.

7.4 Neutron Angular Correlations

FREYA does not consider the angular distribution of fission fragments and simply chooses the emission angle for one fragment by sampling an isotropic distribution, with the other fragment emitted in the opposite direction to conserve momentum. The neutrons emitted by the fission fragments through evaporation in the fragment rest frame are then boosted into the lab frame along that axis accordingly. This boost results in a correlation between neutron energy and emission angle relative to the fission axis, with neutrons emitted parallel to the fission axis having more energy than those emitted at perpendicular angles. For the present work the FREYA code was modified to fix the fission fragment axis to be along the z-axis, with the heavy fragment emitted in the $+z$ direction. Fig. 7.5 shows the results of a FREYA simulation for the ^{238}U(γ,f) reaction at $E_\gamma = 5.5$ MeV, with a strong correlation between neutron energy and emission angle relative to the fragment axis.

A comparison between the angular distributions for ^{232}Th and ^{238}U at $E_\gamma = 5.5$ MeV

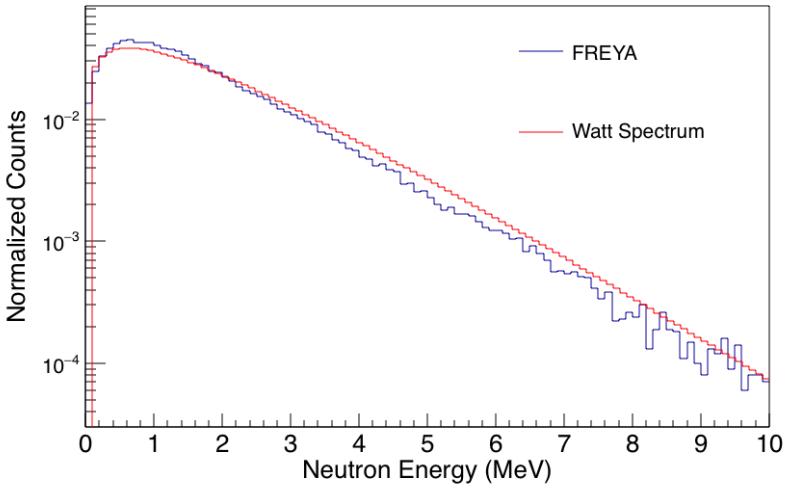

Figure 7.4: Comparison between FREYA ^{232}Th photofission neutron spectrum and modified Watt spectrum at $E_\gamma = 7$ MeV.

shown in Fig. 7.6 demonstrates that the neutrons from ^{232}Th receive more of a boost from the fission fragments than those from ^{238}U, leading to a stronger neutron asymmetry for a given fragment asymmetry.

To create a source of photofission neutrons with the appropriate angular distribution for linearly-polarized γ-ray-induced photofission, the momentum of the fission fragments from FREYA was rotated so that their fission fragment axis follows the fragment angular distribution $W(\theta, \phi)$ using formalism from section 3.3. Then, $W(\theta, \phi)$ is given by

$$W(\theta, \phi) = \frac{1}{a + 2b} \left(a + b \sin^2(\theta) + b \cos(2\phi) \sin^2(\theta) \right), \tag{7.4.1}$$

where a and b are related to a single fragment asymmetry parameter A_f by

$$A_f = \frac{b}{a}, \tag{7.4.2}$$

and a and b are normalized by $a + b = 1$. A GEANT4 photofission simulation was written for which the inputs are: the fission fragment asymmetry A_f; and a file containing the kinematic parameters of the photofission neutrons from a FREYA simulation for which the

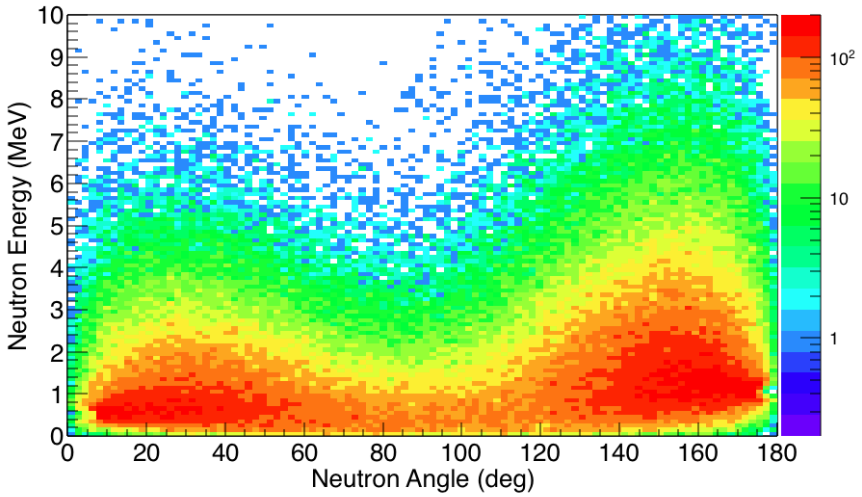

Figure 7.5: Simulated neutron energy and angle correlations for photofission of ^{238}U at $E_\gamma = 5.5$ MeV. The asymmetry in the plot between $\phi = 0°$ and $\phi = 180°$ is caused by the light fragment's emission in the $-z$ direction, while the heavy fragment is emitted in the $+z$ direction.

fission fragment axis has been set as the z axis. A fission fragment emission axis is chosen by sampling the $W(\theta, \phi)$ distribution, and the neutrons' momenta are rotated appropriately. Using this neutron generator, the relationship between the fragment and neutron angular distributions may be determined. An example of the neutron angular distribution generated by this simulation is shown in Fig. 7.7, which uses FREYA neutrons from ^{238}U(γ,f) at $E_\gamma = 5.5$ MeV and a fission fragment asymmetry of $A_f = 10$. The $sin^2(\theta)$ and $cos(2\phi)$ dependences of the neutron angular distribution are readily apparent. A fit to the angular distribution with the form of $W(\theta, \phi)$ is also shown. The results of the fit are used to determine the neutron asymmetry A_n.

Fig. 7.8 shows the neutron asymmetry A_n as a function of the fission fragment asymmetry A_f for ^{238}U and ^{232}Th. As discussed in section 3.4 the neutron asymmetry is correlated with the fragment asymmetry, but the correlation is significantly reduced by the spreading effects of the isotropic neutron emission in the fragment rest frame. Dependence of the neutron asymmetry on the energy of neutrons is shown by fitting the asymmetry after only including neutrons with energies above a threshold. As the minimum neutron energy is

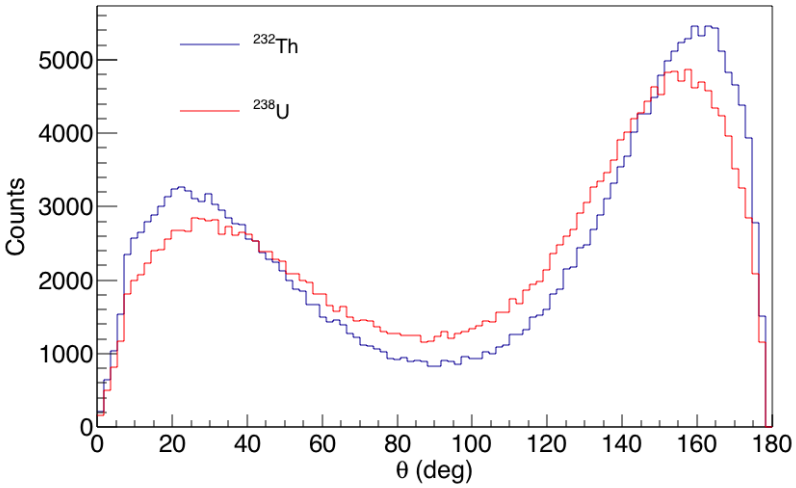

Figure 7.6: FREYA photofission neutron angular distribution relative to the fission fragment axis for ^{232}Th and ^{238}U at $E_\gamma = 5.5$ MeV.

increased the asymmetry increases, consistent with the highest energy neutrons being the most asymmetric as they receive the largest boost from the fission fragments. At this point the FREYA and GEANT4-based photofission neutron generator is ready to be incorporated into simulations of the full target and detector assembly.

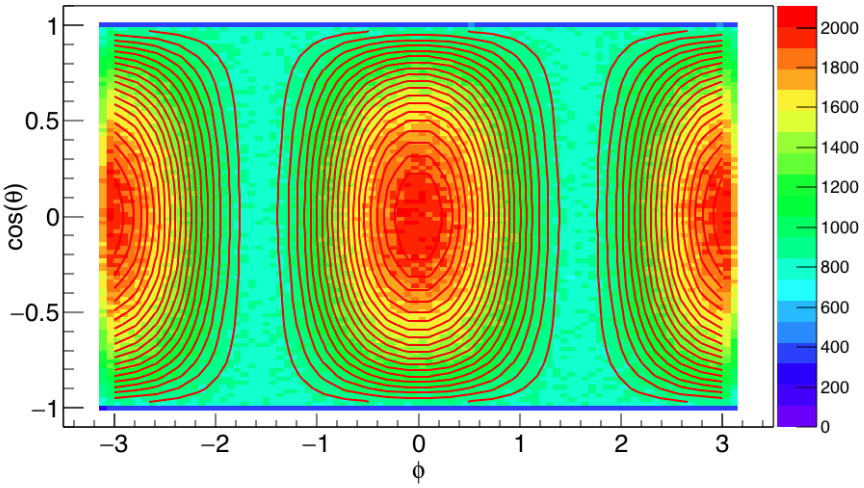

Figure 7.7: ^{238}U(γ,f) neutron angular distribution for $E_\gamma = 5.5$ MeV and $A_f = 10$. The red solid lines are the contours of a $W(\theta, \phi)$ fit.

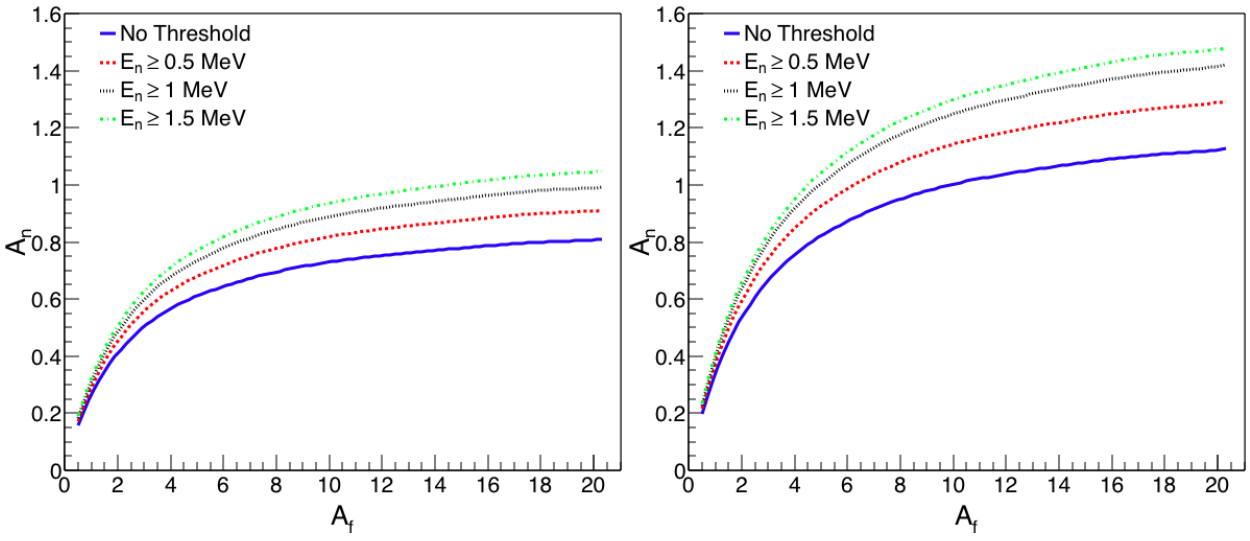

(a) ^{238}U (b) ^{232}Th

Figure 7.8: Photofission neutron asymmetries as a function of fission fragment asymmetry for several neutron energy thresholds.

CHAPTER 8: DATA REDUCTION & ANALYSIS II

8.1 Introduction

This chapter will cover the analysis and data reduction techniques employed to measure the neutron polarization asymmetries, neutron multiplicities and absolute cross sections for the ^{232}Th(γ,f) and ^{238}U(γ,f) reactions. Two neutron multiplicity analysis techniques are developed in sections 8.2, 8.3.4 and 8.5. Characterizations of background neutrons will be described in section 8.3, including a never-before-measured accelerator-induced background. Analysis of the neutron polarization asymmetries in the INVS detector is discussed in section 8.4. A Monte Carlo model for fitting the photofission neutron multiplicity distributions was developed and is described in section 8.5.2. Finally the absolute photofission cross section analysis is discussed in section 8.6.

8.2 Moderated Neutron Time Distribution

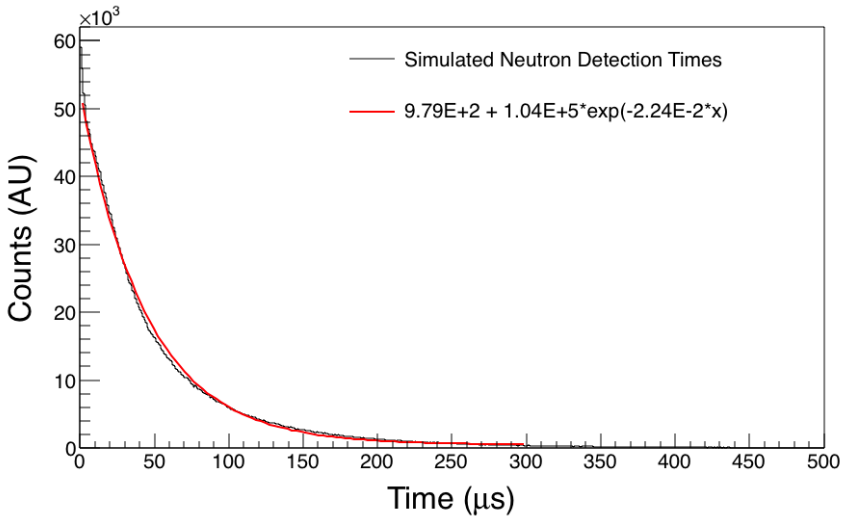

Figure 8.1: Simulated neutron detection times in GEANT4 along with an exponential fit.

Determining the detected neutron multiplicities requires setting a time window in which neutrons from the same fission event may be counted. The time window must be long enough that any correlated neutrons from a single fission event will either have been detected or escaped the detector; however, making it excessively long increases the likelihood that uncorrelated neutrons from other fission events or backgrounds are counted as well. Thus a clear understanding of the neutron detection timescale is necessary. Neutrons of MeV energy (fast neutrons) scatter off of the H and C nuclei until thermalized, and can then be detected by traveling into one of the ^{3}He PCs. Fast neutrons travel much faster than the thermal neutrons ($\sim 10^7$ m/s vs $\sim 10^3$ m/s), so the initial moderation process occurs in the timescale of < 1 μs. The detection time is then dominated by the random walk of the thermal neutrons within the polyethylene moderator, which can take anywhere up to 100s of μs. Because the random walk timescale is the same for any initial neutron energy, the neutron detection times are independent of the neutron energy. To evaluate this process, GEANT4 simulations of the INVS detector were performed and the detection time for each neutron was recorded, where the neutron is always emitted at time $t = 0$ and detected some time after that. The results of one simulation are shown in Fig. 8.1 along with an exponential fit with a 31 μs half life.

A direct comparison of neutron detection time can not be generated from the data because there is no 'start' signal for each fission event. The closest comparison is to instead sort through the detected neutrons in chronological order starting at $t = 0$. The first neutron to be detected generates a 300 μs gate following it, and any neutrons detected in the gate are added to a time distribution with the detection time being the time relative to the start of the gate. Another gate is triggered by the first chronological neutron occurring outside of the first gate, so that any neutron can only be counted once. Fig. 8.2 shows a schematic version of the logic behind this process of multiplicity gating.

A Monte Carlo simulation was developed to model the neutron detection times observed

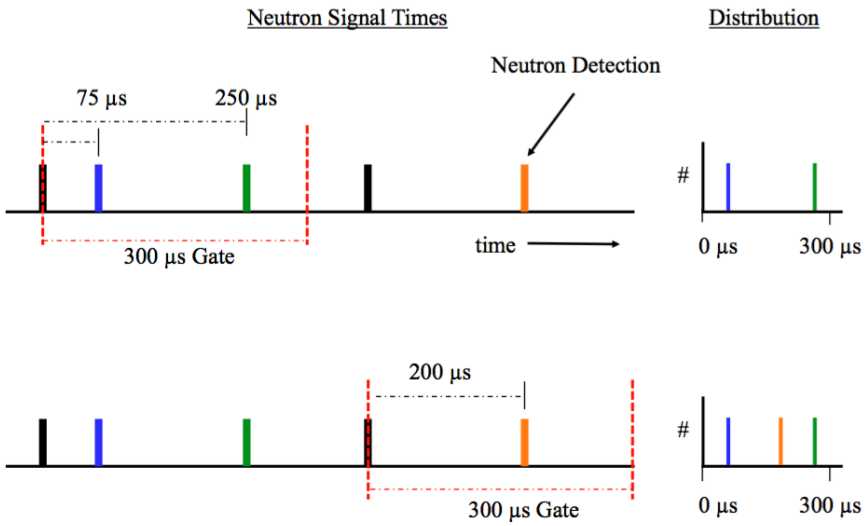

Figure 8.2: Schematic demonstrating the logic of multiplicity gating. The first neutron detection creates a 300 μs gate. A neutron signal time distribution is filled with the detection times relative to the start of the gate. The first neutron detection to occur after the end of the 300 μs gate defines the start of the next gate.

in the INVS detector. A total fission event rate $R_{fission}$ was defined as

$$R_{fission} = \frac{R_{neutron}}{\epsilon_{INVS}\bar{\nu}} \tag{8.2.1}$$

where $R_{neutron}$ is the detected neutron rate in the INVS detector, ϵ_{INVS} is the detector efficiency and $\bar{\nu}$ is the mean neutron multiplicity per fission. A reasonable estimate of $\bar{\nu} = 2.5$ for the multiplicity was used based on a previous measurement of the photofission neutron multiplicity distribution for ^{238}U at similar E$_\gamma$[71]. The Monte Carlo simulation populated a length of time with fission events randomly distributed in time so that the average event rate was $R_{fission}$. For each fission event a neutron multiplicity was selected from a Gaussian distribution with a mean of $\bar{\nu}$ and a spread of $\sigma = 1$. Each neutron had a probability ϵ_{INVS} of being detected, and would be detected at a time after the fission event determined by sampling an exponential decay function with a half life of 31 μs. The detected neutrons were ordered in time to produce a data stream identical to the measured data, and were then analyzed using the same gating technique. This Monte Carlo simulation is described

in more detail in section 8.5.2.

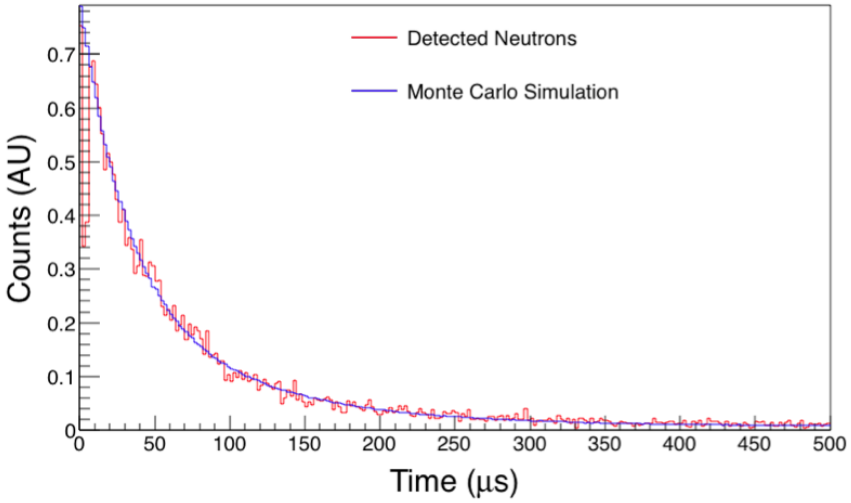

Figure 8.3: Comparison of measured data and Monte Carlo simulation of neutron time distributions for ^{238}U(γ,f) at $E_\gamma = 5.1$ MeV.

A data set with $E_\gamma = 5.1$ MeV incident on a ^{238}U target was chosen to be compared with a simulation because the fission neutron detection rate was significantly higher than the background rate, but was still low enough that the probability of two fission events overlapping was small and thus the observed time distribution would be more directly determined by the random walk of the thermal neutrons and not influenced by the accidental overlap of events. The simulated and measured time distributions are compared in Fig. 8.3 and agree well with one another. With the neutron detection timescale half life of 31 μs validated, a gate length of 300 μs was chosen for the background multiplicity analysis as it will contain effectively all of the correlated neutrons associated with a single event (99.9%) while still being short enough not to allow for significant overlap of uncorrelated events at low event rates ($\sim<$ 50 Hz).

8.3 Background Analysis

There were three sources of background neutrons present throughout this work: cosmic-ray induced neutrons, neutrons from the D(γ,n) reaction occurring in the detector moderator,

and neutrons from contaminations in the HIγS beam inducing (γ,xn) reactions on the targets. The backgrounds will be described in more detail in sections 8.3.1, 8.3.2 and 8.3.3. The neutron background caused by cosmic-rays can be measured directly, but ultimately the other two sources of background neutrons had to be measured simultaneously with a Pb target, using a method described in Section 8.3.4. Additionally, an upper limit was placed on the E_γ for ^{238}U photofission analysis because of the presence of neutrons from the ^{238}U(γ,n) reaction, as will be discussed in section 8.3.5.

8.3.1 Cosmic-ray Induced Neutrons

Cosmic-rays are high energy particles such as protons which collide with the Earth's atmosphere to produce cascades of secondary particles such as electrons, photons and muons. The cosmic-ray muons can produce spallation neutrons by colliding with and fragmenting the nuclei in any material. Because there is material all around the target area the resulting cosmic-ray neutrons can come from any direction, so the INVS detector was surrounded with neutron shielding on all sides. Simulations performed for the MAJORANA experiment indicate that ~ 30 cm of borated polyethylene shielding will reduce the flux of $0 - 20$ MeV cosmic-ray induced neutrons by a factor of 3.3, with diminishing returns for thicker shielding[104]. The borated polyethylene shielding is even more effective at stopping lower energy cosmic-ray neutrons that have scattered multiple times. As a result, an approximately 30 cm of borated polyethylene shielding around the INVS detector reduced the detected cosmic ray background rate by about a factor of 6, from ~ 3 Hz to 0.537 ± 0.003 Hz. The cosmic-ray neutron background rate is constant in time making it easy to subtract from the data.

8.3.2 Neutrons Produced by the D(γ,n) Reaction

There are very few nuclei that produce neutrons from interactions with γ-ray beams with $E_\gamma \leq 6.3$ MeV so there are relatively few possible sources of γ-ray beam induced background. One notable exception is deuterium, with the threshold for the D(γ,n) reaction being 2.22

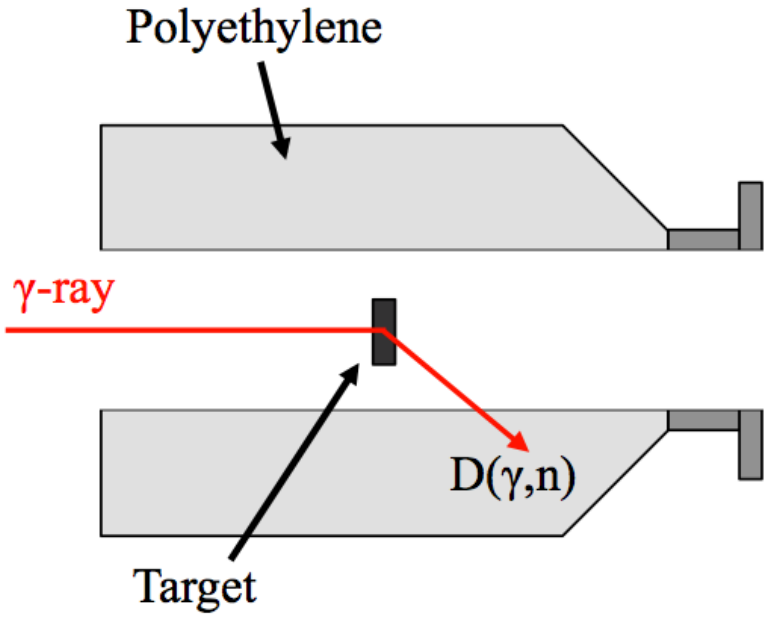

Figure 8.4: Diagram of Compton scattering D(γ,n) background neutron production in the INVS detector.

MeV. Because ^{nat}H has a deuterium abundance of 0.016% and the D(γ.,n) reaction cross section peaks at 2.5 mb, a significant amount of H needs to be in the path of the γ-ray beam for this background to be measurable. Water vapor in the air is removed as a potential background source through the means of a vacuum pipe. The polyethylene moderator of the INVS, however, cannot be removed as it is an integral part of the detector. While the moderator of the INVS is not placed directly in the path of the HIγS beam, γ-rays in the beam can Compton scatter off of the atomic electrons in the thick targets of ^{232}Th, ^{238}U, and ^{nat}Pb and into the polyethylene moderator of the INVS as shown in Fig. 8.4, producing neutrons through the D(γ,n) reaction on the deuterium present in the ^{nat}H component of the polyethylene. Because the Compton scattering and the D(γ,n) reaction cross sections are both energy dependent, this background rate has the potential to change with the energy of the γ-ray beam, so it was measured at each beam energy using a ^{nat}Pb target. At $E_\gamma = 6$ MeV the detected neutron rate from the D(γ,n) reaction background was 1.1 ± 0.2 Hz.

8.3.3 Bremsstrahlung Contamination of the HIγS Beam

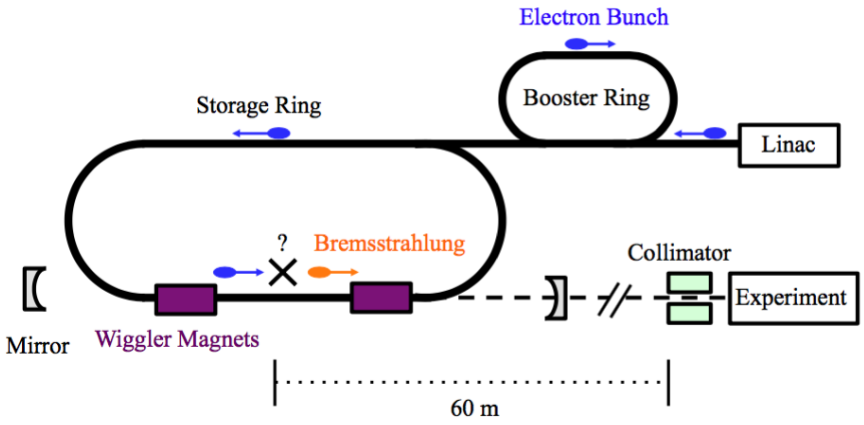

Figure 8.5: Schematic of bremsstrahlung production by the HIγS electron storage ring.

In the course of this work an additional beam-induced background was observed and identified: a high energy bremsstrahlung contamination of the γ-ray beam. The potential existence of a bremsstrahlung component of the HIγS beam had been discussed in the past, but prior to this work there had been no direct measurements of this background. The exact mechanism which causes the bremsstrahlung has not been identified and is beyond the scope of this work. As shown in Fig. 8.5, during normal operation electrons travel in the storage in the direction of the target. Any interaction between the high energy electrons and residual gas, stray electric or magnetic fields or physical equipment in the beamline would cause bremsstrahlung with some fraction of the flux directed towards the target. For this work the electron beam energy in the storage ring ranged from approximately 400 to 500 MeV, meaning that any bremsstrahlung produced would have that as the endpoint energy. The exact shape of the bremsstrahlung spectrum depends on what material the electrons were scattering on and was not determined in this work. A representative bremsstrahlung spectrum of 400 MeV electrons incident on a thin converter as simulated in GEANT4 is shown in Fig. 8.6.

To verify that the background was caused by the electrons in the storage ring and not by the primary γ-ray beam, measurements were made with the HIγS facility operating in

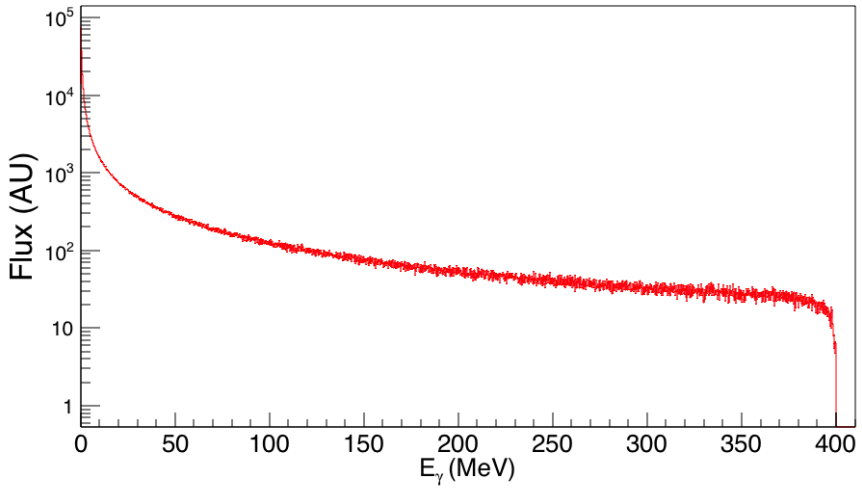

Figure 8.6: Simulated bremsstrahlung spectrum from 400 MeV electrons incident on a thin Ta plate.

'single bunch mode' in which there was only a single electron bunch in the storage ring instead of the two used in normal operation. The single electron bunch would produce FEL photons but would never collide with counter propagating FEL photons since there wasn't a second electron bunch to scatter on. This meant that the FEL photons in the lasing cavity were never inverse-Compton scattered to MeV energies and a γ-ray beam would not be produced. Any neutrons detected by the INVS above the cosmic-ray background would be from the backgrounds produced by electrons in the storage ring. Measurements were made with multiple storage ring energies and targets, consistently producing neutrons with rates of a 1-3 Hz above the cosmic-ray background. A measurement made in single bunch mode operation with no target in the INVS detector yielded a signal rate of 0.04 ± 0.05 Hz, consistent with just a cosmic-ray neutron background.

Additionally, measurements were made in which the HIγS beam was on and in normal operation, but a thick Ta beam stop was positioned in the γ-ray beam far upstream of the collimator. In this configuration there was no additional count rate observed above the cosmic-ray background, indicating that the neutrons associated with the electron storage ring weren't being produced within the accelerator itself. Instead, the neutrons must be

produced in targets placed in the INVS detector by a component of the HIγS beam which is not generated through inverse-Compton scattering and which is capable of generating neutrons on ^{nat}Pb, for which the isotope with the lowest energy threshold is ^{207}Pb with a threshold of E_γ = 6.74 MeV for the ^{207}Pb(γ,n) reaction. It should be noted that, in the configuration of the HIγS facility used for this work, the primary γ-ray beam was not capable of exceeding 6.3 MeV (FEL λ=780 nm). Thus the accelerator-induced background must be some form of bremsstrahlung generated in the storage ring.

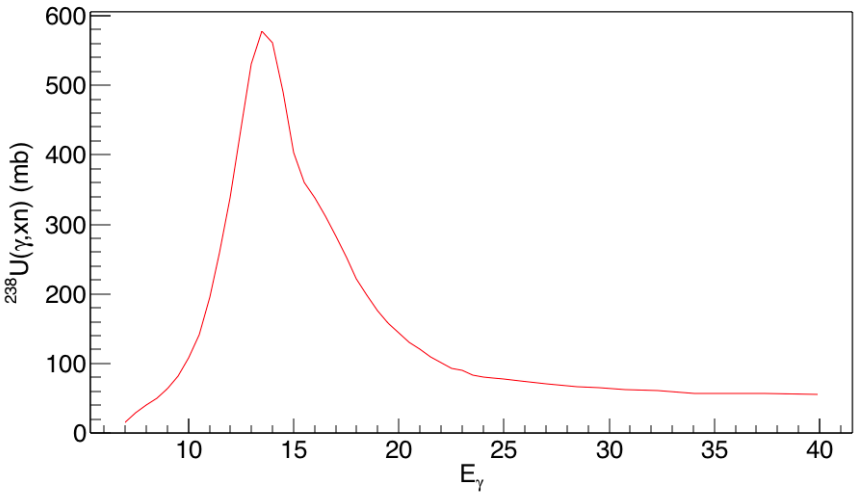

Figure 8.7: The total ^{238}U(γ,xn) reaction cross section[78].

What makes this γ-ray beam contamination so problematic for this work is that as shown in Fig. 8.6, it extends into the GDR, the region between 10 and 20 MeV in which photonuclear reactions like (γ,n), (γ,2n) and (γ,f) reach their maximum values. The cross section for the ^{238}U(γ,xn) reaction is shown in Fig. 8.7. At its peak the total (γ,xn) cross section is nearly 600 mb, roughly 6 orders of magnitude greater than the ^{238}U(γ,f) reaction cross section in the μb range being probed by the primary γ-ray beam at 5 MeV. Even if the background bremsstrahlung has a flux many orders of magnitude less than the primary HIγS beam, it can still produce neutrons at a comparable or even greater rate than the main γ-ray beam. Consequently the bremsstrahlung background must be measured very precisely.

8.3.4 Measuring the Compton and Bremsstrahlung Backgrounds

Although a bremsstrahlung background could be observed while operating the HIγS facility in single bunch mode, since the exact cause of the bremsstrahlung is not fully understood there is no guarantee that the bremsstrahlung background in normal operation with two electron bunches will simply be twice that of single bunch mode. In fact measurements of the single bunch mode bremsstrahlung background made on different days with the same storage ring parameters and target yielded different neutron rates, with variations of 20% observed. The variability in the bremsstrahlung contamination dependent on beam tuning necessitated measuring it while in normal two bunch operation, and directly before or after making a measurement with a ^{232}Th or ^{238}U target in order to capture the rate as it was during the photofission measurement. However, during normal operation the main γ-ray beam will be on target and therefore the Compton scattering induced D(γ,n) reaction background will be present as well. Thus the bremsstrahlung and Compton backgrounds were measured simultaneously by directing the HIγS beam on a ^{nat}Pb target, and the relative contributions of the two backgrounds were determined by exploiting their unique neutron multiplicity distributions.

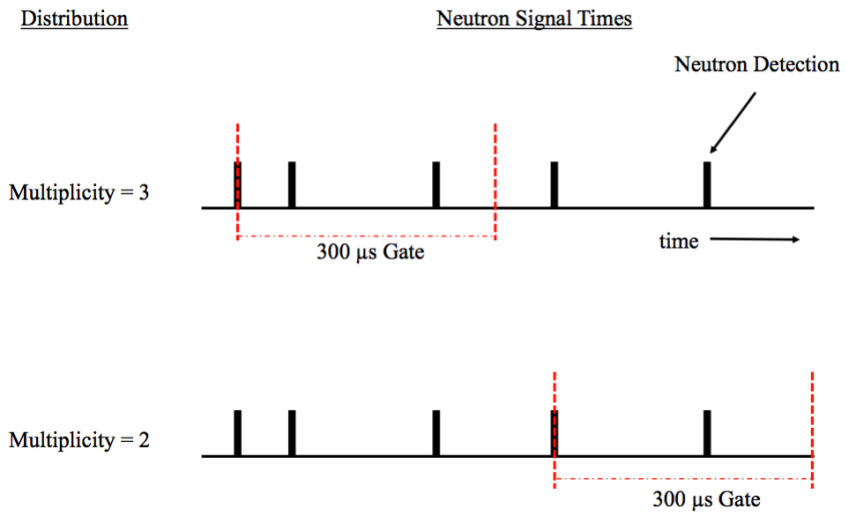

Figure 8.8: Schematic of detected neutron multiplicity logic.

Background multiplicities are defined by grouping together neutrons within 300 μs gates,

as depicted in Fig. 8.8 . The neutron detection events for a data taking run are placed in chronological order, and the first detected neutron creates a 300 μs gate. The multiplicity is defined as the total number of neutrons in the gate including the one which created it, meaning that the minimum detected multiplicity is 1 by definition. The next 300 μs gate is created on the first neutron that falls outside of the previous gate so that any neutron will only be counted towards a single multiplicity event.

The Compton scattering background only produces neutrons through the D(γ,n) reaction, meaning that each neutron detection event will be multiplicity 1. This assumption will remain true as long as the rates are low enough that random overlap of fission and background events is unlikely, which is the case for all the backgrounds measured in this work. The bremsstrahlung contamination will generate neutrons through the (γ,n), (γ,2n), (γ,3n) and (γ,f) reactions of ^{nat}Pb, with the detected multiplicity distribution being a function of the relative contributions of each reaction and the efficiency of the INVS to the neutrons from each reaction. As the energy of the electrons in the storage ring increases, the endpoint energy of the bremsstrahlung spectrum will increase and the overall photon flux at lower energies will increase as well. However the shape of the bremsstrahlung spectrum will remain roughly constant over the GDR energy range of $10 - 20$ MeV which is responsible for a vast majority of the neutron production arising from the Pb(γ,xn) reaction. The relative contributions of the various photonuclear reactions will then remain constant, and therefore so will the multiplicity distribution caused by the bremsstrahlung contamination on a particular target. The only aspect of the bremsstrahlung-induced background that will change with the beam tune and energy is the overall rate of neutron production.

The multiplicity of the bremsstrahlung-induced neutron background on the ^{nat}Pb target was measured by operating the HIγS facility in single bunch mode and detecting neutrons while the ^{nat}Pb target was positioned in the center of the INVS detector. The neutrons were grouped into multiplicity events using the logic depicted in Fig. 8.8, the multiplicity events were summed and then divided by the run time to get the multiplicity rates, e.g.

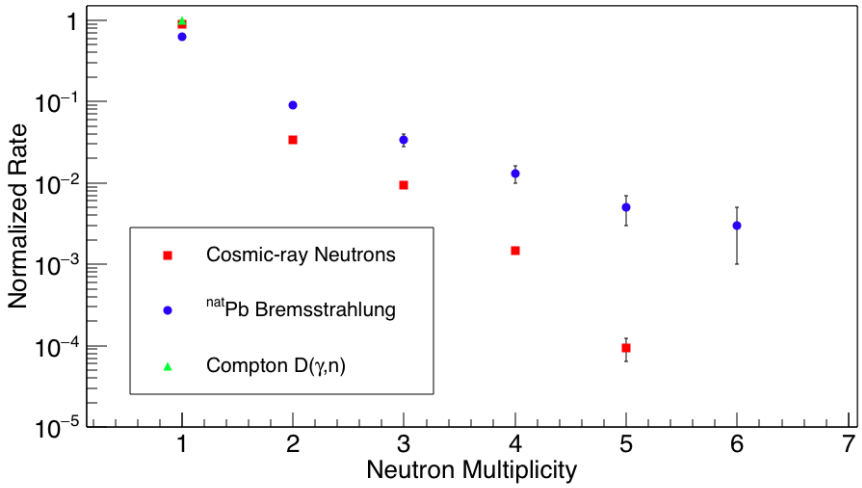

Figure 8.9: Neutron multiplicity rates for various backgrounds, normalized to 1 Hz.

the rate of multiplicity 1 events, the rate of multiplicity 2 events, etc. This same analysis was performed on the cosmic-ray neutron backgrounds that were measured over several nights when the γ-ray beam was not present. For the low neutron count rates typical of background measurements, it was assumed that the multiplicity rates could be added and subtracted linearly without needing to account for high-rate pileup effects. The shape of the bremsstrahlung background neutron distribution resulting from the ^{nat}Pb(γ,xn) reaction was then determined by subtracting the cosmic-ray induced neutron multiplicity rates from the single bunch mode measurement with the ^{nat}Pb target. The multiplicity distributions for the three sources of background with the ^{nat}Pb target are shown in Fig. 8.9, each normalized to a neutron count rate of 1 Hz. The cosmic-ray neutron background having multiplicities greater than 1 is consistent with spallation events in which multiple neutrons are created in the same interaction, either in the detector material or above it.

The Compton scattering and bremsstrahlung-induced contributions to the neutron background during the presence of the main HIγS beam were measured by placing the ^{nat}Pb target in the center of the INVS detector and measuring the multiplicity rates, using the same gating logic as shown in Fig. 8.8. The cosmic-ray neutron background multiplicity rates

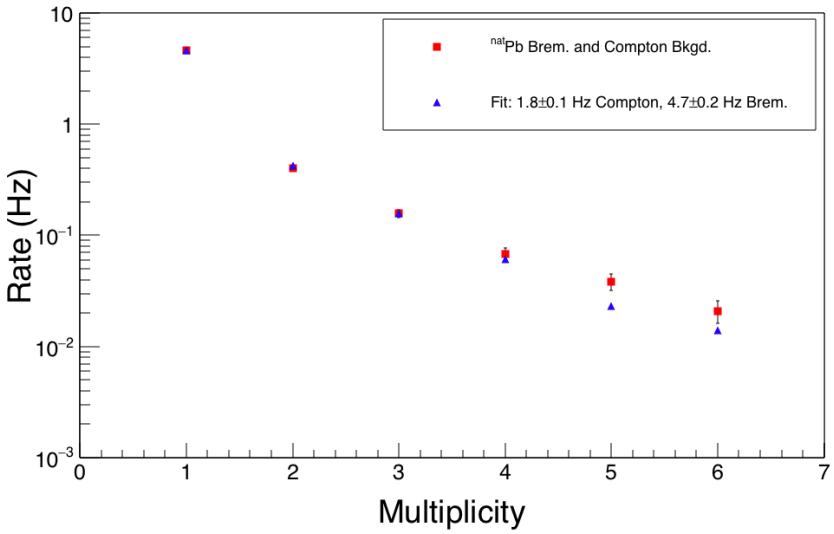

Figure 8.10: Fit to the bremsstrahlung-induced and the D(γ,n) reaction-induced backgrounds, using the normalized multiplicity distributions.

were subtracted, leaving only the Compton and bremsstrahlung components. The resulting multiplicity rate distribution was fit using the normalized bremsstrahlung and Compton background multiplicity distributions to determine their relative contributions to the background neutron rates. The fit results for a measurement of the Compton scattering and bremsstrahlung-induced backgrounds at E_γ = 5.5 MeV are shown in Fig. 8.10, with the measured background multiplicity rates compared to the reconstruction from the fit. Typical uncertainties in those two background rates were about 10%. The measured neutron background rates are plotted in Fig. 8.12 as a function of E_γ, relative to the primary γ-ray beam flux.

Once the rates of the bremsstrahlung and Compton-scattering induced backgrounds were measured with the ^{nat}Pb target the backgrounds for the ^{232}Th and ^{238}U could be determined by scaling the rates appropriately. A scaling factor $C_{t/Pb}$ is defined as

$$R_t(bkgd) = C_{t/Pb}(bkgd)R_{Pb}(bkgd), \tag{8.3.1}$$

where R_t is the detected neutron rate for either the ^{238}U or ^{232}Th target, R_{Pb} is the detected neutron rate with the ^{nat}Pb target and $bkgd$ specifies if the background is Compton scattering-induced ($bkgd = Compton$) or bremsstrahlung-induced ($bkgd = Brem$).

The bremsstrahlung scaling factor $C_{t/Pb}(Brem)$ was measured for the ^{232}Th and ^{238}U targets by running the HIγS facility in single bunch mode and measuring the neutron production rates on all 3 targets sequentially, with the cosmic-ray background subtracted. Based on those observed relative bremsstrahlung-induced neutron rates, $C_{U/Pb}(Brem) = 1.17$ and $C_{Th/Pb}(Brem) = 1.38$. The normalized bremsstrahlung-induced background rates on ^{232}Th and ^{238}U are shown in Fig. 8.11.

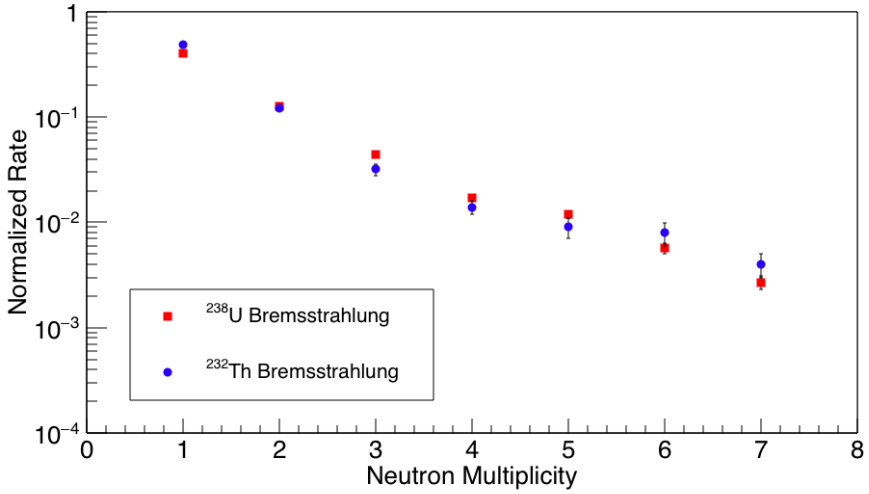

Figure 8.11: Normalized neutron multiplicity rates for bremsstrahlung-induced backgrounds on ^{232}Th and ^{238}U.

The Compton scattering induced neutron background rate is proportional to the number of electrons in the target, so the scaling factor is given by

$$C_{t/Pb}(Compton) = \frac{Z_t \rho_t \ell_t A_{Pb}}{Z_{Pb} \rho_{Pb} \ell_{Pb} A_t}, \tag{8.3.2}$$

where Z is the nuclear charge, ρ is the density, ℓ is the length and A is the mass number. $C_{U/Pb}(Compton) = 0.520$ and $C_{Th/Pb}(Compton) = 0.633$.

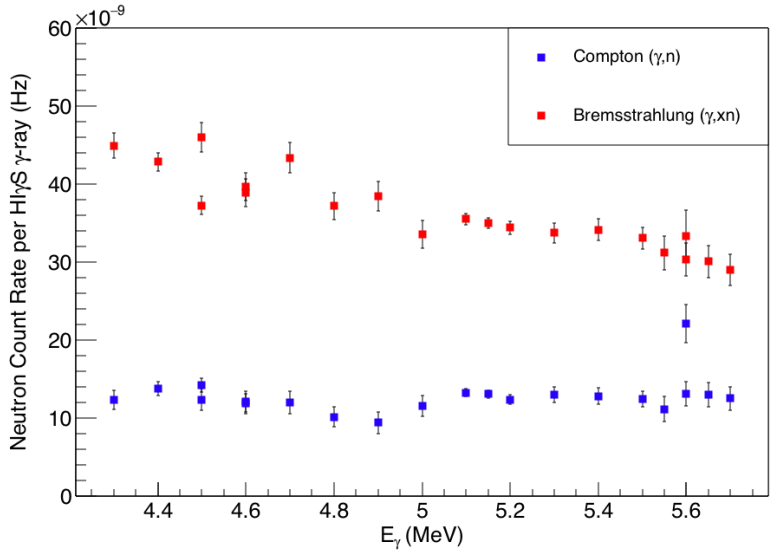

Figure 8.12: HIγS beam-induced background neutron count rates observed with ^{nat}Pb target, normalized to the flux of the primary γ-ray beam.

The Compton scattering-induced and bremsstrahlung-induced neutron background rates, normalized to the flux of the HIγS γ-ray beam for a range of E_γ, are shown in Fig. 8.12. The present work represents the first measurement of the bremsstrahlung contamination of the HIγS beam in this energy regime. The absolute bremsstrahlung-induced count rate increases with the energy of the electron storage ring, but the flux of the HIγS beam increases at an even faster rate with storage ring energy resulting in the relative contamination of the γ-ray beam's decreasing with increasing E_γ. The total bremsstrahlung flux, ϕ_{brem}, may be estimated using

$$\phi_{brem} = \frac{R_{brem} A_{Pb}}{\sigma_{Pb} \ell_{Pb} \rho_{Pb} N_A F_{GDR} \varepsilon_{INVS}}, \tag{8.3.3}$$

where R_{brem} is the detected bremsstrahlung neutron rate ($\sim$ 4 Hz on average), A_{Pb} is atomic mass of ^{nat}Pb (207.2), σ_{Pb} is the average (γ,xn) reaction cross section over the GDR ($\sim$ 400 mb for all naturally abundant isotopes of Pb)[78], ℓ_{Pb} is the ^{nat}Pb target thickness (1.6 cm), ρ_{Pb} is the ^{nat}Pb target density (11.34 g/cm^3), N_A is Avogadro's number, F_{GDR} is the fraction of the bremsstrahlung spectrum which falls in the GDR (estimated to be 9% using the simulated data plotted in Fig. 8.6), and ε_{INVS} is the INVS detector efficiency

(estimated to be 20%). With these assumptions, the total bremsstrahlung flux is estimated to be $\sim 10^4$ γ/s, which is a $\sim 10^{-4}$ contamination of the primary HIγS beam. The resulting bremsstrahlung contamination just in the GDR energy region is $\sim 10^3$ γ/s.

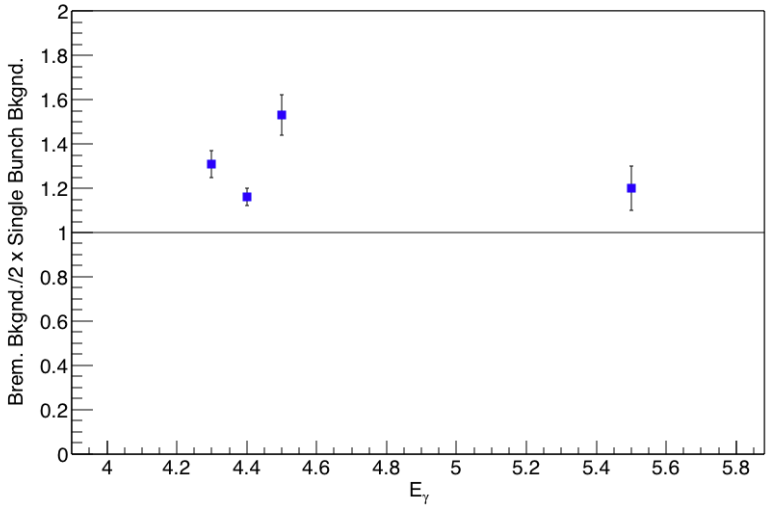

Figure 8.13: Ratio of measured bremsstrahlung-induced background with primary HIγS beam and estimate of bremsstrahlung background from doubling the rate observed in single bunch mode measurements (shown as a horizontal line).

The viability of estimating the bremsstrahlung background by measuring the rate in single bunch mode and simply doubling it was investigated. Data sets were selected in which a single bunch mode measurement with a ^{238}U or ^{nat}Pb target was made directly before or after a measurement in normal operation with the ^{nat}Pb target, so that any time or beam tune dependent effects would be minimized. As shown in Fig. 8.13 the estimated bremsstrahlung background from doubling the single bunch mode measurements consistently under-predicts the observed background rate. Thus the direct measurement of the bremsstrahlung background with normal HIγS beam in two-bunch mode operation is necessary.

8.3.5 ^{238}U(γ,n) Reaction Background Neutrons

Neutrons from the ^{238}U(γ,n) reaction were a background present only in measurements with the ^{238}U target with $E_\gamma > 6$ MeV because above that energy the high energy tail of the

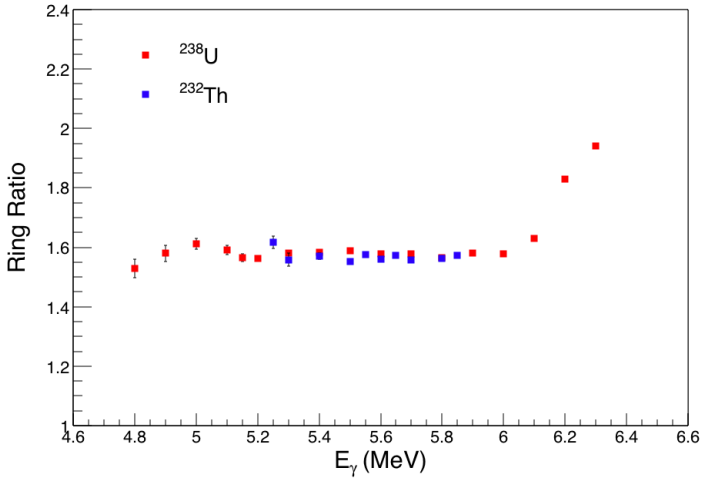

Figure 8.14: Ring ratios observed for measurements of neutrons from the ^{232}Th(γ,f) and ^{238}U(γ,f) reactions, with a sharp increase in ^{238}U above E_γ = 6 MeV caused by the γ-ray beam spectrum crossing the ^{238}U(γ,n) reaction threshold at 6.15 MeV.

HIγS γ-ray beam crossed the ^{238}U(γ,n) reaction threshold of 6.15 MeV. The (γ,n) reaction background was difficult to characterize because it changes rapidly with energy and depends strongly on the overlap of the γ-ray beam spectrum and the ^{238}U(γ,n) reaction cross section, which is not precisely known near the reaction threshold. Since the (γ,n) reaction neutrons were produced by γ-rays just above the reaction threshold, the neutron energies were low compared to the fission neutrons and thus were more likely to be detected.

Although the ^{238}U(γ,n) reaction-induced background could not be sufficiently quantified to measure the fission neutron multiplicities and photofission cross sections, the effects of the background could be observed in the ring ratio of the INVS detector. The inner ring and outer rings of the INVS have different efficiency dependence on neutron energy, and thus the ratio R_r of counts in the inner ring to the outer ring is a measure of the average incident neutron energy.

Fig. 8.14 shows the observed R_r for measurements with the ^{232}Th and ^{238}U targets, as a function of E_γ. The value of R_r remains constant for the ^{232}Th target for all E_γ and is flat for the ^{238}U target at lower E_γ, with a sharp increase at higher E_γ consistent with the γ-ray spectrum crossing the ^{238}U(γ,f) reaction threshold. The lower energy (γ,n) neutrons

produced just above the threshold would be more likely to be detected in the inner INVS ring, and consequently increase the value of R_r. Based on the observed R_r, the ^{238}U(γ,f) reaction cross section data was contaminated with neutrons from the ^{238}U(γ,n) reaction for $E_\gamma > 6$ MeV.

8.4 Prompt Photofission Neutron Asymmetry Analysis

Asymmetries in the angular distribution of the prompt photofission neutrons about the polarization axis of the γ-ray beam were determined by fitting the asymmetries observed in the INVS detector and then using GEANT4 simulations to account for the neutron interactions in the detector moderator and target assembly. The method for fitting the neutron detection asymmetries in the INVS will be discussed in section 8.4.1, and the simulation results will be discussed in section 8.4.2.

8.4.1 Neutron Asymmetries in the INVS Detector

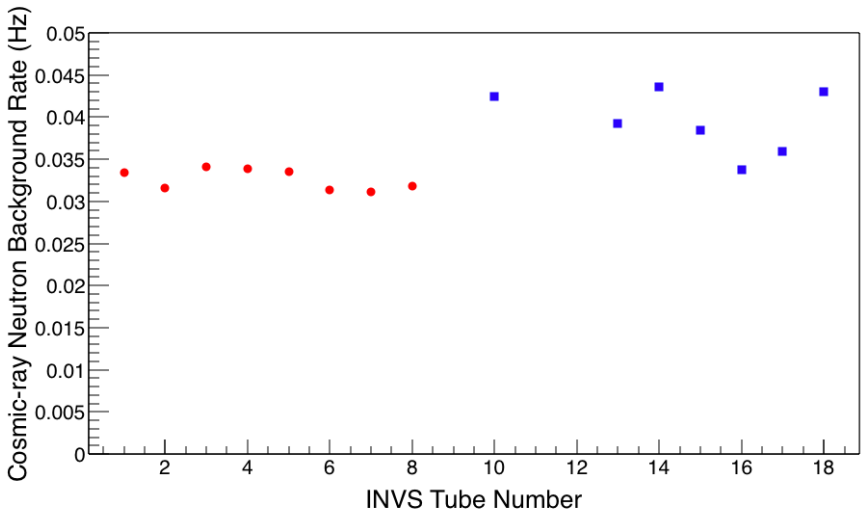

Figure 8.15: Cosmic-ray induced background neutron rates. Statistical error bars are smaller than the markers.

Background subtraction was performed on the raw INVS neutron yields prior to scaling each PC by its relative efficiency. Cosmic-ray induced neutron background yields are plotted

in Fig. 8.15. The outer ring of the INVS detector has a greater rate since the cosmic-ray neutron background is primarily produced outside of the INVS detector. Single bunch mode measurements of the bremsstrahlung background did not have good enough statistics to be used for background subtraction, but the observed yields were consistent with the yield in each PC tube's being proportional to its relative efficiency. This would be the case if the bremsstrahlung-induced neutrons were emitted with no asymmetry in the ϕ angle. Given that the bremsstrahlung beam should be unpolarized this is a reasonable assumption. Additionally the Compton scattering induced neutron background can also be treated as having no preferred polarization direction. The linear-polarization of the γ-ray beam does introduce an asymmetry in the angular distribution of the Compton-scattered γ-rays, with an enhancement in the scattering cross section for $\phi = 90°, 270°$. However, for the E_γ range used in the present work, the asymmetry is small with less than 30% more scattering in the plane perpendicular to the polarization axis of the beam[105]. Therefore for the purposes of this work, the probability of the neutron creation is treated as equal throughout the detector moderator with respect to ϕ.

The Compton scattering and bremsstrahlung-induced background rates were determined with the multiplicity fitting method described in Section 8.3.4. After subtracting background neutrons and scaling the yields per PC tube by its relative efficiency, the detector asymmetry was determined by fitting the yields in the inner and outer INVS rings with a distribution of the form $a(1 + b\cos 2\phi)$, where b is the detector asymmetry A_d. A fit for the neutron detector asymmetries for the photofission of ^{238}U at $E_\gamma = 5.6$ MeV is shown in Fig. 8.16.

8.4.2 Simulated Asymmetries in the INVS Detector

The interaction of the neutrons in the INVS detector and the target materials was modeled using the GEANT4 simulation described in section 6.4.5. In addition to neutron energy loss and the change in direction from scattering within the target and detector materials, the simulation also accounts for the possibility of neutron induced fission caused by the

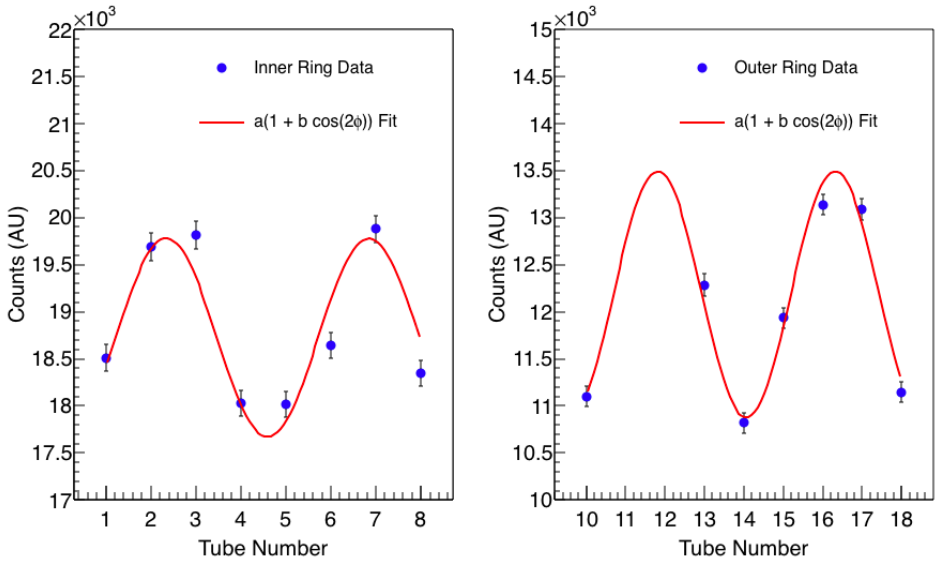

Figure 8.16: Data and fits for the detected neutron asymmetry in the inner and outer rings of the PC tubes in the INVS for $E_\gamma = 5.6$ MeV on ^{238}U.

interaction of the photofission neutrons within the thick ^{232}Th or ^{238}U target. Neutron-induced secondary fission is handled automatically by the GEANT4 simulation using the standard "G4NeutronHPFission" class, and the fission neutrons are emitted isotropically. The ^{238}U(n,f) reaction cross section is approximately 100 mb over the range of neutron energies produced by the ^{238}U(γ,f) reaction[77], meaning that 0.5% of photofission neutrons will induce secondary fission. Neutron-induced fission is much less of an issue with the ^{232}Th target as the ^{232}Th(n,f) reaction cross section is approximately 1 mb over the range of neutron energies produced by the ^{232}Th(γ,f) reaction, resulting in a 0.005% chance that photofission neutrons will induce secondary fission.

The GEANT4 simulations used the photofission neutron generator described in section 7.4 which takes the fission neutrons from FREYA calculations and orients them so that the fission fragment axis matches an angular distribution $W(\theta, \phi)$ (Eqn. 7.4.1). The simulated neutron asymmetry in the INVS detector was fit using the function

$$Y(\phi) = a_d(1 + b_d \cos(2\phi)), \tag{8.4.1}$$

where a_d and b_d are fit parameters describing the overall neutron yield and the asymmetry produced by the γ-ray beam polarization, respectively. Here, $Y(\phi)$ gets its form from removing the θ angle dependence in $W(\theta, \phi)$, since the arrangement of the PCs in the INVS has no θ sensitivity. Using the results of the GEANT4 simulations, the relationship between the fragment asymmetry A_f and the detected neutron asymmetry b_d may be obtained. Fig. 8.17 shows the simulated photofission neutron asymmetries for ^{232}Th and ^{238}U as a function of the fission fragment asymmetry for the inner and outer rings of PCs in the INVS. All simulations were performed with $E_\gamma = 5.5$ MeV, because using photofission neutrons generated by different excitation energies had no effect on the detector asymmetry over the energy range probed in this work.

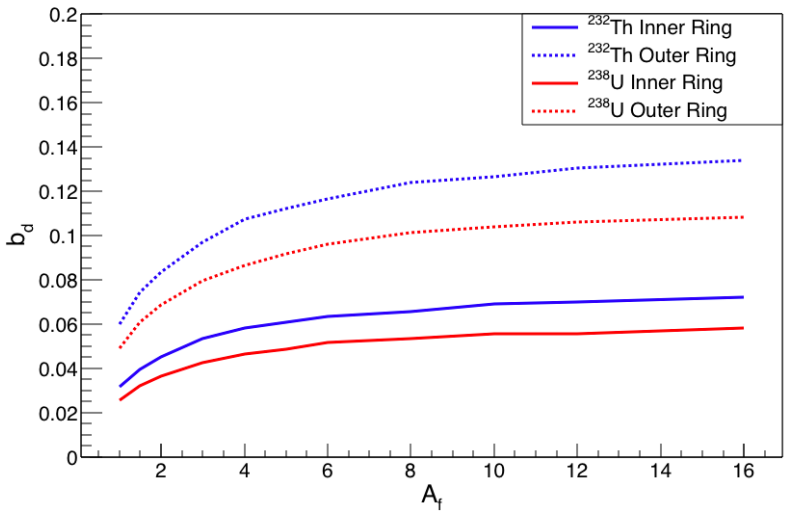

Figure 8.17: Simulated photofission neutron asymmetries in the INVS detector as a function of fragment asymmetry for the inner and outer detector rings.

8.5 Photofission Neutron Multiplicity Analysis

Multiplicity is a word with a multiplicity of meanings!

Ensslin *et al.*[106]

The goal of the present work is to determine the prompt photofission neutron multiplicities for ^{232}Th and ^{238}U, which are assumed to have a Gaussian distribution with a mean

$\overline{\nu}$ and a spread σ. However, what is experimentally measured is a *detected* neutron multiplicity distribution, which is entirely defined by the logic used to group individual neutrons detections into a single multiplicity event. The naive approach of using a 300 μs gate defined in section 8.3.4 works well for low event rates, where the probability of multiple reactions' occurring within the same gate is low. For a majority of the present work, the photofission rates are high enough that accidental coincidences become problematic and significantly impact the measured neutron multiplicities, in particular by creating falsely high multiplicity events where the real signal count rate is low. The effects of accidental coincidences are apparent in Fig. 8.18 which shows the detected neutron multiplicity distribution for the D(γ,n) reaction with the 300 μs gating scheme, at a total neutron detection rate of 445 Hz. The cosmic-ray neutron background has been subtracted, so the only source of neutrons is deuteron photodisintegration, which is a neutron multiplicity 1 event by definition. It is clear that an improved multiplicity logic scheme is necessary for analyzing the neutron multiplicities.

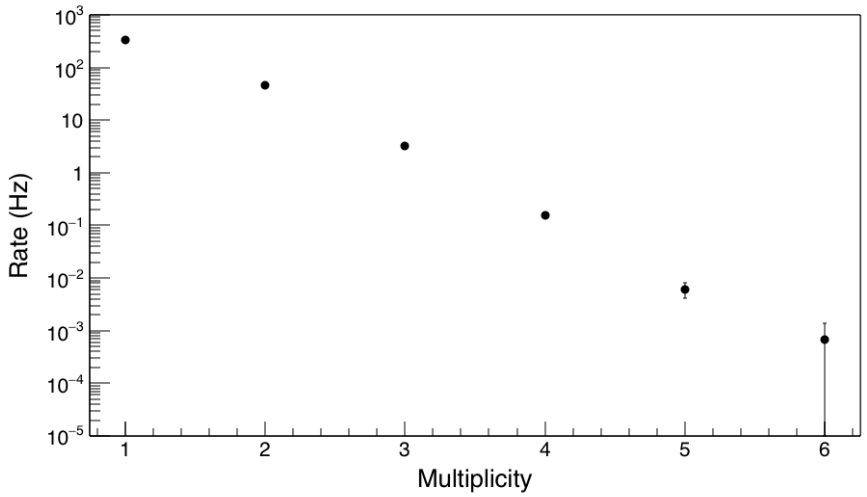

Figure 8.18: Detected neutron multiplicity distribution for the D(γ,n) reaction using 300 μs coincidence gates.

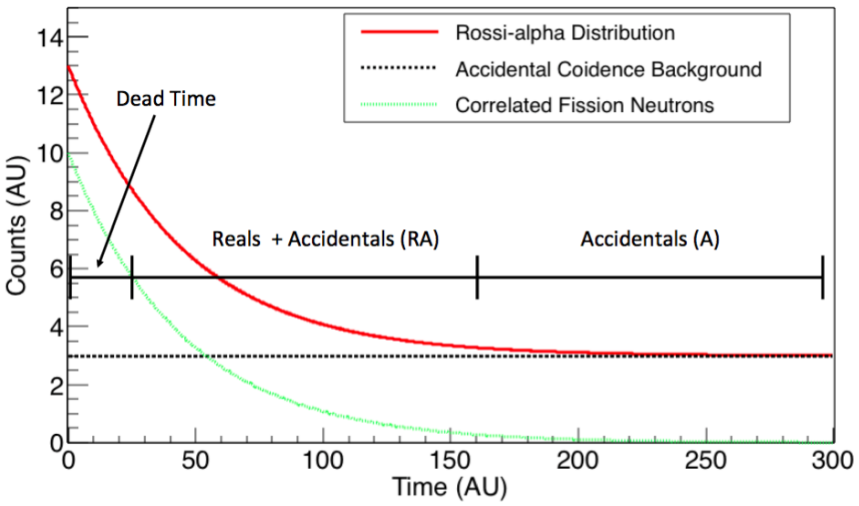

Figure 8.19: Rossi-alpha distribution with correlated and uncorrelated components and gates defining multiplicity regions.

8.5.1 Rossi-alpha Method

The detected neutron multiplicities in this work are defined by employing the Rossi-alpha method, a common multiplicity logic scheme which was originally developed for reactor neutron noise analysis[107]. Assuming that one could trigger a gate at the time of fission, the detected neutron time distribution would have the form

$$S(t) = A + Re^{-\lambda t}, \tag{8.5.1}$$

where $S(t)$ is the signal rate, A is the accidental background rate, R is the real signal from coincident fission neutrons, and λ is the detection decay constant associated with the neutron detector.

The distribution and its components are shown in Fig. 8.19, along with the time gates used to group neutrons into multiplicities. The RA gate contains neutrons from real coincidences as well as accidentals, while the A gate contains only accidentals. Additionally, a small delay is added between the initial trigger and the RA gate to account for a short dead time effect in the digitizer DAQ. Fig. 8.20 shows the time distribution of neutrons from the D(γ,n) reaction using the simple gating logic described in Fig. 8.2. There is a window with

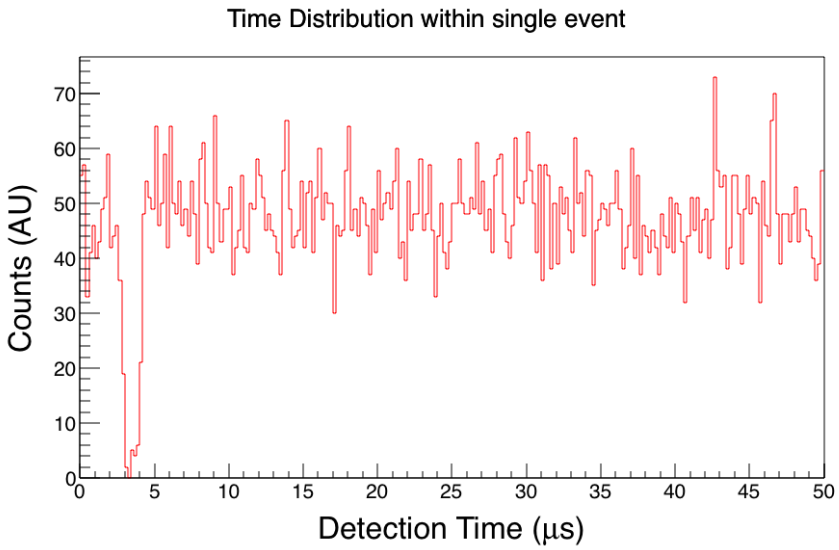

Figure 8.20: Detected neutron time distribution for the D(γ,n) reaction using 300 μs coincidence gate, with dead time between $3-4$ μs after the digitizer trigger.

no counts from $2.75-4.25$ μs after the first neutron trigger which defines the gate. This dead time results from the leading edge of the waveform of the coincident neutron's only being partially captured within the digitizer's acquisition window. If a pulse arrives too late in the data taking window, as in Fig. 8.21, the extracted pulse height and rise time values won't reflect the true shape of the waveform and it will be rejected by the PSD cut. A delay of 10 μs after the initial trigger prevents this dead time from impacting the overall efficiency within the RA gate, removing a potential systematic shift in multiplicity yields.

The Rossi-alpha gating logic is shown schematically in Fig. 8.22 as it was applied to analyzing the neutron detections in the INVS detector. Each neutron detection triggers an RA and A gate, and their multiplicities are recorded. Unlike the previous naive gating logic, here a neutron can be counted in several multiplicities in both the RA and A gates. Additionally the definition of multiplicity is changed. In the gating logic used for the background multiplicity analysis, a single neutron detection would result in an event with multiplicity=1. In the Rossi-alpha logic, that neutron would generate empty RA and A gates, which would both record multiplicity=0. By design this multiplicity analysis suppresses single, uncorrelated neutron events which is beneficial as the neutron backgrounds are typically $\sim 60\%$

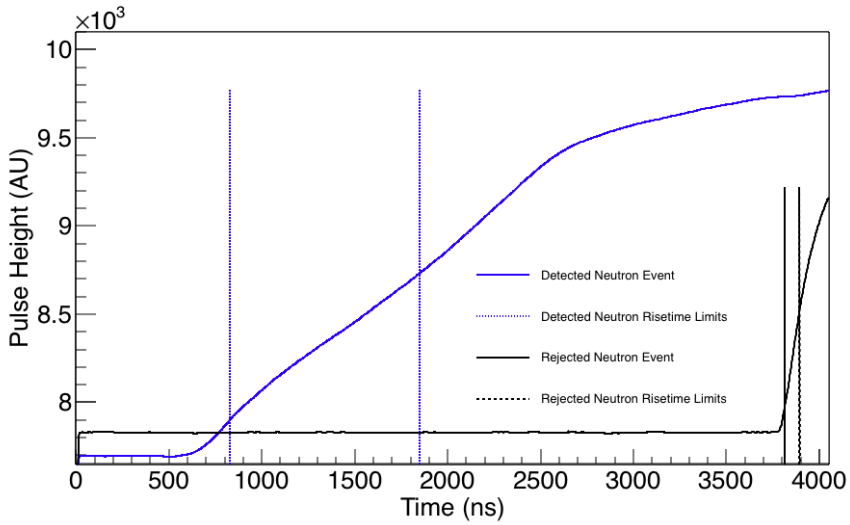

Figure 8.21: Example of a potential neutron pulse cut-off by the end of the digitizer gate, along with the coincident neutron pulse which triggered the gate.

single neutron events, with most of the remaining $\sim$ 40% of neutrons being grouped into multiplicity 2.

The detected multiplicity distribution from the Rossi-alpha analysis is given by subtracting the yield in the A gates from the RA gate yields for each multiplicity. An example is shown in Table 8.1 for a ^{238}U target with E_γ = 5.2 MeV. The Rossi-alpha multiplicity distribution for the D(γ,n) reaction is shown in Fig. 8.23. With the new multiplicity analysis the D(γ,n) reaction multiplicity distribution is consistent with 0 for all multiplicities except for 2 which may arise from the cosmic-ray neutron background.

Fig. 8.24 shows the measured $RA - A$ multiplicity distributions for ^{238}U and ^{232}Th targets, both of which have a significant number of higher multiplicity events from (γ,f) correlated neutrons. With the definition of detected neutron multiplicity settled, the next step is to determine the underlying photofission neutron multiplicities that would result in the detected multiplicities.

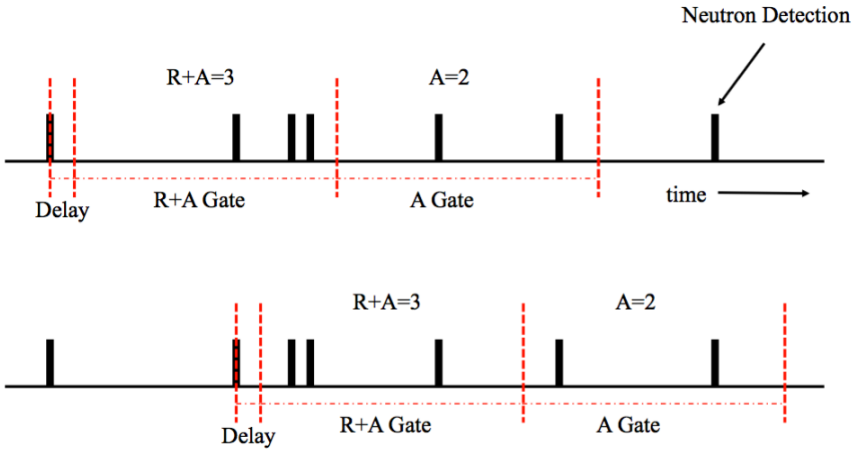

Figure 8.22: Schematic of Rossi-alpha method of multiplicity gating logic.

Multiplicity	RA	A	RA - A
0	74011	95098	-21087
1	24231	8867	15364
2	7300	3226	4074
3	1872	757	1115
4	481	131	350
5	143	38	105
6	59	5	54
7	20	6	14
8	11	1	10
9	2	1	1
10	0	0	0

Table 8.1: Measured RA, A and RA-A multiplicities for a ^{238}U target with $E_\gamma = 5.2$ MeV.

8.5.2 Monte Carlo Fitting of Photofission Neutron Multiplicities

Even with the Rossi-alpha multiplicity gating logic the detected neutron multiplicity distributions depend on the fission event rate and overlap with the background in a non-linear manner. Thus a Monte Carlo simulation is needed to reproduce the rate dependent effects and determine the underlying photofission prompt neutron multiplicity. A model was developed in which a particular fission neutron distribution is assumed, and then fission neutrons are generated and analyzed with the Rossi-alpha method. The resulting distribution is compared with the detected multiplicity distribution to determine the goodness of the fit.

A logic flow chart for the Monte Carlo simulation is shown in Fig. 8.25, and the steps

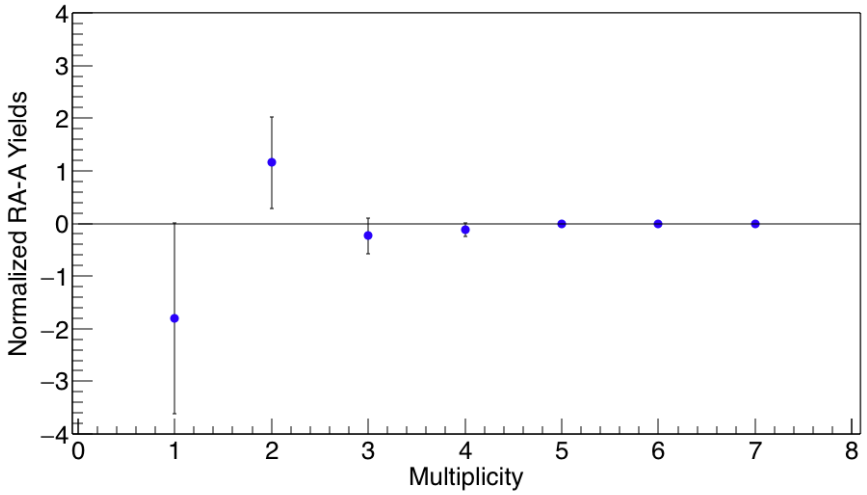

Figure 8.23: Measured Rossi-alpha multiplicity distribution for the D(γ,n) reaction at E_γ = 4.3 MeV.

are described in more detail below.

1. A guess at the photofission prompt neutron multiplicity is made using a Gaussian distribution with mean $\overline{\nu}$ and spread σ. The distribution is limited to physically allowed values of emitted neutrons, i.e. integer values greater than or equal to 0.

2. The total photofission rate, $R_{(\gamma,f)}$, for the run that is being modeled is determined using

$$R_{(\gamma,f)} = \frac{R_{INVS} - R_{background}}{\varepsilon_{INVS}\overline{\nu}}, \tag{8.5.2}$$

   where R_{INVS} is the INVS neutron detection rate, $R_{background}$ is the background neutron rate determined using the multiplicity fitting method described in section 8.3.4, and ε_{INVS} is the neutron detector efficiency for photofission neutrons determined by GEANT4 simulations.

3. A simulation time duration, τ_{sim}, is chosen and fission event times are selected randomly to fill that length of time, with the total number of fissions given by $R_{(\gamma,f)}\tau_{sim}$ so that the simulated fission rate matches the experimental data.

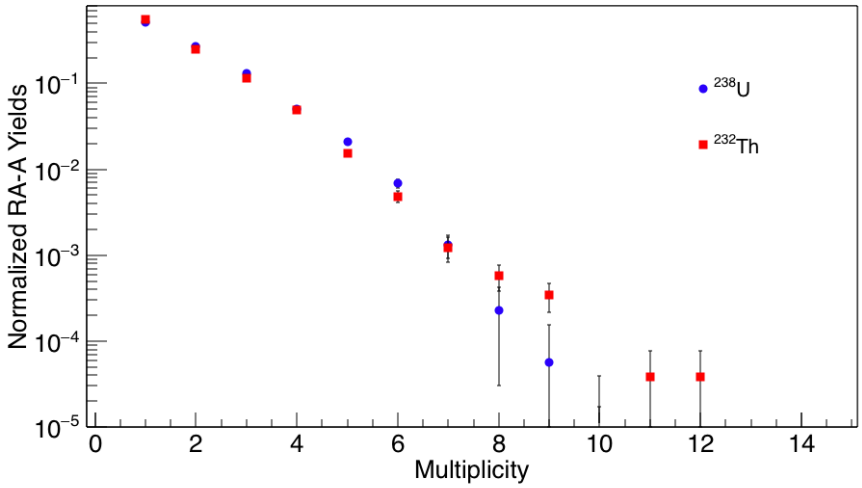

Figure 8.24: Measured Rossi-alpha multiplicity distributions for ^{238}U and ^{232}Th.

4. For each fission event the guessed multiplicity distribution is sampled to determine the number of neutrons emitted by the fission reaction.

5. Each neutron has a probability of being detected equal to ε_{INVS}.

6. If the neutron is detected, the detection time relative to the fission event is determined by sampling an exponential decay function with a half-life of 31 μs.

7. Once the list of detected fission neutrons is fully generated, background neutrons are added by inserting the multiplicity distributions determined in section 8.3.4 using the simple 300 μs gating logic. Unlike the photofission neutrons in the simulation, no attempt is made to guess the underlying multiplicity distribution. Instead the number of multiplicity (1, 2, 3, etc.) events are added to the Monte Carlo simulation so that the simulated rates of each multiplicity match the experimental values.

8. For each background neutron, a detection time relative to the start of the background event is chosen by sampling an exponential decay function with a 31 μs half life. Background neutrons are limited to being detected within 300 μs of the background event start time.

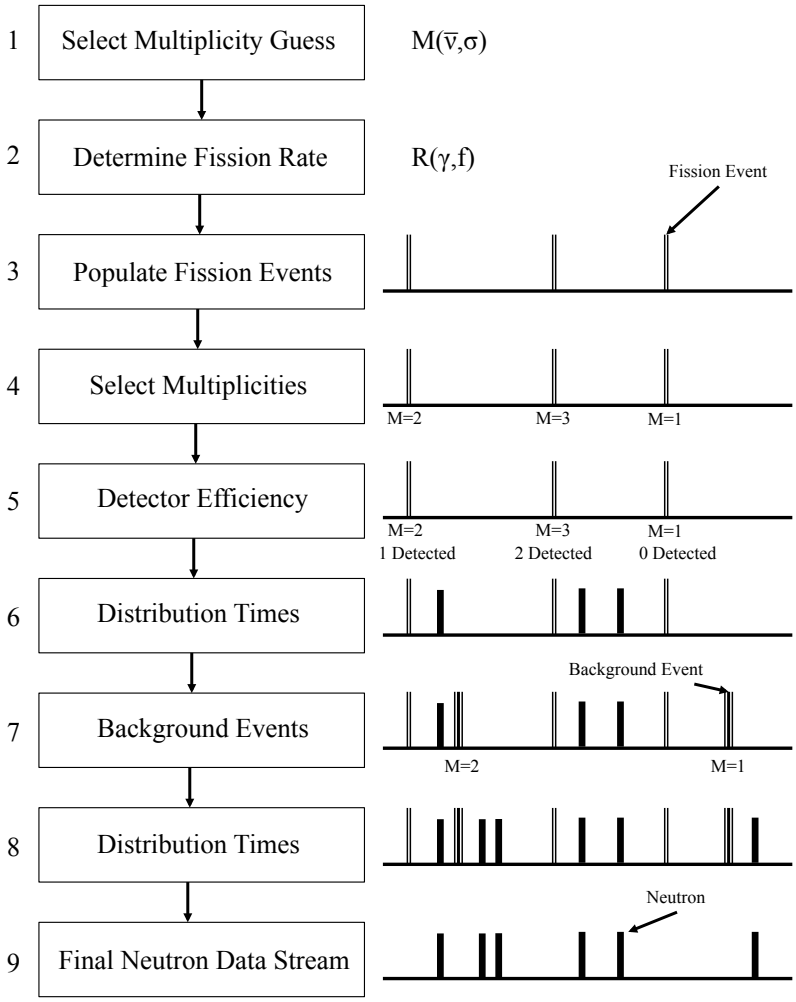

Figure 8.25: Monte Carlo simulation logic for generating neutron timestamps.

9. After all fission and background neutrons are simulated, the list of detected neutrons is saved and sorted chronologically to produce a data stream equivalent to what is measured experimentally.

The neutrons produced by the Monte Carlo technique are analyzed using the same Rossi-alpha method as the measured data, and the resulting multiplicity rates are compared with

the experimental values. The goodness of fit is given by the χ^2 value, defined as

$$\chi^2 = \sum_{m=1}^{6} \left(\frac{D_m - S_m}{\sigma_m} \right)^2, \tag{8.5.3}$$

where m is the multiplicity, D_m is the rate of that multiplicity from the experimental data, S_m is the rate of that multiplicity from the Monte Carlo simulation, and σ_m is the statistical uncertainty of the experimental multiplicity rate. A maximum multiplicity of 6 was chosen since higher order multiplicities suffered from statistical fluctuations in the simulations and would have required orders of magnitude longer simulation times. The simulation was run for multiplicity distributions with a range of $\overline{\nu}$ and σ with the goal of minimizing the χ^2. After finding the multiplicity distribution with the smallest χ^2 value, the errors for $\overline{\nu}$ and σ were determined by the change in value needed to increase the χ^2 by 1. The contour plot for the χ^2 fit of ^{238}U(γ,f) with E_γ = 5.6 MeV is shown in Fig. 8.26, with the contour lines given in increments of χ^2=1 above the minimum value of $\chi^2 = 5.3$.

8.6 Photofission Cross Section Analysis

Compared with the multiplicity and asymmetry analyses, the photofission cross section analysis is straightforward. The cross section $\sigma(\gamma,\mathrm{f})$ is written as

$$\sigma(\gamma, f) = \frac{(N_n - N_b)A_t}{\varepsilon_{INVS}\overline{\nu}N_\gamma \ell_t \rho_t f N_A}, \tag{8.6.1}$$

where N_n is the total number of detected neutrons, N_b is the number of background neutrons, A_t is the mass number of the target material, ε_{INVS} is the efficiency of the INVS detector, $\overline{\nu}$ is the mean prompt neutron multiplicity, N_γ is the total number of γ-rays on target, ℓ_t is the target thickness, ρ_t is the target density, f is the thick target correction factor and N_A is Avogadro's number. The thick target correction accounts for the reduction of the γ-ray

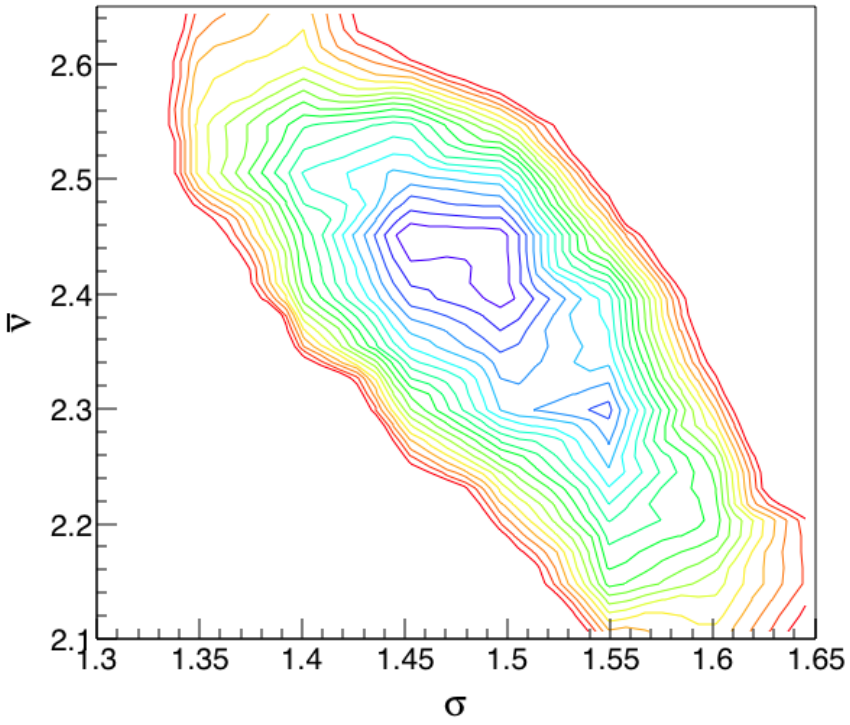

Figure 8.26: Contour plot of the χ^2 value for the Monte Carlo simulated neutron multiplicities compared with the measured multiplicities for the ^{238}U(γ,f) reaction with E_γ = 5.6 MeV, as a function of the photofission multiplicity distribution parameters $\overline{\nu}$ and σ. The contour lines are given in increments of χ^2=1 above the minimum value of χ^2 = 5.3.

beam flux caused by attenuation within the target and is given by

$$f = \frac{1 - e^{-\mu\rho_t\ell_t}}{\mu\rho_t\ell_t}, \tag{8.6.2}$$

where μ is the energy dependent attenuation coefficient for the target material[86]. The neutron background rates come from the analysis in section 8.3.4 and the γ-ray count rate comes from the scintillating paddle flux monitor described in section 5.4. The value of $\overline{\nu}$ is determined from the results of the multiplicity measurements which will be given in section 9.3. The photofission neutron spectra from the FREYA simulations did not differ enough over the range of 4.3 $<E_\gamma <$ 6.3 MeV to change the simulated efficiency of the INVS. Thus, $\varepsilon_{INVS} = 0.295 \pm 0.009$ for ^{232}Th(γ,f) neutrons and $\varepsilon_{INVS} = 0.277 \pm 0.008$ for

^{238}U(γ,f) neutrons, where both efficiencies include interactions within the target material and target holder. The systematic error in the photofission cross sections is dominated by the contribution from ε_{INVS}, and is consequently about 3%.

CHAPTER 9: RESULTS & DISCUSSION

9.1 Introduction

The experimental results of the ^{232}Th and ^{238}U measurements are presented in this chapter along with a discussion of how the present work fits into the landscape of existing photofission data. The prompt photofission neutron polarization asymmetries are covered in section 9.2, the photofission neutron multiplicities are discussed in section 9.3 and the photofission cross sections are explored in section 9.4. The implications of the present work on the structure of the ^{232}Th and ^{238}U fission barriers will also be discussed. Finally concluding remarks on the present results and potential future work will be given. The data presented in this chapter may also be found in tabulated form in appendix B.

9.2 Prompt Photofission Neutron Polarization Asymmetries

The detected photofission neutron asymmetries were fit using the method described in section 8.4.2 to extract the detector asymmetry parameter b_d, defined by equation 8.4.1. Fig. 9.1 shows the detected asymmetries for ^{232}Th and ^{238}U for both the inner and outer INVS detector rings. As confirmed with the GEANT4 simulations, the asymmetry in the outer ring is much greater than that of the inner ring because the outer ring is more sensitive to the higher energy neutrons which have greater asymmetries. Measurements where the fission cross sections dropped below ~ 1 μb where the background neutron yields were comparable to the fission neutron yields are not included because there were not enough statistics to produce reliable fits.

The underlying prompt photofission neutron asymmetries were extracted from the detected asymmetries using the simulation results from sections 7.4 and 8.4.2. The asymmetry

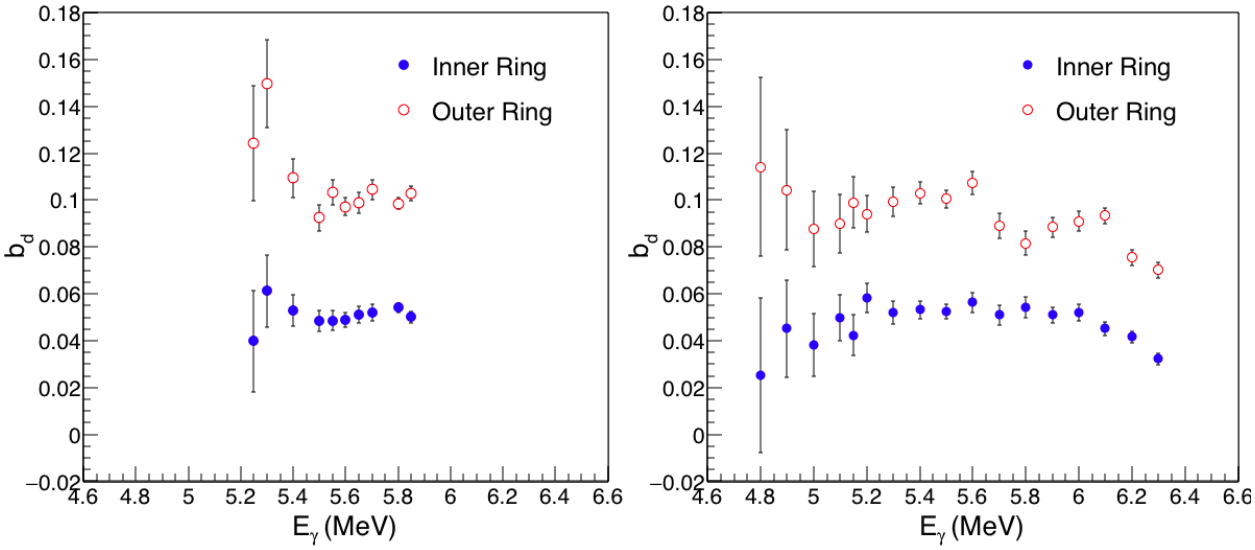

(a) ^{232}Th (b) ^{238}U

Figure 9.1: Detected asymmetry parameter b_d for photofission neutrons, with error bars defined by the uncertainty in the fits.

may be given by a single parameter A_n defined by

$$A_n = \frac{b_n}{a_n}, \tag{9.2.1}$$

where a_n and b_n are given by the neutron angular distribution

$$W_n(\theta, \phi) = \frac{1}{a_n + 2b_n} \left(a_n + b_n \sin^2(\theta) + b_n \cos(2\phi) \sin^2(\theta) \right), \tag{9.2.2}$$

which follows the form of equation 7.4.1. Recall that a_n and b_n are normalized by

$$a_n + b_n = 1. \tag{9.2.3}$$

The prompt photofission neutron asymmetries A_n for ^{232}Th and ^{238}U are shown in Fig. 9.2 for the inner and outer INVS rings. Once the effects of the detector response are accounted for, the asymmetries detected by each ring are in good agreement.

Each ring of the INVS detector provides an independent measurement of the neutron

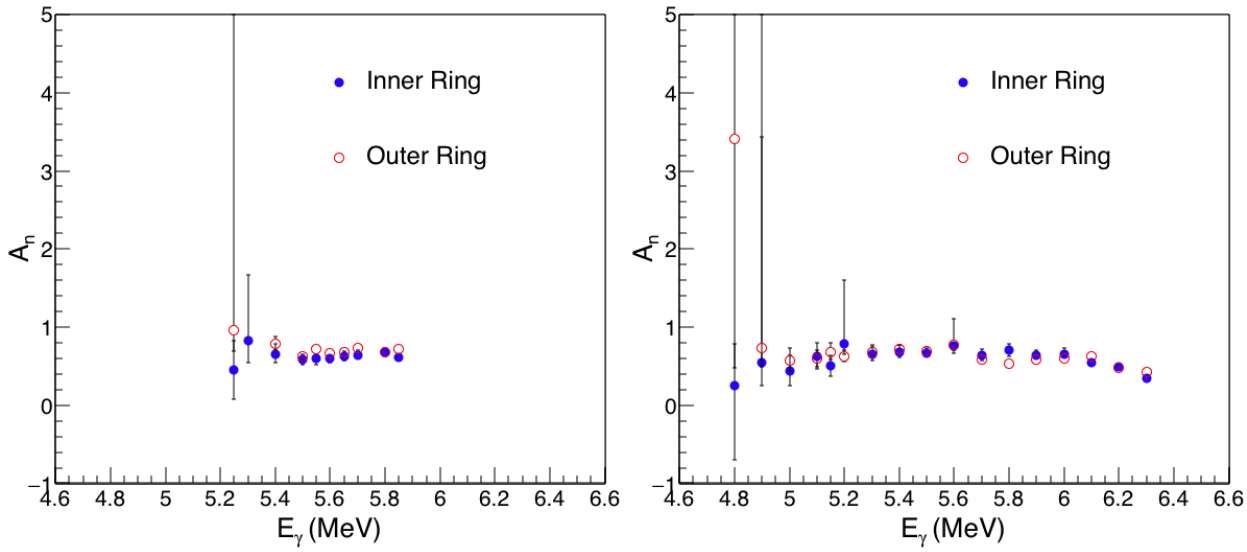

(a) ^{232}Th (b) ^{238}U

Figure 9.2: Detected asymmetry parameter A_n for photofission neutrons. The error bars reflect the uncertainty of the fits.

asymmetries, so a single value of A_n was produced by averaging the results of the inner and outer rings and summing their uncertainties in quadrature. Finally, a polarization asymmetry $\Sigma_n(\theta)$ may be defined in terms of the neutron yields in the planes parallel and perpendicular to the γ-ray beam polarization axis. The prompt fission neutron polarization asymmetry $\Sigma_n(90°)$ is defined by

$$\Sigma_n(\theta) = \frac{W(\theta,\phi=0) + W(\theta,\phi=180) - W(\theta,\phi=90) - W(\theta,\phi=270)}{W(\theta,\phi=0) + W(\theta,\phi=180) + W(\theta,\phi=90) + W(\theta,\phi=270)} \tag{9.2.4}$$

evaluated at $\theta = 90°$, which is equivalent to

$$\Sigma_n(90°) = \frac{A_n}{1+A_n}. \tag{9.2.5}$$

The polarization asymmetry from the combined inner and outer rings is shown in Fig. 9.3 for ^{232}Th and ^{238}U. Both isotopes exhibit large asymmetries, equivalent to roughly 2.5 neutrons emitted in the plane of γ-ray beam polarization for every 1 neutron emitted perpendicular

to the polarization. The ^{232}Th polarization asymmetry remains constant over the measured E_γ range, while the ^{238}U asymmetry decreases significantly above $E_\gamma = 6$ MeV.

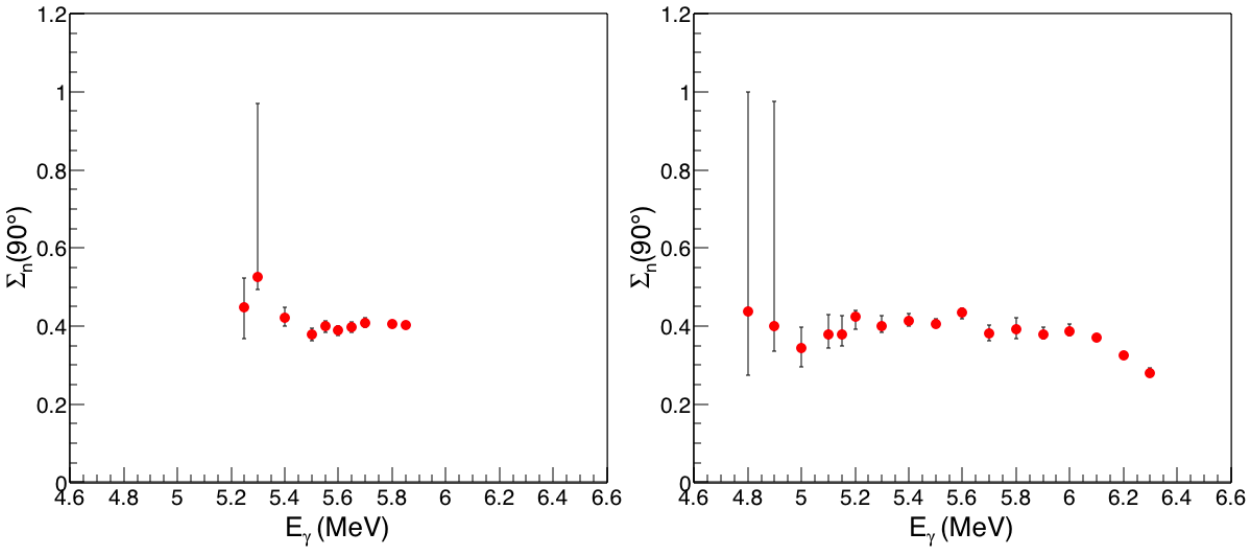

(a) ^{232}Th (b) ^{238}U

Figure 9.3: Detected polarization asymmetry for photofission neutrons. The error bars reflect the uncertainty of the fits.

These results are consistent with the expected effects of the transmission through the fission barrier. Recall that ^{232}Th and ^{238}U are even-even nuclei with $J^\pi = 0^+$ ground states. As discussed in section 3.1, the low energy photoabsorption interaction is dominated by the E1 excitation, which through selection rules can only connect the 0^+ ground state with a 1^- excited state in the potential well. This means that fission can only proceed through the (J^π, K) channels of $(1^-, 0)$ and $(1^-, \pm 1)$, where the $K = 0$ state has an asymmetry $\Sigma_n(90°) = 1$ and the $K = \pm 1$ states have $\Sigma_n(90°) = -1$ (as shown in Table 3.1).

Based on the the most likely energy level ordering for an even-even nucleus[34] (shown in Fig. 3.1), the lowest energy 1^- excitation is $(1^-, 0)$ which corresponds to the mass asymmetry mode. This would then be the dominant fission channel at low energy E_γ and would result in large polarization asymmetries. The next lowest channel would be the $(1^-, \pm 1)$ bending mode which would begin to contribute as E_γ is increased, reducing the polarization asymmetry, as experimentally observed.

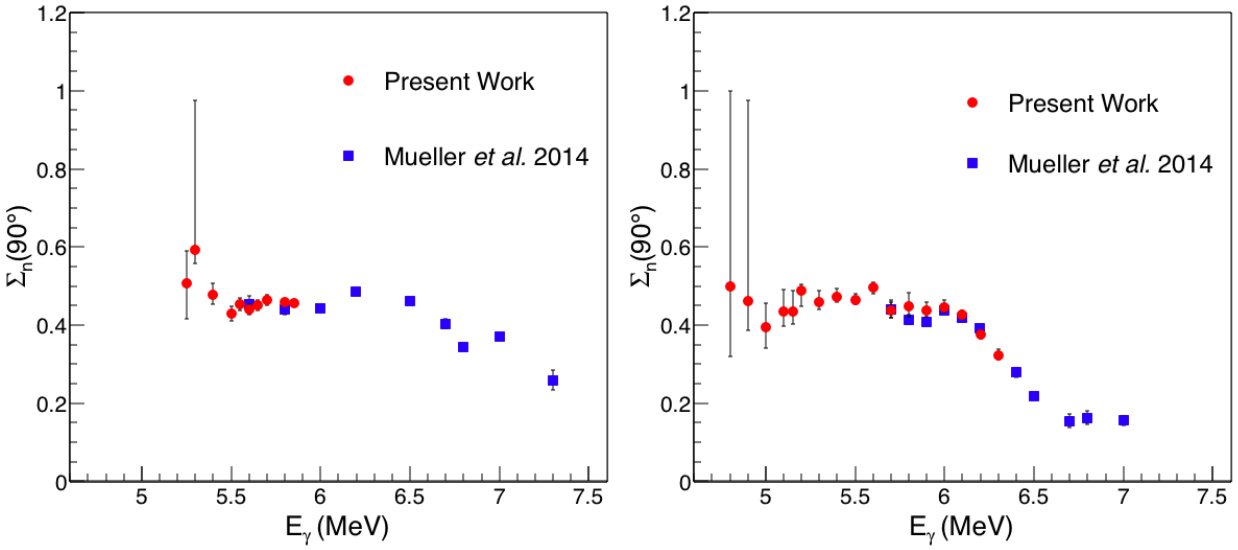

(a) ^{232}Th (b) ^{238}U

Figure 9.4: Comparison of Σ_n for $E_n > 1.5$ MeV with previous data[14].

The results of the present work are compared with the only existing previous measurement by Mueller *et al.*[14] of prompt photofission polarization asymmetries in Fig. 9.4, with good agreement observed between both sets of data. The previous measurement using a neutron TOF technique only includes neutrons with energy above 1.5 MeV because of the detection limitations of the liquid scintillator detectors.

In order to make a direct comparison, the present asymmetries were adjusted to include only neutrons above 1.5 MeV. This adjustment was achieved by setting a 1.5 MeV energy threshold on the neutron distribution fit which correlates the fission fragment asymmetry with the emitted neutron asymmetry. The effect of the neutron energy threshold on the relationship between the fission fragment asymmetry and the neutron asymmetry is shown in Fig. 7.8. As discussed in section 3.4 and calculated in section 7.4 the higher energy fission neutrons are expected to have a greater polarization asymmetry. Incorporating a 1.5 MeV neutron energy threshold increased the polarization asymmetries by about 10%.

The present work represents the lowest E_γ prompt photofission neutron polarization measurements for ^{232}Th and ^{238}U, and is one of only two such measurements ever made.

There are no observed changes in the polarization asymmetries measured in the present experiment which would indicate the existence of additional, low energy states from a third minimum in the fission barrier.

9.3 Prompt Photofission Neutron Multiplicities

The prompt photofission neutron multiplicity distributions for ^{232}Th and ^{238}U were fit using the Monte Carlo method described in section 8.5.2. As with the polarization asymmetries, fits could not be performed for $E_\gamma < 5.3$ MeV measurements where the photofission cross sections were low. Additionally, the ^{238}U multiplicity fits were limited to a maximum E_γ of 5.8 MeV because above that energy the high energy tail of the HIγS γ-ray beam crossed the ^{238}U(γ,n) reaction threshold of 6.15 MeV. This limit is lower than the 6 MeV cutoff imposed on the photofission analysis because the presence of an uncharacterized background arising from the (γ,n) reaction significantly impacts the multiplicity distribution fitting, even for a low rate of photoneutrons.

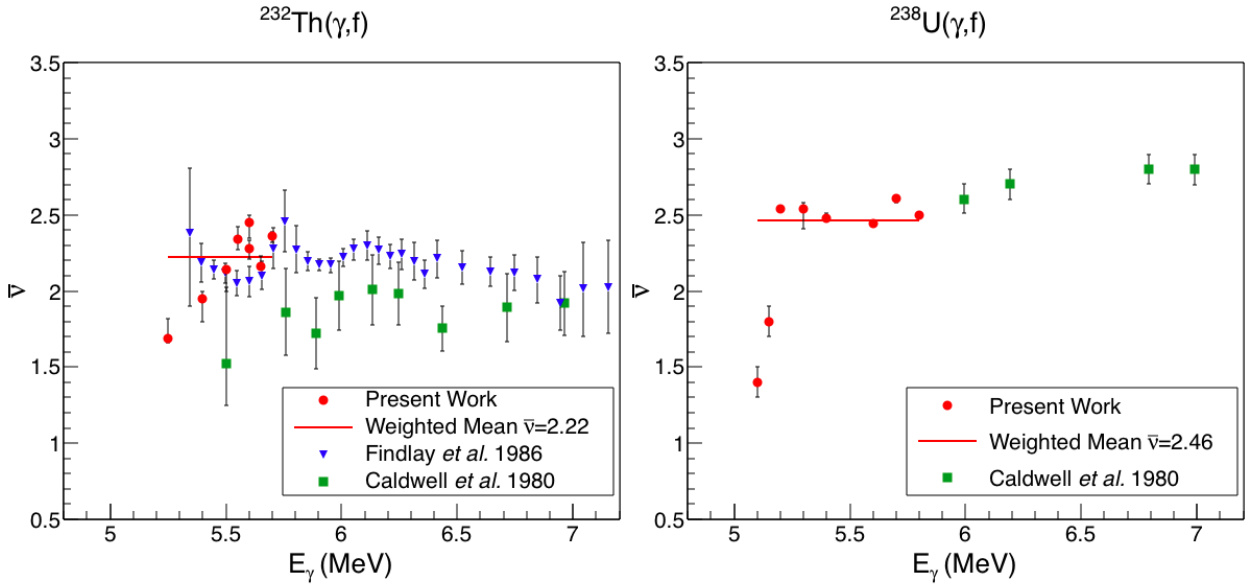

(a) ^{232}Th (b) ^{238}U

Figure 9.5: Mean photofission neutron multiplicities determined in the present work compared with previous data[71][61].

The mean prompt photofission neutron multiplicities, $\overline{\nu}$, for ^{232}Th and ^{238}U are shown in Fig. 9.5, along with the previous measurements by Caldwell *et al.*[71] and Findlay *et al.*[61]. The error bars in the present data represent the range of values that increase the χ^2 of the fit by less than 1. A weighted mean of the present data was calculated using the inverse of the χ^2 as the weight. The weighted mean is thus given by

$$\overline{\nu}_{mean} = \frac{\Sigma_i \frac{\overline{\nu}_i}{\chi_i^2}}{\Sigma_i \frac{1}{\chi_i^2}}, \tag{9.3.1}$$

where χ^2 is defined by equation 8.5.3 and describes the goodness of fit of $\overline{\nu}$. Multiplicities determined in the present work were $\overline{\nu}_{mean} = 2.22$ for the photofission of ^{232}Th, and $\overline{\nu}_{mean} = 2.46$ for the photofission of ^{238}U. The lowest E_γ points which diverge from the rest of the data suffer from poor statistics and consequently have larger χ^2 values. exceeding 200 for the lowest E_γ ^{232}Th measurement and 50 for the lowest E_γ ^{238}U measurement. The full results are tabulated in section B.2.

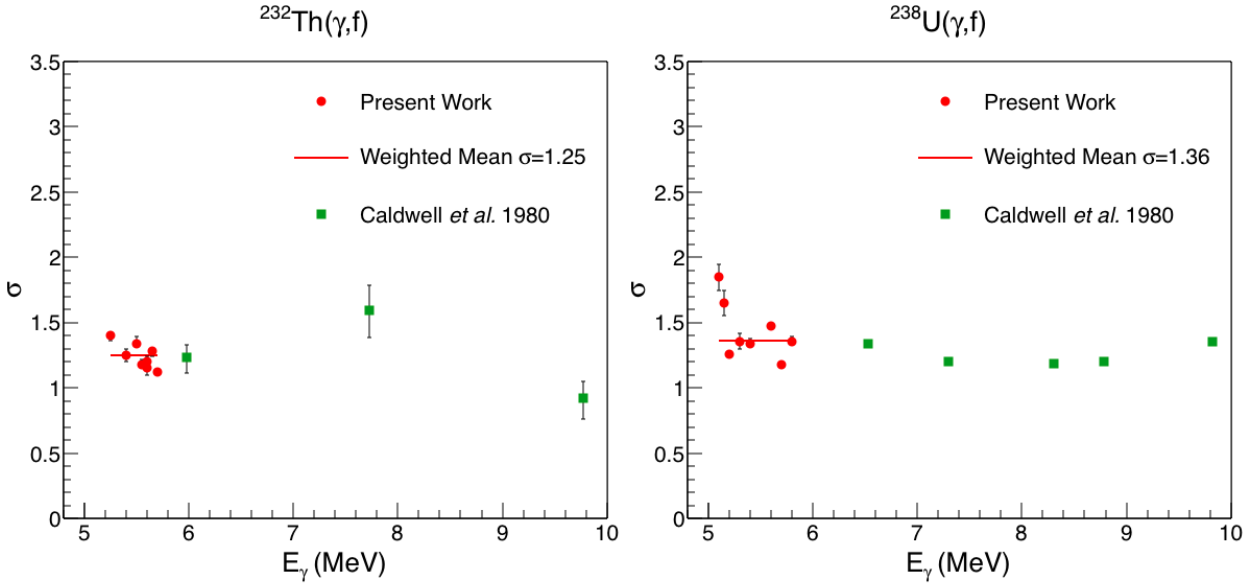

(a) ^{232}Th. (b) ^{238}U.

Figure 9.6: Photofission neutron multiplicity spreads compared with previous data[71].

The spreads σ of the prompt neutron multiplicity distributions were also determined

through the Monte Carlo fit and are plotted in Fig. 9.6 along with the previous measurements of Ref. [71]. The weighted mean σ_{mean} was calculated using equation 9.3.1 and, consistent with the previous measurements, with $\sigma_{mean} = 1.25$ for the ^{232}Th(γ,f) reaction and $\sigma_{mean} = 1.36$ for the ^{238}U(γ,f) reaction. The present work represents the lowest E_γ measurements of the prompt photofission neutron multiplicities and spreads for ^{232}Th and ^{238}U, and the lowest energy measurements of photofission neutron multiplicities for any isotope.

As discussed in section 3.4, the prompt fission neutron multiplicities are sensitive to many fission observables such as the fragment excitation energy, mass and kinetic energy distributions. The agreement between the present $\overline{\nu}$ and σ and the previous measurements is consistent with the fission mechanism's remaining unchanged at these new, sub-barrier excitation energies. There is no evidence in the present data of any exotic forms of fission or new fission channels contributing to the fission yields.

9.4 Photofission Cross Sections

9.4.1 Photofission of ^{232}Th

The photofission cross sections for ^{232}Th were determined using the analysis method described in section 8.6. The total neutron production cross section is plotted in Fig. 9.7, spanning a range from 2 mb down to 600 nb. The vertical error bars correspond to the statistical uncertainty and a 2% systematic error is not shown. The horizontal error bars represent the 3% FWHM energy resolution of the γ-ray beam.

The ^{232}Th(γ,f) reaction cross section is plotted in Fig. 9.8 along with the previous measurements. The present data are generally in good agreement, with the present work sampling the marked spread of energy ranges when compared with the previous measurements. This work represents the first quasi-monoenergetic photofission measurement with ^{232}Th in the sub-barrier E_γ range, as the previous two measurements[61][52] shown were made using bremsstrahlung γ-ray beams. The agreement in the observed cross sections validates the unfolding and normalization techniques used by the previous measurements to

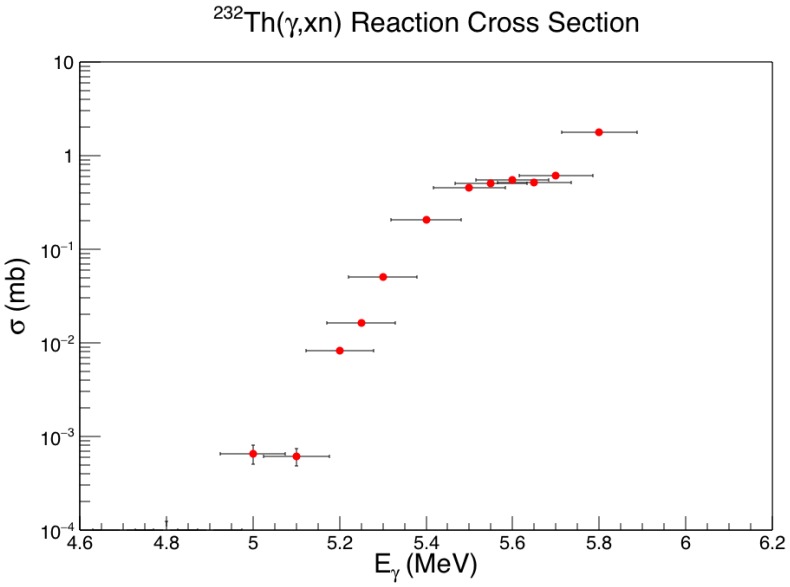

Figure 9.7: Total photoneutron production cross section for ^{232}Th. The horizontal error bars represent the 3% FWHM energy resolution of the γ-ray beam.

extract the photofission cross sections from the integrated bremsstrahlung beam yields.

In particular the present work observes the same plateau in the photofission cross section of ^{232}Th in the E_γ range of 5.4-5.7 MeV. Blokhin and Soldatov[62] attribute this plateau to an almost complete fragmentation of a resonance in the second minimum caused by damping, and a partial fragmentation of a resonance in the third minimum which is shifted in energy relative to the second minimum resonance. This combination of resonant states in the second and third minima explains the large width of the plateau and the fact that it is structured. These resonances and the resulting photofission cross section plateau are shown in Fig. 4.2.

The one significant deviation between the present data and previous measurements is the suppression of the resonance at 5.6 MeV, with a factor of 1.6 between the present work and the data of Smirenkin and Soldatov[52]. The data of Findlay *et al.*[61] varies significantly in this E_γ region but still appears to observe the resonance. Additionally the 5.6 MeV peak was observed by a tagged-photon measurement[64] with a 0.2% spread, so the resonance is not likely to be an artifact of unfolding the bremsstrahlung spectra. The cause of this discrepancy between the present work and previous measurements is unknown, however the 5.6 MeV resonance is reproduced in both double- and triple-humped barrier calculations so

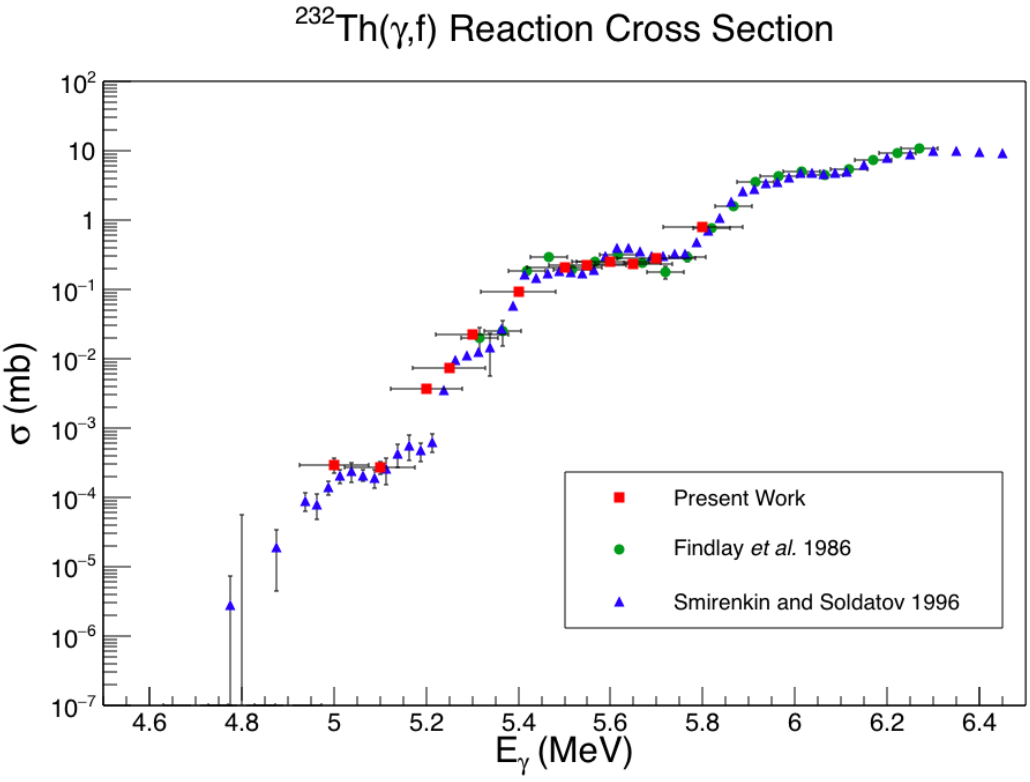

Figure 9.8: Present ^{232}Th(γ,f) cross section compared with previous measurements by Findlay *et al.*[61] and Smirenkin and Soldatov[52]. The vertical error bars represent the statistical uncertainties and the horizontal error bars represent the energy resolution. The present work has a resolution of 3% FWHM (150 keV at 5 MeV), Findlay *et al.* have an 80 keV resolution and Smirenkin and Soldatov have a 12 keV resolution. The previous measurements both were made with bremsstrahlung beams, so the energy resolution represents the unfolded spectrum resolution.

it does not impact the fission barrier shape interpretation.

Given the generally good agreement between the present work and the work of Smirenkin and Soldatov[52], the present measurements are consistent with the triple-humped ^{232}Th fission barrier interpretation that was fit to the previous data[62]. The inferred fission barrier, shown in Fig. 9.10, has a 1.8 MeV deep third minimum, in disagreement with all modern theoretical calculations of the fission barrier which predict a shallow minimum of less than 0.5 MeV[29][26][28]. The discrepancy between theoretical calculations and measurements of the ^{232}Th fission barrier remains unresolved, and this work adds to the growing list of experimental measurements of features in the ^{232}Th photofission cross section which are consistent with a triple-humped fission barrier.

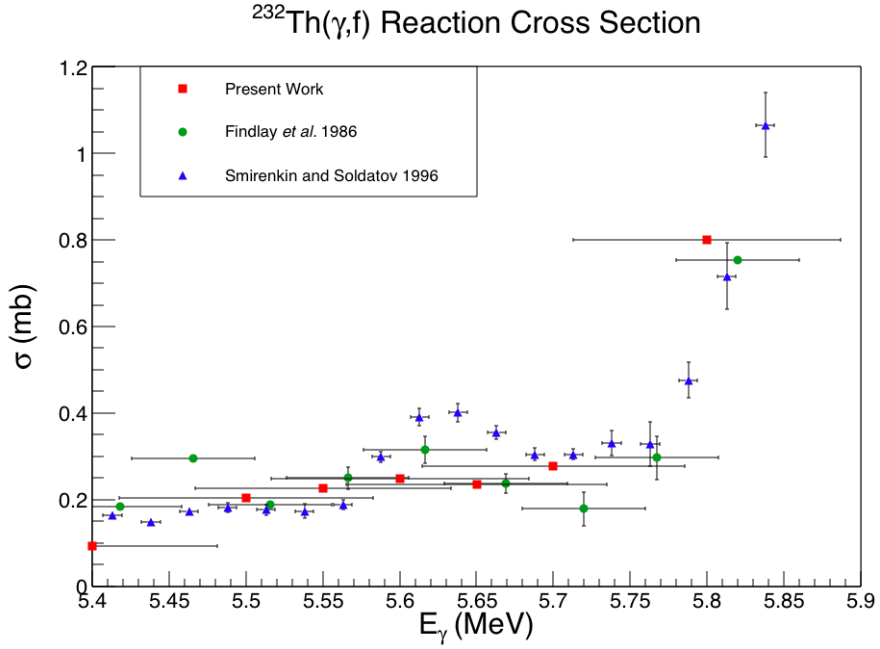

Figure 9.9: A portion of the data from Fig. 9.8, in a linear scale.

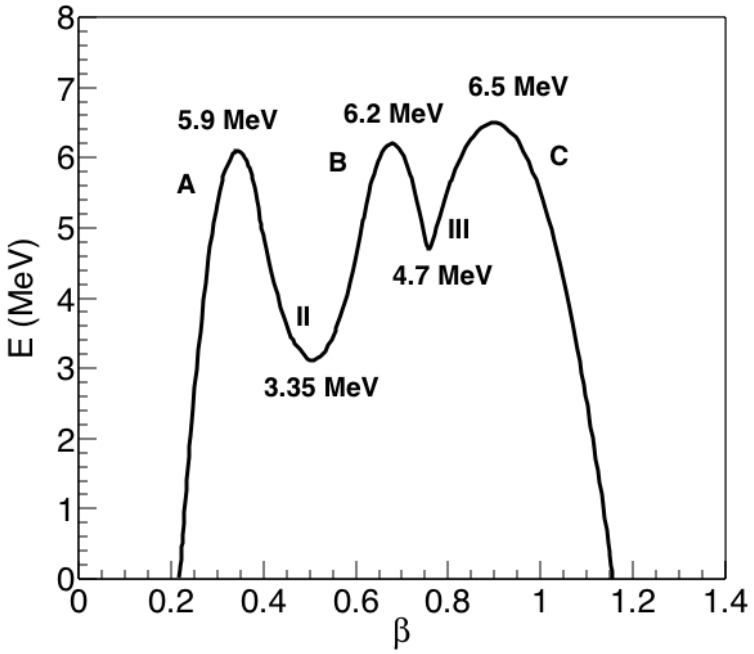

Figure 9.10: ^{232}Th fission barrier fit by Blokhin and Soldatov[62] to the data of Smirenkin and Soldatov[52]. The barrier heights are $E_A = 5.9$ MeV, $E_B = 6.2$ MeV and $E_C = 6.5$ MeV; the barrier depths are $E_{II} = 3.35$ MeV and $E_{III} = 4.7$ MeV; and the barrier curvatures are $\hbar\omega_A = 1.3$ MeV, $\bar{\omega}_B = 1.1$ MeV, $\hbar\omega_C = 0.65$ MeV, $\hbar\omega_{II} = 0.45$ MeV and $\hbar\omega_{III} = 2.6$ MeV.

9.4.2 Photofission of ^{238}U

The total photoneutron production cross section for ^{238}U is shown in figure 9.11. The cross section calculation assumes the neutron detection efficiency ε_{INVS} which was simulated for neutrons from the ^{238}U(γ,f) reaction, so the contributions of neutrons originating from the ^{238}U(γ,n) reaction in the measurements above E_γ = 6 MeV are overrepresented. In reality the neutron detector efficiency is much higher for the neutrons from the (γ,n) reaction, since near threshold they are much lower in energy than the photofission neutrons. However, as discussed in section 8.3.5 the (γ,n) reaction contribution near threshold is difficult to quantify because of uncertainty in the shape of the cross section. Consequently these data points will not be included in the photofission cross section analysis.

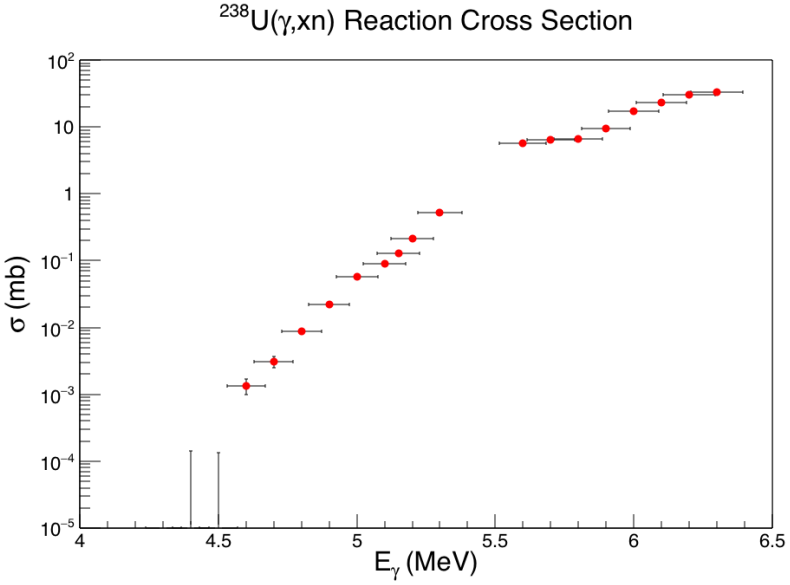

Figure 9.11: Total photoneutron cross section for ^{238}U measured in the present work. Neutrons are produced by the (γ,f) reaction for most of the data, with an increasing contribution from the (γ,n) reaction for measurements above 5.9 MeV.

The ^{238}U(γ,f) reaction cross section was determined by dividing the ^{238}U(γ,xn) reaction cross section by the experimentally determined neutron multiplicity $\overline{\nu}$ = 2.46. The results are shown in Fig. 9.12 along with previous measurements. The present ^{238}U(γ,f) reaction cross section spans a range of over 6 orders of magnitude, from 7 mb down to 600 nb. The calculated photofission cross sections for double- and triple-humped fission barriers from fits

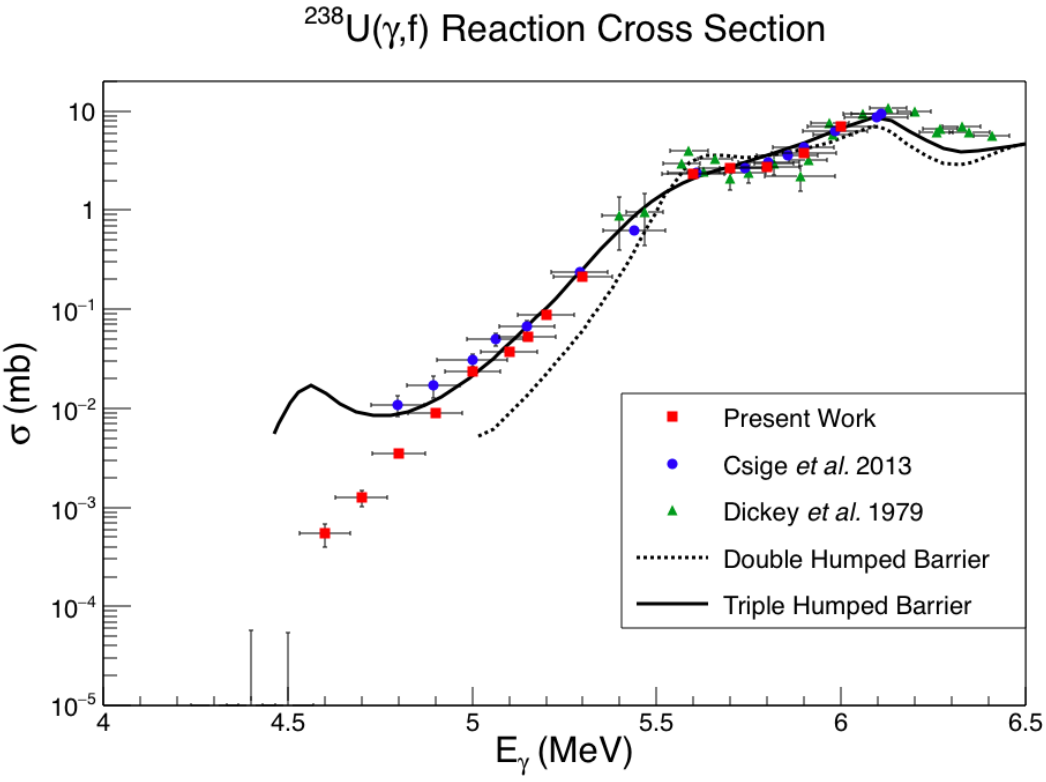

Figure 9.12: Present ^{238}U(γ,f) reaction cross section data compared with the previous measurements by Dickey *et al.*[56] and Csige *et al.*[13]. Also shown are the calculated photofission cross sections from double- and triple-humped fission barriers fit to Csige *et al.*[13].

to previous data[13] are also shown. Above $E_\gamma = 5.2$ MeV the present work agrees with the previous measurements, as shown in Fig. 9.13, but below $E_\gamma = 5.2$ MeV the present work diverges from Csige *et al.*[13] by up to a factor of 3. Additionally, there is no sign of the expected resonance[13] at 4.6 MeV in the present measurement.

The data of Csige *et al.*[13] was also measured at HIγS, using the same γ-ray beams as the present work. Csige *et al.* used a different technique for measuring the photofission cross section by the fission fragments, as discussed in section 4.2.2. This means that the bremsstrahlung beam contamination which was measured for the first time in this work (see section 8.3.4) would have also been present during the previous measurement, and could potentially have created false signs of a low energy photofission resonance. While the primary HIγS γ-ray beam probes the $\sim \mu$b sub-barrier photofission cross section, the bremsstrahlung γ-ray spectrum includes the GDR region of $10-20$ MeV where the photofission cross section

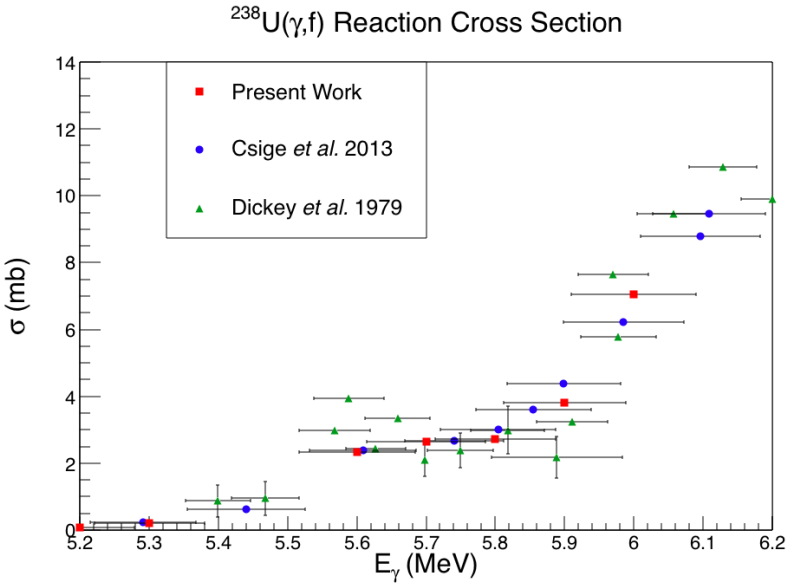

Figure 9.13: A portion of the data from Fig. 9.12 in a linear scale.

is nearly 200 mb. The bremsstrahlung-induced photofission background rate will then be much larger than the sub-barrier photofission signal rate. Furthermore, as shown in Fig. 8.12, the relative rate of the events caused by bremsstrahlung contamination to the primary HIγS γ-ray beam increases with decreasing E_γ, meaning that the relative observed 'background cross section' will increase at lower energies. This increasing photofission rate mimics the signal expected from a low energy resonance in the photofission cross section.

This explanation is validated by adding the measured bremsstrahlung-induced background neutrons back into the present data and reanalyzing the ^{238}U(γ,f) reaction cross section, as shown in Fig. 9.14. With the background caused by bremsstrahlung added back, the present data are in agreement with the previous measurement of Csige *et al.*[13]. This agreement is consistent with the bremsstrahlung beam contamination being present in the Csige *et al.*[13] measurement. Since the signs of a low energy resonance in the Csige *et al.*[13] ^{238}U(γ,f) reaction cross section are likely a previously unaccounted-for accelerator-induced background, there no longer exists any experimental evidence of a third minimum in the ^{238}U fission barrier. The present work is consistent with a double-humped fission barrier interpretation, as shown in Fig. 9.15.

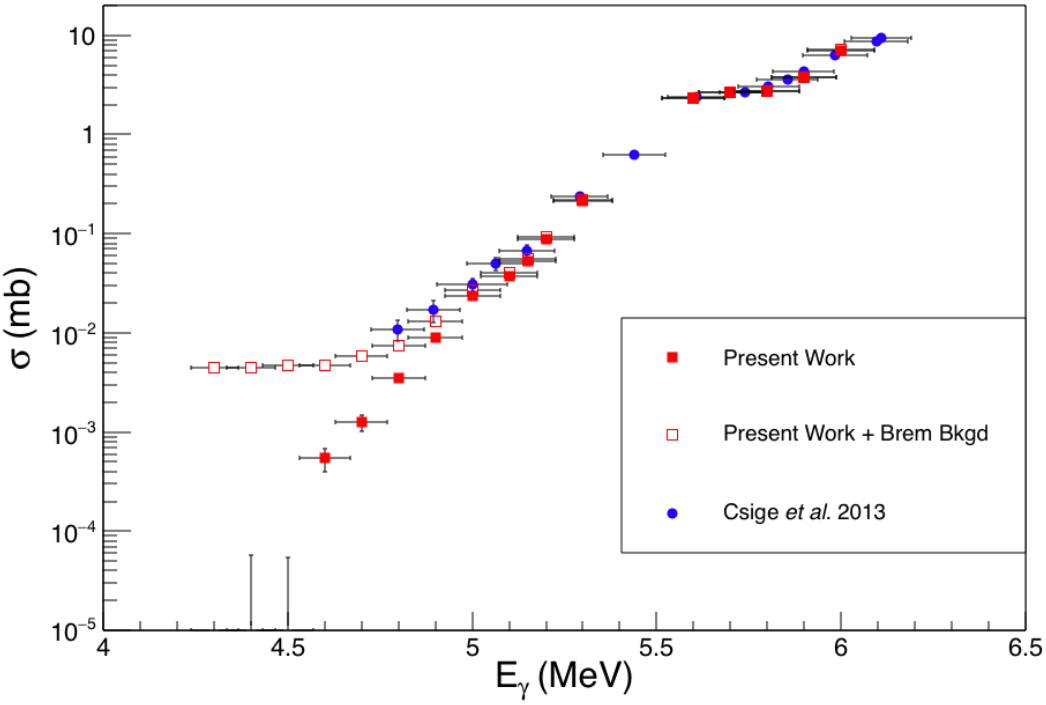

Figure 9.14: Comparison between the present ^{238}U(γ,f) reaction data with and without the accelerator-induced bremsstrahlung background neutrons and Csige *et al.*[13]. The inclusion of the bremsstrahlung beam induced neutrons in the present data results in agreement with the previous measurement.

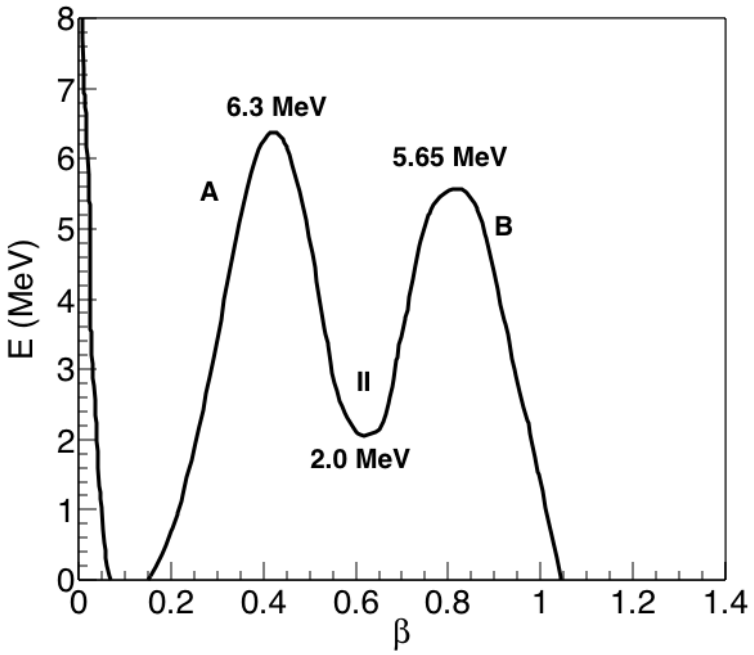

Figure 9.15: ^{238}U fission barrier fit by Csige *et al.*[13], assuming a double-humped barrier structure. The barrier heights are $E_A = 6.3 \pm 0.2$ MeV and $E_B = 5.65 \pm 0.2$ MeV; the barrier depth is $E_{II} = 2.0 \pm 0.2$ MeV; and the barrier curvatures are $\hbar\omega_A = 1.1 \pm 0.1$ MeV, $\bar{\omega}_B = 0.6 \pm 0.1$ MeV and $\hbar\omega_{II} = 1.0 \pm 0.1$ MeV.

9.5 Concluding Remarks

This work was performed at the HIγS facility operated by TUNL, where 100% linearly polarized, quasi-monoenergetic γ-ray beams were used to induce fission in the two targets and the prompt photofission neutrons were detected. A ^{3}He proportional counter-based neutron detector was significantly upgraded and thoroughly characterized to allow for the detection of polarization asymmetries and neutron multiplicities.

This work represents the lowest energy photofission measurements in ^{232}Th and ^{238}U, probing the photofission neutron multiplicities, prompt neutron polarization asymmetries and photofission cross sections. The photofission cross sections were measured down to 300 nb and 500 nb for ^{232}Th and ^{238}U, respectively, measuring the ^{238}U(γ,f) reaction cross section at the lowest energy ever. The photofission neutron polarization asymmetry measurements extend previous work at $E_\gamma > 5.6$ MeV done at HIγS[14] by reproducing the already measured asymmetries and extending the data range down to lower energies which have never been probed before. The mean photofission neutron multiplicities and spreads were measured at the lowest energies to date.

Using a multiplicity analysis technique made possible by the detector upgrade, a bremsstrahlung beam contamination of the HIγS γ-ray beam was measured for the first time. This accelerator-induced background has been identified as the cause of a false signal in a previous measurement which had incorrectly predicted a third minimum in the ^{238}U fission barrier. The present results are consistent with a double-humped ^{238}U fission barrier and a triple-humped ^{232}Th fission barrier. A deep third minimum in the ^{232}Th barrier is not predicted by theoretical calculations, and it remains to be understood why the state of the art theoretical models are inconsistent with experimental data.

The inferred fission barrier structure for ^{238}U could be further refined by determining the barrier structure which best reproduces the newly measured ^{238}U(γ,f) reaction cross section. Using using the same approach as Csige *et al.*[13], the photofission cross section can be calculated with the EMPIRE statistical model code for a particular fission barrier structure.

The barrier parameters can then be tuned to reproduce the measured ^{238}U(γ,f) reaction cross section as closely as possible. The resulting improved ^{238}U fission barrier structure would provide more accurate data for modern theoretical nuclear models to reproduce.

The structure of the fission barriers may be further constrained by future photofission measurements. The bremsstrahlung beam background at HIγS will limit the sensitivity of photofission measurements to about what was achieved in this work. To measure lower cross sections the bremsstrahlung component of the incident beam will need to be mitigated or characterized more thoroughly. However, the beam tune dependence of the bremsstrahlung may make a high precision characterization intractable. A proposed upgrade to the HIγS facility[108] using an external laser source and directing the electron beam in the FEL storage ring at a slight angle relative to the γ-ray beam axis is a promising solution, as it would direct the electron-beam-produced bremsstrahlung away from the γ-ray beam path.

The inferred ^{232}Th fission barrier[62] predicts resonances below E_γ = 5 MeV. These resonances could potentially be observed using γ-ray beams provided by the ELI-NP facility presently under construction in Bucharest, which will have roughly 2 orders of magnitude more flux than the current HIγS beam. The γ-ray beams to be produced by ELI-NP will also have finer resolution, 0.5% compared with 3% at HIγS, which would give better resolution of the fine structure in the photofission cross section from resonances. Photofission cross section measurements constitute one of the major components of the ELI-NP research plan.

The recent development of laser-wakefield based γ-ray sources has raised the prospect of performing active interrogation with portable linearly-polarized γ-ray sources[11]. A group at the University of Nebraska, Lincoln have developed a novel γ-ray source which generates polarized γ-ray beams through inverse-Compton scattering laser photons off of energetic, laser-wakefield driven electron beams. In collaboration with the author, they demonstrated the production of 9 MeV γ-ray beams[12]. Thus, γ-ray beams produced by such a source can induce photofission on shielded SNM, and the fission neutrons can escape high density shielding to be detected. The results of the present work indicate that large polarization

asymmetries are observed in photofission neutrons from ^{232}Th and ^{238}U at E_γ well below the fission barrier. At these low energies there are virtually no background neutrons because E_γ is below the neutron separation energy for most nuclei, so photofission neutrons are a sensitive probe for the presence of SNM. Additionally, the neutron polarization asymmetry gives information about the isotopic composition of the SNM. Previous measurements at higher E_γ have demonstrated the ability to detect the enrichment of U through the detected photofission neutron polarization asymmetries[109]. The present results suggest the technique is also valid for lower energy γ-ray beams, which would be easier to produce in realistic scenarios.

APPENDIX A: DEUTERIUM PHOTODISINTEGRATION KINEMATICS

Using the formalism of Schreiber *et al.*[89], the cross section for neutron emission by D(γ,n) for a circularly polarized γ-ray beam can be written as

$$\sigma(\theta_{COM}) = \frac{\lambda^2}{48\pi}\Big[|S|^2 + \frac{27}{2}|P|^2 \sin^2\theta_{COM}\Big], \tag{A.0.1}$$

where λ is the wavelength of the γ-ray, and $|S|^2$ and $|P|^2$ are the M1 (s wave) and E1 (p wave) strengths respectively. The energy dependent E1 and M1 strengths for this work come from theoretical calculations by Tornow *et al.*[90]. After a neutron emission angle θ_{COM} is selected it is boosted into the lab frame. The invariant energy of the system is given by

$$W = \sqrt{(E_\gamma + m_d c^2)^2 - E_\gamma^2}, \tag{A.0.2}$$

where E_γ is the energy of the incident γ-ray and m_d is the mass of the deuteron. The momentum of the neutron (or proton) in the COM frame is then

$$p_n = \frac{\sqrt{(W^2 - (m_p c^2 - m_n c^2)^2)(W^2 - (m_p c^2 + m_n c^2)^2)}}{2W}, \tag{A.0.3}$$

where m_n and m_p are the masses of the neutron and proton respectively. In the laboratory frame the component of the momentum parallel to the relative motion of the COM frame, $p_{||}^{COM}$, is determined by the appropriate Lorentz transformation

$$\begin{aligned} p_{||}^{LAB} &= \gamma_f \beta_f E_n^{COM} + \gamma_f p_{||}^{COM}, \\ \gamma_f &= \frac{E_\gamma + m_d c^2}{W}, \\ \beta_f &= \frac{E_\gamma}{E_\gamma + m_d c^2}, \end{aligned} \tag{A.0.4}$$

where γ_f is the Lorentz factor and β_f is the velocity of the COM frame. The component of p_n perpendicular to the relative motion of the COM frame is unaffected by the transformation

to the laboratory frame. The angle of neutron emission in the lab relative to the γ-ray beam axis, θ_{LAB}, can be written as

$$\theta_{LAB} = atan\left(\frac{p_n \sin\theta_{COM}}{\gamma_f \beta_f \sqrt{(m_n c^2)^2 + p_n^2} + \gamma_f p_n \cos\theta_{COM}}\right). \tag{A.0.5}$$

From Wattenberg [110] [111] the energy of an outgoing neutron from D(γ,n) in the lab frame, E_n, is given by

$$E_n = \frac{A-1}{A}\left(E_\gamma - Q - \frac{E_\gamma^2}{1862(A-1)}\right) + E_\gamma cos\theta\sqrt{\frac{2(E_\gamma - Q)}{931A^3}}, \tag{A.0.6}$$

where A is the mass of the target nucleus (2) and Q is the Q-value of the reaction (2.2246 MeV).

APPENDIX B: TABULATED RESULTS

B.1 Prompt Photofission Neutron Polarization Asymmetry Data

$E_\gamma(MeV)$	σ_{E_γ} (MeV)	b_d Inner Ring	b_d Outer Ring	$\Sigma_n(90^\circ)$
5.25	0.079	0.040±0.02	0.12±0.02	$0.51\pm^{0.08}_{0.09}$
5.3	0.080	0.06±0.02	0.15±0.02	$0.6\pm^{0.4}_{0.04}$
5.4	0.081	0.053±0.007	0.109±0.008	$0.48\pm^{0.03}_{0.02}$
5.5	0.083	0.049±0.005	0.0925±0.006	$0.43\pm^{0.02}_{0.02}$
5.55	0.083	0.049±0.004	0.103±0.005	$0.45\pm^{0.02}_{0.02}$
5.6	0.084	0.049±0.003	0.097±0.004	$0.44\pm^{0.01}_{0.01}$
5.65	0.085	0.051±0.004	0.099±0.004	$0.45\pm^{0.01}_{0.01}$
5.7	0.086	0.052±0.003	0.105±0.004	$0.46\pm^{0.01}_{0.01}$
5.8	0.087	0.054±0.002	0.099±0.003	$0.458\pm^{0.009}_{0.008}$
5.85	0.088	0.050±0.003	0.103±0.003	$0.456\pm^{0.009}_{0.01}$

Table B.1: Tabulated ^{232}Th(γ,f) reaction asymmetry data. $\pm\sigma_{E_\gamma}$ gives error bars which represent the FWHM of the γ-ray beam spectrum.

$E_\gamma(MeV)$	σ_{E_γ} (MeV)	b_d Inner Ring	b_d Outer Ring	$\Sigma_n(90^\circ)$
4.8	0.072	0.03±0.03	0.11±0.04	$0.4\pm^{0.6}_{0.2}$
4.9	0.074	0.05±0.02	0.10±0.03	$0.4\pm^{0.6}_{0.06}$
5	0.075	0.04±0.01	0.088±0.02	$0.34\ \pm^{0.06}_{0.05}$
5.1	0.077	0.050±0.009	0.09±0.01	$0.38\pm^{0.05}_{0.03}$
5.15	0.077	0.042±0.009	0.10±0.01	$0.38\pm^{0.05}_{0.03}$
5.2	0.078	0.0584±0.006	0.094±0.008	$0.43\pm^{0.01}_{0.03}$
5.3	0.080	0.052±0.005	0.0993±0.006	$0.40\pm^{0.03}_{0.02}$
5.4	0.081	0.053±0.004	0.103±0.005	$0.41\pm^{0.02}_{0.01}$
5.5	0.083	0.053±0.003	0.100±0.004	$0.40\pm^{0.01}_{0.01}$
5.6	0.084	0.056±0.004	0.107±0.005	$0.43\pm^{0.01}_{0.02}$
5.7	0.086	0.051±0.004	0.0889±0.005	$0.38\pm^{0.02}_{0.02}$
5.8	0.087	0.054±0.004	0.0817±0.005	$0.39\pm^{0.03}_{0.02}$
5.9	0.089	0.051±0.003	0.0884±0.004	$0.38\pm^{0.02}_{0.01}$
6	0.09	0.0520±0.003	0.0910±0.004	$0.39\pm^{0.02}_{0.01}$
6.1	0.092	0.045±0.003	0.0933±0.003	$0.37\pm^{0.01}_{0.01}$
6.2	0.093	0.042±0.002	0.0755±0.003	$0.33\pm^{0.01}_{0.01}$
6.3	0.095	0.032±0.002	0.070±0.003	$0.28\pm^{0.01}_{0.01}$

Table B.2: Tabulated ^{238}U(γ,f) reaction asymmetry results. $\pm\sigma_{E_\gamma}$ gives error bars which represent the FWHM of the γ-ray beam spectrum.

B.2 Prompt Photofission Neutron Multiplicity Data

$E_\gamma(MeV)$	$\overline{\nu}$	σ	χ^2
5.25	$1.69\pm^{0.13}_{0.03}$	$1.4\pm^{0.03}_{0.04}$	41.0
5.4	$1.95\pm^{0.05}_{0.15}$	$1.25\pm^{0.05}_{0.05}$	2.69
5.5	$2.14\pm^{0.02}_{0.14}$	$1.34\pm^{0.05}_{0.02}$	0.141
5.55	$2.34\pm^{0.08}_{0.07}$	$1.18\pm^{0.04}_{0.03}$	1.78
5.6	$2.45\pm^{0.05}_{0.1}$	$1.15\pm^{0.05}_{0.05}$	1.60
5.6	$2.28\pm^{0.05}_{0.07}$	$1.2\pm^{0.04}_{0.03}$	0.520
5.65	$2.16\pm^{0.07}_{0.02}$	$1.28\pm^{0.02}_{0.04}$	0.223
5.7	$2.36\pm^{0.03}_{0.04}$	$1.12\pm^{0.02}_{0.02}$	0.245

Table B.3: Tabulated ^{232}Th photofission prompt neutron multiplicity data. The uncertainties for $\overline{\nu}$ and σ represent the variation of the parameter which changes the χ^2 value by 1.

$E_\gamma(MeV)$	$\overline{\nu}$	σ	χ^2
5.1	$1.4\pm^{0.1}_{0.1}$	$1.85\pm^{0.1}_{0.1}$	8.58
5.15	$1.8\pm^{0.1}_{0.1}$	$1.65\pm^{0.1}_{0.1}$	4.08
5.2	$2.54\pm^{0.02}_{0.02}$	$1.26\pm^{0.02}_{0.02}$	3.77
5.3	$2.54\pm^{0.04}_{0.13}$	$1.35\pm^{0.07}_{0.05}$	0.812
5.4	$2.48\pm^{0.03}_{0.02}$	$1.34\pm^{0.04}_{0.02}$	0.661
5.6	$2.44\pm^{0.02}_{0.02}$	$1.47\pm^{0.02}_{0.02}$	0.886
5.7	$2.61\pm^{0.02}_{0.03}$	$1.18\pm^{0.02}_{0.02}$	1.07
5.8	$2.5\pm^{0.02}_{0.02}$	$1.35\pm^{0.04}_{0.02}$	1.54

Table B.4: Tabulated ^{238}U photofission prompt neutron multiplicity data. The uncertainties for $\overline{\nu}$ and σ represent the variation of the parameter which changes the χ^2 value by 1.

B.3 Photofission and Photoneutron Cross Section Data

$E_\gamma(MeV)$	σ_{E_γ} (MeV)	$\sigma(\gamma,xn)$ (mb)	$\sigma(\gamma,f)$ (mb)
4.7	0.071	-0.0009±0.0005	-0.0004±0.0002
4.8	0.072	-0.0001±0.0002	-0.00004±0.0001
4.9	0.074	-0.0009±0.0002	-0.0004±0.0001
5	0.075	0.0007±0.0002	0.00030±0.00007
5.1	0.077	0.0006±0.0001	0.00027±0.00006
5.2	0.078	0.0083±0.0002	0.00373±0.00009
5.25	0.079	0.0165±0.0003	0.0074±0.0002
5.3	0.080	0.0504±0.0005	0.0227±0.0002
5.4	0.081	0.2063±0.0008	0.0929±0.0003
5.5	0.083	0.452±0.001	0.2038±0.0005
5.55	0.083	0.505±0.001	0.2273±0.0005
5.6	0.084	0.550±0.001	0.2480±0.0005
5.65	0.085	0.522±0.001	0.2351±0.0005
5.7	0.089	0.615±0.001	0.2771±0.0005
5.8	0.087	1.774±0.006	0.799±0.003

Table B.5: Tabulated ^{232}Th photofission data. $\pm\sigma_{E_\gamma}$ gives error bars which represent the FWHM of the γ-ray beam spectrum.

$E_\gamma(MeV)$	σ_{E_γ} (MeV)	$\sigma(\gamma,xn)$	$\sigma(\gamma,f)$
4.3	0.065	-0.0008±0.0005	-0.0003±0.0002
4.4	0.066	-0.0002±0.0003	-0.00008±0.0001
4.5	0.068	-0.0002±0.0003	-0.00006±0.0001
4.6	0.069	0.0013±0.0004	0.0005±0.0001
4.7	0.071	0.0031±0.0006	0.0012±0.0002
4.8	0.072	0.0087±0.0006	0.0035±0.0002
4.9	0.074	0.0219±0.0007	0.0089±0.0003
5	0.075	0.0574±0.0006	0.0233±0.0002
5.1	0.077	0.0910±0.0005	0.0370±0.0002
5.15	0.077	0.1296±0.0006	0.0527±0.0002
5.2	0.078	0.2165±0.0007	0.0880±0.0003
5.3	0.080	0.530±0.001	0.2156±0.0006
5.6	0.084	5.73±0.01	2.330±0.005
5.7	0.086	6.49±0.01	2.639±0.006
5.8	0.087	6.70±0.01	2.722±0.006
5.9	0.089	9.34±0.02	3.798±0.007
6.0	0.09	17.38±0.03	7.06±0.01
6.1	0.09	23.39±0.03	
6.2	0.09	29.92±0.04	
6.3	0.09	33.32±0.04	

Table B.6: Tabulated ^{238}U photofission data. $\pm\sigma_{E_\gamma}$ gives error bars which represent the FWHM of the γ-ray beam spectrum. The photofission cross section is not evaluated for E$\gamma > 6$ MeV due to the presence of background neutrons from the ^{238}U(γ,n) reaction.

BIBLIOGRAPHY

[1] O. Hahn and F. Strassmann. Über den nachweis und das verhalten der bei der bestrahlung des urans mittels neutronen entstehenden erdalkalimetalle. *Naturwissenschaften*, 27(1):11–15, 1939.

[2] L. Meitner and O.R. Frisch. Products of the Fission of the Uranium Nucleus. *Nature*, 143:471 – 472, 1939.

[3] Energy, Electricity and Nuclear Power Estimates for the Period up to 2050. Technical Report 1, International Atomic Energy Agency, Vienna, 2015.

[4] R. Vandenbosch and J.R. Huizenga, editors. *Nuclear Fission*. Academic Press, 1973.

[5] Y. Oganessian. Heaviest Nuclei From ^{48}Ca-induced Reactions. *Journal of Physics G: Nuclear and Particle Physics*, 34(4):R165, 2007.

[6] A. Staszczak, A. Baran, and W. Nazarewicz. Spontaneous Fission Modes and Lifetimes of Superheavy Elements in the Nuclear Density Functional Theory. *Phys. Rev. C*, 87:024320, Feb 2013.

[7] Scientific Grand Challenges: Forefront Questions in Nuclear Science and the Role of Computing at the Extreme Scale. Technical report, D.O.E. Office of Nuclear Physics, 2009.

[8] Thorium Fuel Cycle - Potential Benefits and Challenges. Technical report, International Atomic Energy Agency, Vienna, 2005. IAEA-TECDOC-1450.

[9] Safety Margins of Operating Reactors. Technical report, International Atomic Energy Agency, Vienna, 2003. IAEA-TECDOC-1332.

[10] J.D. McDonnell, N. Schunck, D. Higdon, J. Sarich, S.M. Wild, and W. Nazarewicz. Uncertainty Quantification for Nuclear Density Functional Theory and Information Content of New Measurements. *Phys. Rev. Lett.*, 114:122501, Mar 2015.

[11] J. Silano, H.J. Karwowski, S. Clarke, S. Pozzi, S. Banerjee, D. Haden, G. Golovin, S. Chen, I. Ghebregziabher, C. Liu, C. Petersen, J. Zhang, N. Powers, B. Zhao, K. Brown, J. Mills, and D. Umstadter. Selective Activation with All-laser-driven Thomson γ-rays. In *2013 IEEE International Conference on Technologies for Homeland Security, HST 2013*, pages 429–434, 2013.

[12] C. Liu, G. Golovin, S. Chen, J. Zhang, B. Zhao, D. Haden, S. Banerjee, J. Silano, H. Karwowski, and D. Umstadter. Generation of 9 MeV γ-rays by All-laser-driven Compton Scattering with Second-harmonic Laser Light. *Opt. Lett.*, 39(14):4132–4135, Jul 2014.

[13] L. Csige, D. M. Filipescu, T. Glodariu, J. Gulyás, M. M. Günther, D. Habs, H. J. Karwowski, A. Krasznahorkay, G. C. Rich, M. Sin, L. Stroe, O. Tesileanu, and P. G. .

Exploring the Multihumped Fission Barrier of ^{238}U via Sub-barrier Photofission. *Phys. Rev. C*, 87:044321, Apr 2013.

[14] J.M. Mueller, M.W. Ahmed, R.H. France, M.S. Johnson, H.J. Karwowski, L.S. Myers, J. Randrup, M.H. Sikora, M.C. Spraker, S. Stave, J.R. Tompkins, R. Vogt, H.R. Weller, C.S. Whisnant, and W.R. Zimmerman. Prompt Neutron Polarization Asymmetries in Photofission of ^{232}Th, ^{233,235,238}U, ^{237}Np, and ^{239,240}Pu. *Phys. Rev. C*, 89:034615, Mar 2014.

[15] J.R. Tompkins. *Polarized Photofission Fragment Angular Distributions of ^{232}Th and ^{238}U.* PhD thesis, University of North Carolina at Chapel Hill, 2012.

[16] F. Krishichayan, M. Bhike, A. P. Tonchev, and W. Tornow. Photon-induced Fission Product Yield Measurements on ^{235}U, ^{238}U, and ^{239}Pu. In *APS Division of Nuclear Physics Meeting Abstracts*, October 2015.

[17] A. Bohr. *U.N. Int. Conf. Peaceful Uses At. Energy*, 2:151, 1956.

[18] T.A. Mostovaya, V.I. Mostovoi, and G.V. Yakovlev. The Probability of the Ternary Fission of ^{235}U by Monochromatic Neutrons in the 0.06 - 10 eV Energy Range. *Soviet Atomic Energy*, 16(1):1–6, 1964.

[19] T.R. England and B.F. Rider. Evaluation and Compilation of Fission Product Yields. *Los Alamos National Lab Report No. LA-UR-94-3106*, 1994.

[20] N. Bohr and J.A. Wheeler. The Mechanism of Nuclear Fission. *Phys. Rev.*, 56:426–450, Sep 1939.

[21] V.M. Strutinsky and A.S. Tyapin. Soviet Phys.-JETPL8, 664 (1964), English translation: J. Exptl. *Theoret. Phys. (USSR)*, 45:960, 1963.

[22] A. Krasznahorkay. *Tunneling Through Triple-Humped Fission Barriers*, pages 281–318. Springer US, Boston, MA, 2011.

[23] C. Wagemans. *The Nuclear Fission Process.* CRC Press, Boca Raton, 1991.

[24] S.G. Nilsson. Binding States of Individual Nucleons in Strongly Deformed Nuclei. *Kgl. Danske Videnskab. Selskab., Mat.-fys Medd.*, Vol: 29, No. 16, Jan 1955.

[25] V.M. Strutinsky. Shell Effects in Nuclear Masses and Deformation Energies. *Nucl. Phys. A*, 95(2):420 – 442, 1967.

[26] P. Jachimowicz, M. Kowal, and J. Skalski. Eight-dimensional Calculations of the Third Barrier in ^{232}Th. *Phys. Rev. C*, 87:044308, Apr 2013.

[27] H.J. Krappe, J.R. Nix, and A.J. Sierk. Unified Nuclear Potential for Heavy-ion Elastic Scattering, Fusion, Fission, and Ground-state Masses and Deformations. *Phys. Rev. C*, 20:992–1013, Sep 1979.

[28] J.D. McDonnell, W. Nazarewicz, and J.A. Sheikh. Third Minima in Thorium and Uranium Isotopes in a Self-consistent Theory. *Phys. Rev. C*, 87:054327, May 2013.

[29] J. Zhao, B.N. Lu, D. Vretenar, E.G. Zhao, and S.G. Zhou. Multidimensionally Constrained Relativistic Mean-field Study of Triple-Humped Barriers in Actinides. *Phys. Rev. C*, 91:014321, Jan 2015.

[30] P.W. Zhao, Z.P. Li, J.M. Yao, and J. Meng. New Parametrization for the Nuclear Covariant Energy Density Functional with a Point-coupling Interaction. *Phys. Rev. C*, 82:054319, Nov 2010.

[31] G.A. Lalazissis, T. Nikšić, D. Vretenar, and P. Ring. New Relativistic Mean-field Interaction with Density-dependent Meson-nucleon Couplings. *Phys. Rev. C*, 71:024312, Feb 2005.

[32] W. Greiner and J.A. Maruhn. *Nuclear Models*. Springer Berlin Heidelberg, 1996.

[33] V.F. Weisskopf. *Theoretical Nuclear Physics*. John Wiley and Sons, Inc., New York, 1952.

[34] J.R. Huizenga and A.A. Katsanos. Distribution of Spacings of Nuclear Energy Levels of Mixed Spin and Parity. *Nucl. Phys. A*, 98(3):614 – 624, 1967.

[35] P.G. Thirolf and D. Habs. Spectroscopy in the Second and Third Minimum of Actinide Nuclei. *Progress in Particle and Nuclear Physics*, 49(2):325 – 402, 2002.

[36] J.J. Sakurai. *Modern quantum mechanics; rev. ed.* Addison-Wesley, Reading, MA, 1994.

[37] G. Bologna, V. Bellini, V. Emma, A. S. Figuera, S. Lo Nigro, C. Milone, and G. S. Pappalardo. Fission of Bi, Pb, Au and Pt Induced by a Coherent Photon Beam from 1000 MeV Electrons. *Il Nuovo Cimento A (1965-1970)*, 35(1):91–114, 1976.

[38] S.G. Kadmensky. Decay and Fission of Oriented Nuclei. *Phys. At. Nuc.*, 65(8):1390–1402, 2002.

[39] S.G. Kadmensky. Quantum and Thermodynamic Properties of Spontaneous and Low-energy Induced Fission of Nuclei. *Phys. At. Nuc.*, 68(12):1968–1978, 2005.

[40] S.G. Kadmensky and L.V. Titova. Problem of the Conservation of the Fissile-nucleus-spin Projection onto the Fissile-nucleus Symmetry Axis and Quantum Dynamics of the Low-energy Fission Process. *Phys. At. Nuc.*, 72(10):1738, 2009.

[41] A.S. Soldatov, G.N. Smirenkin, S.P. Kapitza, and Y.M. Tsipeniuk. Quadrupole Fission of ^{238}U. *Phys. Lett.*, 14(3):217 – 219, 1965.

[42] S. Nair, D.B. Gayther, B.H. Patrick, and E.M. Bowey. Fission-neutron and Fragment Angular Distributions from Threshold Photofission of ^{232}Th and ^{238}U. *Journal of Physics G: Nuclear Physics*, 3(7):965, 1977.

[43] E.J. Dowdy and T.L. Krysinski. Angular Distributions of ^{238}U Photofission Fragments. *Nucl. Phys. A*, 175(3):501 – 512, 1971.

[44] N. Carjan, P. Talou, and O. Serot. Emission of Scission Neutrons in the Sudden Approximation. *Nucl. Phys. A*, 792(1):102 – 121, 2007.

[45] M. Rizea, N. Carjan, and T. Wada. Angular Distribution of the Scission Neutrons with Respect to the Fission Axis. *Physics Procedia*, 47:27 – 32, 2013.

[46] V.P. Éismont. Neutrons from the Fission of Excited Nuclei. *Soviet Atomic Energy*, 19(2):1000–1003, 1965.

[47] J.M. Verbeke, J. Randrup, and R. Vogt. Fission Reaction Event Yield Algorithm FREYA User Manual. Technical Report LLNL-TM-654899, Lawrence Livermore National Laboratory, 2010.

[48] C. Manailescu, A. Tudora, F.-J. Hambsch, C. Morariu, and S. Oberstedt. Possible Reference Method of Total Excitation Energy Partition Between Complementary Fission Fragments. *Nucl. Phys. A*, 867(1):12 – 40, 2011.

[49] M. Csatlos, A. Krasznahorkay, P.G. Thirolf, D. Habs, Y. Eisermann, T. Faestermann, G. Graw, J. Gulyas, M.N. Harakeh, R. Hertenberger, M. Hunyadi, H.J. Maier, Z. Mate, O. Schaile, and H.-F. Wirth. Resonant Tunneling Through the Triple-humped Fission Barrier of ^{236}U. *Phys. Lett. B*, 615(3-4):175 – 185, 2005.

[50] A. Krasznahorkay, D. Habs, M. Hunyadi, D. Gassmann, M. Csatls, Y. Eisermann, T. Faestermann, G. Graw, J. Gulyas, R. Hertenberger, H.J. Maier, Z. Mate, A. Metz, J. Ott, P. Thirolf, and S.Y. van der Werf. On the Excitation Energy of the Ground State in the Third Minimum of ^{234}U. *Phys. Lett. B*, 461(1-2):15 – 21, 1999.

[51] L. Csige, M. Csatlos, T. Faestermann, Z. Mate, J. Gulyas, D. Habs, R. Hertenberger, A. Krasznahorkay, R. Lutter, H.J. Maier, P.G. Thirolf, and H.-F. Wirth. Hyperdeformed Sub-barrier Fission Resonances Observed in ^{232}U. *Phys. Rev. C*, 80:011301, Jul 2009.

[52] G.N. Smirenkin and A.S. Soldatov. Cross Section for ^{232}Th in the Threshold Region. *Phys. At. Nuc.*, 59(2):203 – 212, 1996.

[53] N.S. Rabotnov, G.N. Smirenkin, A.S. Soldatov, L.N. Usachev, S.P. Kapitza, and Y.M. Tsipenyuk. Photofission of Th^{232}, U^{238}, Pu^{238}, Pu^{240}, Pu^{242} and the Structure of the Fission Barrier. *Yad.Fiz.*, 11:508, 1970.

[54] O.Y. Mafra, S. Kuniyoshi, and J. Goldemberg. Intermediate Structure in the Photoneutron and Photofission Cross Sections in ^{238}U and ^{232}Th. *Nucl. Phys. A*, 186(1):110 – 126, 1972.

[55] M.V. Yester, R.A. Anderm, and R.C. Morrison. Photofission Cross Sections of ^{232}Th and ^{236}U from Threshold to 8 MeV. *Nucl. Phys. A*, 206(3):593 – 613, 1973.

[56] P.A. Dickey and P. Axel. ^{238}U and ^{232}Th Photofission and Photoneutron Emission Near Threshold. *Phys. Rev. Lett.*, 35:501–504, Aug 1975.

[57] C.D. Bowman, I.G. Schröder, K.C. Duvall, and C.E. Dick. Subthreshold Photofission of ^{235}U and ^{232}Th. *Phys. Rev. C*, 17:1086–1088, Mar 1978.

[58] J.T. Caldwell, E.J. Dowdy, B.L. Berman, R.A. Alvarez, and P. Meyer. Giant Resonance for the Actinide Nuclei: Photoneutron and Photofission Cross Sections for ^{235}U, ^{236}U, ^{238}U, and ^{232}Th. *Phys. Rev. C*, 21:1215–1231, Apr 1980.

[59] J.W. Knowles, W.F. Mills, R.N. King, B.O. Pich, S. Yen, R. Sobie, L. Watt, T.E. Drake, L.S. Cardman, and R.L. Gulbranson. A High-resolution Measurement of the Photofission Spectrum of ^{232}Th Near Threshold. *Phys. Lett. B*, 116(5):315 – 319, 1982.

[60] H.X. Zhang, T.R. Yeh, and H. Lancman. Photofission Cross Section of ^{232}Th. *Phys. Rev. C*, 34:1397–1405, Oct 1986.

[61] D.J.S. Findlay, N.P. Hawkes, and M.R. Sene. Photofission of ^{232}Th Near Threshold. *Nucl. Phys. A*, 458(2):217 – 224, 1986.

[62] A.I. Blokhin and A.S. Soldatov. Analysis of the Cross Section for ^{232}Th Photofission in the Subbarrier Energy Region. *Phys. At. Nuc.*, 72(6):917–927, 2009.

[63] A. Manfredini, M. Muchnik, L. Fiore, C. Ramorino, H.G. de Carvalho, J. Lang, and R. Muller. ^{238}U Fission Induced by Low-energy Monochromatic γ-rays. *Nuclear Physics*, 74(2):377 – 384, 1965.

[64] A.M. Khan and J.W. Knowles. Photofission of ^{232}Th, ^{282}U and ^{235}U Near Threshold Using a Variable Energy Beam of γ-rays. *Nucl. Phys. A*, 179(2):333 – 352, 1972.

[65] R.A. Anderl, M.V. Yester, and R.C. Morrison. Photofission Cross Sections of ^{238}U and ^{235}U from 5.0 MeV to 8.0 MeV. *Nucl. Phys. A*, 212(2):221 – 240, 1973.

[66] M. Herman, R. Capote, B.V. Carlson, P. Obloinsk, M. Sin, A. Trkov, H. Wienke, and V. Zerkin. EMPIRE: Nuclear Reaction Model Code System for Data Evaluation. *Nuclear Data Sheets*, 108(12):2655 – 2715, 2007.

[67] D.L. Hill and J.A. Wheeler. Nuclear Constitution and the Interpretation of Fission Phenomena. *Phys. Rev.*, 89:1102–1145, Mar 1953.

[68] W. Hauser and H. Feshbach. The Inelastic Scattering of Neutrons. *Phys. Rev.*, 87:366–373, Jul 1952.

[69] J.M. Mueller, M.W. Ahmed, B. Davis, J.M. Hall, S.S. Henshaw, M.S. Johnson, H.J. Karwowski, D. Markoff, L.S. Myers, B.A. Perdue, S. Stave, J.R. Tompkins, M.J. Tuffley, and H.R. Weller. Measurement of Prompt Neutron Polarization Asymmetries in Photofission of ^{235,238}U, ^{239}Pu, and ^{232}Th. *Phys. Rev. C*, 85:014605, Jan 2012.

[70] J.M. Mueller. *Prompt Neutron Polarization Asymmetries in Photofission of Isotopes of Thorium, Uranium,Neptunium, and Plutonium.* PhD thesis, Duke University, 2013.

[71] J.T. Caldwell, E.J. Dowdy, R.A. Alvarez, B.L. Berman, and P. Meyer. Experimental Determination of Photofission Neutron Multiplicities for ^{235}U, ^{236}U, ^{238}U, and ^{232}Th Using Monoenergetic Photons. *Nuclear Science and Engineering*, 73:153–163, Feb 1980.

[72] H.R. Weller, M.W. Ahmed, H. Gao, W. Tornow, Y.K. Wu, M. Gai, and R. Miskimen. Research Opportunities at the Upgraded HIγS Facility. *Progress in Particle and Nuclear Physics*, 62(1):257 – 303, 2009.

[73] C. Sun. *Characterizations and Diagnostics of Compton Light Source*. PhD thesis, Duke University, 2009.

[74] J.K. Sprinkle, Jr., H.O. Menlove, M.C. Miller, and P.A. Russo. An Evaluation of the INVS Model IV Neutron Counter. *Los Alamos National Lab Report No. LA-12496-MS*, 1993.

[75] Cremat Inc. *CR-110 Charge Sensitive Preamplifier: Application Guide*, May 2014. Rev. 2.

[76] M.W. Ahmed, C.R. Howell, and A.S. Crowell. CODA at TUNL (C@ T) and the TUNL Real-Time Analysis Package (TRAP) Version 03. a (2014).

[77] M.B. Chadwick et al. ENDF/B-VII.0: Next Generation Evaluated Nuclear Data Library for Nuclear Science and Technology. *Nuclear Data Sheets*, 107(12):2931–3118, December 2006.

[78] Handbook on Photonuclear Data for Applications, Cross-sections and Spectra. Technical report, International Atomic Energy Agency, Vienna, 2000. IAEA-TECDOC-1178.

[79] T.J. Langford, C.D. Bass, E.J. Beise, H. Breuer, D.K. Erwin, C.R. Heimbach, and J.S. Nico. Event Identification in ^{3}He Proportional Counters Using Risetime Discrimination. *Nucl. Instrum. Methods A*, 717:51 – 57, 2013.

[80] S. Shalev, Z. Fishelson, and J.M. Cuttler. The Wall Effect in ^{3}He Counters. *Nucl. Instrum. Meth.*, 71(3):292 – 296, 1969.

[81] S. Agostinelli et al. Geant4: A Simulation Toolkit. *Nucl. Instrum. Meth. A*, 506(3):250 – 303, 2003.

[82] V. Uzhinsky. Development of the Fritiof Model in Geant4. In *Joint International Conference on Supercomputing in Nuclear Applications and Monte Carlo 2010 (SNA + MC2010)*, 2010.

[83] D.H. Wright and M.H. Kelsey. The Geant4 Bertini Cascade. *Nucl. Instrum. Meth. A*, 804:175 – 188, 2015.

[84] J. Apostolakis, G. Folger, V. Grichine, A. Heikkinen, A. Howard, V. Ivanchenko, P. Kaitaniemi, T. Koi, M. Kosov, J.M. Quesada, A. Ribon, V. Uzhinskiy, and D. Wright. Progress in Hadronic Physics Modeling in Geant4. *Journal of Physics: Conference Series*, 160(1):012073, 2009.

[85] C.W. Arnold, T.B. Clegg, H.J. Karwowski, G.C. Rich, J.R. Tompkins, and C.R. Howell. Characterization of an INVS Model IV Neutron Counter for High Precision (γ,n) Cross-section Measurements. *Nucl. Instrum. Meth. A*, 647(1):55 – 62, 2011.

[86] J.H. Hubbell and S.M. Seltzer. *Tables of X-ray Mass Attenuation Coefficients and Mass Energy-absorption Coefficients From 1 keV to 20 MeV for Elements Z = 1 to 92*. NIST Standard Reference Database.

[87] J.F. Ziegler, M.D. Ziegler, and J.P. Biersack. SRIM: The Stopping and Range of Ions in Matter (2010) . *Nucl. Instrum. Meth. B*, 268(11-12):1818 – 1823, 2010. 19th International Conference on Ion Beam Analysis.

[88] J.W. Marsh, D.J. Thomas, and M. Burke. High Resolution Measurements of Neutron Energy Spectra from AmBe and AmB Neutron Sources. *Nucl. Instrum. Meth. A*, 366(2):340 – 348, 1995.

[89] E.C. Schreiber, R.S. Canon, B.T. Crowley, C.R. Howell, J.H. Kelley, V.N. Litvinenko, S.O. Nelson, S.H. Park, I.V. Pinayev, R.M. Prior, K. Sabourov, M. Spraker, W. Tornow, Y. Wu, E. A. Wulf, and H.R. Weller. First Measurement of the Near-threshold ^{2}H($\vec{\gamma}, n$)p Analyzing Power Using a Free-electron Laser Based γ-ray Source. *Phys. Rev. C*, 61:061604, May 2000.

[90] W. Tornow, N.G Czakon, C.R Howell, A. Hutcheson, J.H. Kelley, V.N. Litvinenko, S.F. Mikhailov, I.V. Pinayev, G.J. Weisel, and H Witala. Low-energy Photodisintegration of the Deuteron and Big-Bang Nucleosynthesis. *Phys. Lett. B*, 574:8 – 13, 2003.

[91] R.E. Pywell, O. Mavrichi, W.A. Wurtz, and R. Wilson. Photon Flux Monitor for a Mono-energetic Gamma-ray Source. *Nucl. Instrum. Meth. A*, 606(3):517 – 522, 2009.

[92] D.G. Madland and J.R. Nix. New Calculation of Prompt Fission Neutron Spectra and Average Prompt Neutron Multiplicities. *Nuclear Science and Engineering*, 81(2):213–271, 1982.

[93] J. Randrup and R. Vogt. Calculation of Fission Observables Through Event-by-event Simulation. *Phys. Rev. C*, 80:024601, Aug 2009.

[94] R. Vogt, J. Randrup, D. A. Brown, M. A. Descalle, and W. E. Ormand. Event-by-event Evaluation of the Prompt Fission Neutron Spectrum from ^{239}Pu(n, f). *Phys. Rev. C*, 85:024608, Feb 2012.

[95] W. Reisdorf, J.P. Unik, H.C. Griffin, and L.E. Glendenin. Fission Fragment K X-ray Emission and Nuclear Charge Distribution for Thermal Neutron Fission of ^{233}U, ^{235}U, ^{239}Pu and Spontaneous Fission of ^{252}Cf. *Nucl. Phys. A*, 177(2):337 – 378, 1971.

[96] W. Holubarsch, E. Pfeiffer, and F. Gonnenwein. Fragment Kinetic Energies in MeV Neutron-induced Fission of ^{232}Th. *Nucl. Phys. A*, 171(3):631 – 640, 1971.

[97] F. Vivs, F.-J. Hambsch, H. Bax, and S. Oberstedt. Investigation of the Fission Fragment Properties of the Reaction ^{238}U(n,f) at Incident Neutron Energies up to 5.8 MeV. *Nucl. Phys. A*, 662(1):63 – 92, 2000.

[98] T. Kawano, S. Chiba, and H. Koura. Phenomenological Nuclear Level Densities using the KTUY05 Nuclear Mass Formula for Applications Off-Stability. *Journal of Nuclear Science and Technology*, 43(1):1–8, 2006.

[99] S. Lemaire, P. Talou, T. Kawano, M. B. Chadwick, and D. G. Madland. Monte Carlo Approach to Sequential Neutron Emission from Fission Fragments. *Phys. Rev. C*, 72:024601, Aug 2005.

[100] H. Koura, M. Uno, T. Tachibana, and M. Yamada. Nuclear Mass Formula with Shell Energies Calculated by a New Method. *Nucl. Phys. A*, 674(1):47 – 76, 2000.

[101] A.I. Lengyel, O.O. Parlag, V.T. Maslyuk, M.I. Romanyuk, and O.O. Gritzay. Calculations of Average Numbers of Prompt Neutrons for Actinide Photofission. *Journal of Nuclear and Particle Physics*, 6(2):43–46, 2016.

[102] W.D. Loveland, D.J. Morrissey, and G.T. Seaborg. *Fission.* John Wiley & Sons, Inc., 2005.

[103] D.E. Cullen. Sampling ENDL Watt Fission Spectra. *Lawrence Livermore National Laboratory Report No. UCRL-TR-203251*, 1991.

[104] E. Aguayo, A.S. Ankney, T.J., Berguson, R.T. Kouzes, J.L. Orrell, and M.D. Troy. Cosmic Ray Interactions in Shielding Materials. *Pacific Northwest National Laboratory Report No. PNNL-20693*, 2011.

[105] L.W. Fagg and S.S. Hanna. Polarization Measurements on Nuclear Gamma Rays. *Rev. Mod. Phys.*, 31:711–758, Jul 1959.

[106] N. Ensslin, M.S. Krick, D.G. Langner, M.M. Pickrell, T.D. Reilly, and J.E. Stewart. Passive Neutron Multiplicity Counting. In *Passive Nondestructive Assay Manual PANDA*, chapter 6, pages 201–213. Los Alamos Laboratory Report No. LA-UR-07-1402, 1993.

[107] N. Pacilio. *Reactor-noise Analysis in the Time Domain. AEC Critical Review Series.* Jan 1969.

[108] Y. Wu. Next Generation Laser-Compton Gamma-ray Beam Facilities. In *APS Meeting Abstracts*, September 2014.

[109] J.M. Mueller, M.W. Ahmed, A. Kafkarkou, D.P. Kendellen, M.H. Sikora, M.C. Spraker, H.R. Weller, and W.R. Zimmerman. Tests of a Novel Method to Assay SNM Using Polarized Photofission and its Sensitivity in the Presence of Shielding. *Nucl. Instrum. Meth. A*, 776:107 – 113, 2015.

[110] Radiological Health Handbook. Technical report, U.S. Department of Health, Education and Welfare.

[111] D.G. Tayal. *Nuclear Physics*. Himalaya Publishing House.